Bimodal Upconverting Nanoparticles for MRI and Optical Imaging

Qian Ying Li

A Thesis

in

The Department

of

Chemistry and Biochemistry

Presented in Partial Fulfillment of the Requirements

for the Degree of Master of Science (Chemistry) at

Concordia University

Montreal, Quebec, Canada

December, 2015

CONCORDIA UNIVERSITY
School of Graduate Studies

This is to certify that the thesis prepared

By: **Qian Ying Li**

Entitled: **Bimodal Upconverting Nanoparticles for MRI and Optical Imaging**

and submitted in partial fulfillment of the requirements for the degree of

Master of Science (Chemistry)

complies with the regulations of this University and meets the accepted standards with respect to originality and quality.

Signed by the final examining committee:

_____ Chair

Dr. Yves Gelinas

_____ Examiner

Dr. Louis Cuccia

_____ Examiner

Dr. Xavier Ottenwaelder

_____ Thesis Supervisor

Dr. John Capobianco

Approved by_____

Chair of Department or Graduate Program Director

_____

Dean of Faculty

Date December 14, 2015

ABSTRACT

Bimodal Upconverting Nanoparticles for MRI and Optical Imaging

Qian Ying Li, M.Sc.

Integrating multiple functionalities into individual nanoscale materials is of tremendous importance in biomedicine, since this would expand the capabilities of nanoscale materials to perform multiple tasks. Here, fluorescence optical imaging and magnetic resonance imaging (MRI) are combined within the same nanoparticle based material. $NaYF_4$: $Tm^{3+,}$ Yb^{3+}, showed NIR to NIR upconversion, giving deep tissue penetration, which is an advantage in medical imaging. Their lanthanide ions (Tm^{3+}/Yb^{3+}) derived optical properties in the near infrared region of the spectrum, where tissue is maximally transparent. Multimodal properties may be imparted to $NaYF_4$: $Tm^{3+,}$ Yb^{3+} *via* the functionalization of gadonium-tetraazacyclododecanetetraacetic acid (Gd-DOTA), a commercially available MRI contrast agent. Gd-DOTA was covalently bonded to the surface of the silica coated UCNPs using the click reaction. This imaging probe may be used for both MRI and fluorescent imaging.

Another approach to achieve bimodalities is by doping Gd^{3+} ions into the systems of UCNPs, which provides both magnetic and optical properties. Ultra-small $NaGdF_4$, Tm^{3+}, Yb^{3+} of 5 nm was chosen since it is an excellent T_1 contrast agent. The surface chemistry of nanoparticles has direct impact on its physiochemical properties. Therefore, it is aimed to design nanoparticle based blood pool contrast agent for disease diagnostics, which involved the functionalization the polyethylene glycol (PEG) polymer on the ultra-small UCNPs. Here we report the design and characterization of bimodal contrast agent, PEG coated ultra-small $NaGdF_4$, Tm^{3+}, Yb^{3+}.

ACKNOWLEDGEMENTS

I would like to express my special appreciation and thanks for my supervisor Prof. John A. Capobianco. You had given me the chance to work on this master's research project, which was a life changing experience for me. I could see myself growing from a laboratory technician toward research scientist. Only with your continuous guidance and encouragement, I was able to progress on this research project.

I would like to thank my thesis committee members, Prof. Louis A. Cuccia and Prof. Xavier Ottenwaelder for their aspiring guidance to this project and support throughout the years.

I express my warm thanks to Dr. Marc André Fortin, collaborator to this project, for sharing expertise and providing some necessary facilities for the research.

I am using this opportunity to express my gratitude to all my lab colleagues from the Lanthanide Research Group: Jessica Yu, Diana Consuelo Rodriguez Burban, Paola Andrea Rojas Gutierrez, especially Dr. Emma Martin Rodriguez, Dr. Nicoleta Bogdan and Dr. Rafik Naccache, for their patient guidance, invaluably constructive criticism and friendly advice during the project I worked.

Finally, I sincerely thank my parents for supporting me throughout all my studies at University, for providing a home in which to complete my thesis writing.

Table of Contents

List of Figures

List of Tables

List of Abbreviations

CA	Contrast Agent
DOTA	1,4,7,10-tetrakis(carboxymethyl)-1,4,7,10- tetraazacyclododecane
EPR	Enhance Permeability and Retention
ESA	Excited State Absorption
ETU	Energy Transfer Upconversion
FRET	Fluorescence Resonance Energy Transfer
FT-IR	Fourier Transform Infrared
Gd	Gadolinium
Ln	Lanthanide
Ln^{3+}	Trivalent Lanthanide Ions
LnNPs	Lanthanide-Doped Nanoparticles
MS	Mass Spectrometry
NIR	Near Infrared
NMR	Nuclear magnetic resonance
NPs	Nanoparticles
PEG	Polyethylene Glycol
QDs	Quantum Dots
RF	Radiofrequency
SAED	Selected Area Electron Diffraction
TEOS	Tetraethyl Orthosilicate
TEM	Transmission Electron Microscopy
UC	Upconversion
UCNP	Upconverting Nanoparticles
UV	Ultraviolet
XRD	X-Ray Diffraction
XPS	X-ray photoelectron spectroscopy

Chapter One – Introduction

1.1 Nanotechnology and Nanomedecine

Nanotechnology has become a rapidly growing area of science over the last decade. It has drawn much attention in research and development due to its promising benefits in the fields of medicine, electronics, material engineering etc. In the domains of health and medicine, nanotechnology has developed quickly and is used extensively in clinical research. Therefore, it is important to understand the unique properties of nanomaterials, the benefits and risks of using nanomaterials for medicinal purposes.

Nanoscience may be broadly defined as the study of materials and devices usually less than 100 nm. However, this threshold is arbitrary and much discussion has occurred over the years as to whether a more lax definition at 1000 nm should be used since many nanoscience topics would be left in limbo. Ozin in his seminal book on Nanochemistry states “nanochemistry should not be defined only in terms of a length scale”. He proposes to use concepts such size, shape, self-assembly and defects. All of these concepts are important in understanding. For example as the particle size decreases to the nano-regime, the surface to volume ratio increases imparting very interesting properties to the material since the majority of atoms now lie on the surface. Atoms at the surface in general possess dangling bonds which increases the surface energy. Since nature likes to reduce the free energy it will reduce the surface energy by causing the dangling bonds to react. With such consequence, the surface at the nanoscale show high reactivity in comparison to the bulk. Other properties of materials which are size dependent are optical, magnetic and electronics [1].

A common example of change in the optical property due to size is the quantum dots whereas an excellent example of size shape relationship is found for gold. In the case of quantum dots, their unique optical properties arise from their physical dimensions, which are smaller than the "exciton Bohr radius" that ranges roughly between 2 and 20 nm. An excited electron in solids "roams" around the "parent" atom at a distance equal to the "exciton Bohr radius". If the physical size of the nanoparticle becomes comparable or smaller than the "exciton Bohr radius" the electrons start to behave differently affecting the electron structure thus the optical properties. The color of gold at the nanoscale is determined by the oscillating frequency of the conduction electrons. These oscillations are known as "plasmons" [2]. Spherical gold nanoparticles are isotropic therefore the conduction electrons have a single frequency of oscillation. However if the gold nanoparticle is rod shape (anisotropic) two different frequencies of oscillation, transverse and longitudinal thus the colour of the gold nanorods will be different.

Nanomaterials are expected to have a major impact on nanomedicine since the nanometer scale is interesting in biological systems (for example proteins are tens of nanometer in size) since it would allow to probe biological systems. Nanomaterials have been proposed for a number of uses including imaging, diagnostics and therapeutics. The major interest in nanoparticles stems from optical and magnetic properties, which may be used in imaging both *in vitro* and *in vivo.*

At the tissue level, the enhanced permeability and retention (EPR) effect is the size dependent property which is very important in tumor targeting [3]. A key benefit offered by nanomaterials is the possibility to achieve "active" targeting making use of the reactive surface which would facilitate functionalization of the nanoparticles [4]. However, much more work is

needed to characterize the full impact of size, shape, surface chemistry, the EPR effect, cell targeting etc. of nanomaterials in biological systems.

1.2 Lanthanide-Doped Nanoparticles (LnNPs) in Potential Biological Applications

Nanocrystals of rare-earth compounds, such as oxides [5], phosphates [6], fluorides [7] have recently become a new focus of research due to their unique optical property, and have become promising candidates for fluorescence labeling [8]. The unique feature of these nanoparticles is their ability of emitting photons in visible range following near infrared excitation, in a process called upconversion. β-$NaYF_4$ is considered to be among the most efficient host material for upconversion phosphors, when co-doped with Yb^{3+} and Er^{3+} or Tm^{3+} ions. More interestingly, doping with highly paramagnetic Gd^{3+} ions has demonstrated the potential use as a T_1 contrast agent in magnetic resonance imaging [9].

1.2.1 In vitro Optical Imaging

There are substantial advantages that lanthanide-doped nanoparticles offer in the biomedical applications. For example, in the application of *in vitro* cell and tissue imaging, Zijlmans *et al*. [10] in 1999 used Y_2O_2S:Tm/Yb to study the distribution of prostate specific antigent (PSA) in paraffin-embedded sections of human prostate tissue. They provided two important evidences of using lanthanide doped nanocrystals as fluorescent probes over conventional ones. The problem of non-specific autofluorescence associated with UV excitation was absent under near infrared (NIR) excitation which resulting in a low optical background autofluorescence since biomolecules show minimal absorbance in the NIR region 700-1000 nm (optical window). Moreover, it was reported that lanthanide doped upconverting nanoparticles

(Ln-UCNPs) did not show photobleaching due to unaffected chemical bonds in the photo cycle and demonstrated excellent sensitivity. Thus, it demonstrated for the first time the potential application of Ln-UCNPs as luminescent probe for bioimaging.

1.2.2 *In vivo* Optical Imaging

Organic fluorophores and fluorescent proteins have been traditionally used for *in vivo* optical imaging which require UV excitation. Not only they suffer from low photostability and strong background autofluorescence, the resulting broad bands often cause spectral overlap which could be a problem in spectral interpretation during multicolor imaging. Quantum dots (QD) are one of most extensively-studied luminescence nanoparticles. The use of QDs *in vivo* studies raises few problems related to the its toxicity due to the use of heavy metals and potential tissue damage caused by the use of ultraviolet excitation (UV) [11].

In contrast to organic fluorophores, Ln-UCNPs are characterized with high photostability, no photobleaching, and narrow photoluminescence spectra which make them suitable for multiplexed imaging [12]. In contrast to QD, Ln-UCNPs have low cytotoxicity, no photoblinking and the color of the emitted light does not dependent on the size of luminescent nanoparticles, but only on the nature of the lanthanide ions, and thus avoiding the need to separate particles of different sizes formed during the synthesis [13, 14].

Moreover, the challenge faced for *in vivo* optical imaging is tissue penetration depth due to light scattering. Light scattering is dependent on the inverse of the excitation wavelength (Rayleigh scattering), therefore, Ln-UCNPs which use low energy near infrared (NIR) as excitation source, offer a greater tissues penetration depth in comparison to its UV counterparts.

In vivo imaging of LnNPs was reported by Zhang and co-workers [15] using 50-nm $NaYF_4$: Er, Yb nanoparticle in rats. Following 980 nm excitation, the characteristic visible green emission of Er^{3+} was detected up to 10 mm beneath the skin. The suitability of Ln-UCNPs for *in vivo* optical imaging was also demonstrated by Nyk *et al.* [16] using $NaYF_4$: Tm, Yb. The remarkable advantage of using thulium is NIR-to-NIR upconversion, offering greater tissue penetration since both the excitation and emission wavelength fall within the optimal optical window. The whole body image showed high contrast and high signal-to-ratio, which demonstrated the excellent potential of Ln-UCNPs for *in vivo* imaging.

1.3 Magnetic Resonance Imaging (MRI)

The interesting optical properties of Ln-UCNPs have been demonstrated in biological systems. Doping these nanoparticles with Gd^{3+} ions would provide an additional imaging modality since the Ln-UCNPs would be used in magnetic resonance imaging.

Among all of the currently used diagnostic tools, MRI is one of the most powerful imaging techniques, which provides a high resolution image non-invasively. MRI provides functional and anatomical details of human body, allowing clinical professionals to distinguish normal and diseased tissues. Gadolinium (Gd^{3+}) is an extensively studied paramagnetic agent which shortens the T_1 relaxation times of protons, resulting in better contrast resolution, and improving the visibility of internal structures for clinical practices. Several Gd^{3+} based chelates are commercially available such as Dotarem, Omniscan and Gadovist. These Gd^{3+} chelates have rather low relaxivity, and must be administered in quite high dose to provide a good contrast [17]

In recent years, increasing research activities have been focused on nanoscaled contrast agents materials for MRI, for example, the doping of Gd^{3+} ions oxides or fluorides nanoparticles [18, 19]. The main advantage of using nanoparticles based systems compared to chelate complexes is that the former is expected to yield higher relaxivities due to a higher concentration of magnetic ions, thus increasing the sensitivity of the technique. In addition, the benefit of having Gd^{3+} ions into the crystal system would reduce substantially the leakage of Gd^{3+} ions to the body which is a concern when using the Gd^{3+} complexes. Another advantage of the Gd^{3+} doped nanoparticles contrast agent for MRI is that it would have longer circulation time due to enhanced vascular permeability thus an excellent agent for medical imaging [20, 21]. Nanoparticles also offer the added advantage that is the surface can be functionalized imparting active targeting properties.

1.4 Objectives

Among all the imaging techniques, optical imaging is well-known for its high sensitivity, and capable of providing cellular- or molecular-level information. However, it still lacks the capability to obtain full anatomical and physiological structures. On the other hand, MRI provides excellent spatial resolution and penetration depth for *in vivo* imaging, and provides exceptional anatomical information, but suffers from limited sensitivity and lacks resolution for imaging at the cellular level. The combination of MRI and optical imaging leads to the development of new approaches to bridge the gap of high sensitivity and high spatial resolution and offset the drawbacks of these two modalities. For example, a combination of *in vivo* imaging could be used to image a tumor pre-operatively utilizing MRI and intraoperatively using optical imaging which could facilitate the image guided real time surgery.

Therefore, the objective of this thesis is to design a hybrid magnetic and optical imaging probe. Due to the potential benefits of nanoscaled materials for *in vivo* imaging, lanthanide doped nanoparticles are selected as the base material for engineering a biocompatible bimodal contrast agent. There could be two approaches for designing such nanoconstruct. First, the paramagnetic property could be added to the upconverting nanoparticles by surface functionalization; Secondly, gadolinium could be incorporated into the host material such as $NaGdF_4$: Tm^{3+}, Yb^{3+}, which has both optical and magnetic properties. Moreover, Tm^{3+} ion has a characteristic strong emission centered at 800 nm following 980 nm excitation. NIR emission has significant advantage over visible emissions for *in vivo* imaging.

The ideal nanoparticle contrast agent for biological applications should fullfill a number of stringent requirements: it should be water dispersible; stable in biological conditions (i.e resist aggregation); it should exhibit minimum nonspecific binding and be resistant to reticuloendothelial system (RES) or macrophage system uptake, it should provide a good contrast quality (high signal-to-noise ratio) and sufficiently long circulation times in the blood if administrated intravenously [22].

Chapter Two – Theory

2.1 The Lanthanides

The lanthanides comprise the largest naturally-occurring group in the periodic table. The lanthanides are the group of elements occupying the sixth row of the periodic table starting from element 51 (lanthanum) to 71 (lutetium). While scandium and yttrium are not part of the lanthanide series, they are usually considered lanthanide-like or "lanthanoides" due to the similarity in their chemical properties and their occurrence in the same ores as the other elements of the lanthanides.

While some of the lanthanides may exist in the +2 and +4 oxidation states, the +3 oxidation state is the most prevalent and is generally known to be the most stable configuration for the lanthanide ions. This stems from the fact that the +3 oxidation state leaves the ions in the [Xe] $4f^{x}$ configuration and the ionization energy of the f electrons is so large, that they are considered core-like. This measure of stability also implies that modification *via* chemical means is highly difficult.

The ionic radii of the lanthanides decrease from 103 pm (La^{3+}) to 86 pm (Lu^{3+}) shown in figure 2.1. The poor nuclear charge shielding behavior of the f electrons occurs due to the fact that the 6s and 5d electrons are drawn closer towards the nucleus resulting in the well-known lanthanide contraction effect. The f-electrons are the poorest with respect to shielding, while the s-electrons are the best. The $5s^2$ and $5p^6$ electrons penetrate the f-subshell and as the nuclear charge increases, an increase in the contraction is also observed. The shielding of the f-electrons by their s and p counterparts has a direct impact on the magnetic and spectroscopic properties especially in the fact that they are highly uninfluenced by the ligands coordinating the lanthanide

atoms. In addition, the crystal field splitting is significantly less in comparison to that of the d-block elements. As a result, the bands in the electronic spectra of the lanthanides are very sharp showing narrow emission profiles. Additionally, f-f transitions are Laporte forbidden, resulting in low transition probabilities and long excited states lifetime (on the order of ms). The lanthanide elements have ladder-like energy levels of 4f states which allow for sequentially absorption of multiple photons with suitable energy to reach a higher excited state, giving rise to an important property of lanthanides ions: upconversion. [23, 24, 25, 26]

21 **Sc^{3+}** [Ar] 75													
39 **Y^{3+}** [Kr] 102													
57 **La^{3+}** $[Xe]4f^{0}$ 103	58 **Ce^{3+}** $[Xe]4f^{1}$ 102	59 **Pr^{3+}** $[Xe]4f^{2}$ 99	60 **Nd^{3+}** $[Xe]4f^{3}$ 98.3	61 **Pm^{3+}** $[Xe]4f^{4}$ 97	62 **Sm^{3+}** $[Xe]4f^{5}$ 95.8	63 **Eu^{3+}** $[Xe]4f^{6}$ 94.7	64 **Gd^{3+}** $[Xe]4f^{7}$ 93.8	65 **Tb^{3+}** $[Xe]4f^{8}$ 92.1	66 **Dy^{3+}** $[Xe]4f^{9}$ 91.2	67 **Ho^{3+}** $[Xe]4f^{10}$ 90.1	68 **Er^{3+}** $[Xe]4f^{11}$ 89	70 **Yb^{3+}** $[Xe]4f^{12}$ 88	71 **Lu^{3+}** $[Xe]4f^{12}$ 86.1

Atomic number
Symbol
Electronic configuration (M^{3+})
Ionic radius of M^{3+} (pm)

Figure 2.1: The rare earth metals consist of Group III and lanthanides elements [27].

2.2 Upconversion Mechanisms

Upconversion (UC) refers to the generation of light with wavelength shorter than the excitation source. There are three major mechanisms by which upconversion may occur namely excited state absorption (ESA), energy transfer upconversion (ETU) and photon avalanche (PA) upconversion. However, for the purpose of this thesis we will only discuss excited state absorption and energy transfer upconversion.

Excited state absorption involves the sequential absorption of two or more long wavelength photons promoting an ion from the ground to an excited state and followed by the emission of one higher energy photon (shorter wavelength). Figure 2.2 (a) showed the ESA mechanism. The ion in the ground state absorbs a pump photon ① and is excited to an intermediate excited state E1. A second pump photon ② promotes the ion to a higher excited state E2 followed by emission and relaxation of the ion to the ground state.

Energy transfer upconversion occurs *via* the transfer of energy between a neighbouring pair of ions where one ion acts as a donor of energy, while the second acts as an acceptor of energy. A simplified mechanism of energy transfer upconversion is summarized in 2.2 (b). In this upconversion process, an incoming pump photon, corresponding to the energy gap separating states G and E_1, promotes both donor ions (usually an ion with a high absorption cross-section) to the intermediate excited state E_1 (step ①). In the second step (②), a non-radiative energy transfer from the donor ion to the acceptor ion results in the promotion of the latter to its excited state E_1 after which a second energy transfer promotes the acceptor ion to excited state E_2 (③). Following the energy transfer, the donor ions relax to their ground state while the acceptor ion, now in E_2, undergoes a radiative decay with emission and returns to its ground state. The ETU mechanism is dependent on the overall dopant ion concentration due to

the increased proximity of neighboring ion pairs that facilitate the energy transfer process. Furthermore, the mechanism efficiency is also influenced by the choice of donor and acceptor ions, as well as their respective concentrations [26].

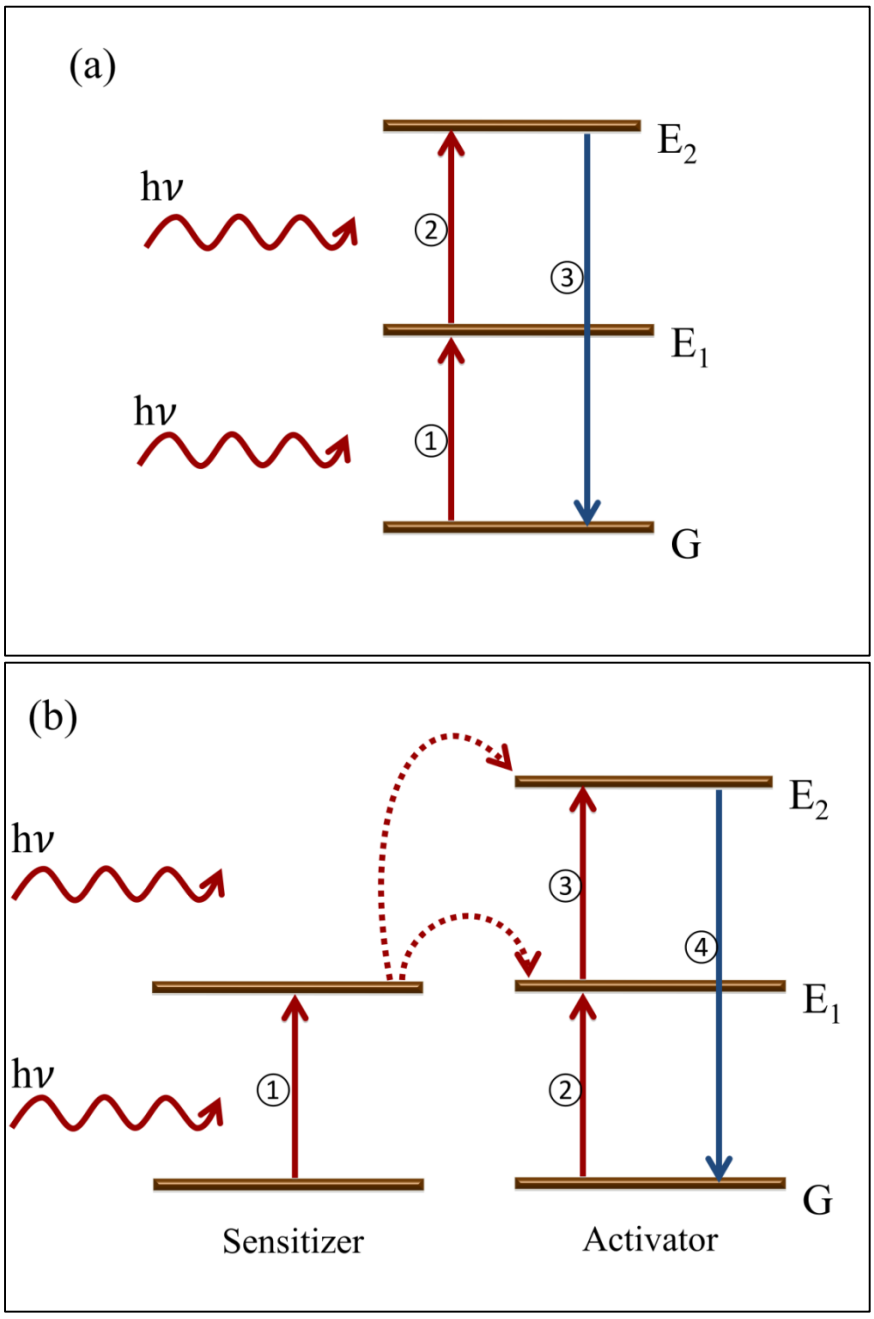

Figure 2.2: Upconversion mechanisms (a) excited-state absorption (ESA); (b) energy transfer upconversion (ETU).

2.3 Upconversion Materials: Lanthanide-Doped Nanoparticles

2.3.1 Host Materials

The inorganic host crystal plays an important role in the efficiency of the upconversion processes. An ideal host for UC process to occur needs to possess high chemical stability, low lattice phonon energies that minimize non-radiative process and maximize radiative emissions and close lattice matches to the dopant ions. To the date, upconversion process have been studied in nano sized host matrices such as fluorides ($NaYF_4$, $NaYbF_4$, $NaGdF_4$, $NaLaF_4$, LaF_3), oxyfluorides (GdOF), oxides (La_2O_3, Lu_2O_3, Y_2O_3), halides ($BaCl_2$, $CsCdBr_3$, $Cs_3Y_2I_9$), oxysulfides (Y_2O_2S), phosphates (YPO_4) and vanadates (YVO_4). Halide hosts such as chlorides, bromides, and iodides normally exhibit low phonon energies (< 300 cm^{-1}) however, they are hygroscopic. Oxide hosts have relatively high phonon energies, generally higher than 500 cm^{-1}. Fluoride host is the most desirable host with high chemical stability and low phonon energies (~350 cm^{-1}) [28].

It is also known that the crystal structure of the host material significant influences upconversion efficiency. It has been observed that the crystalline host of hexagonal phase of $NaGdF_4$ or β-$NaYF_4$ exhibit higher upconversion efficiency relative to cubic counterparts [29]. This dependency is attributed to the different crystal fields around the Ln^{3+} in both crystal phases. Low symmetry hosts offer more uneven components around Ln^{3+} enhancing the electronic coupling between 4f energy levels and higher electronic configuration that subsequently increases f-f transition probabilities of dopant ions [30].

2.3.2 Lanthanide Dopant Ions

It is well established that lanthanide ions exhibit low absorption cross-sections with the consequence that they demonstrate low pump efficiency. Thus, the upconversion efficiency is low for single doped nanocrystals. In order to enhance the upconversion efficiency, co-doping of the host is used with two different lanthanide ions. One of the dopant ion acts as the activator and the other usually is Yb^{3+} as the sensitizer. It has been shown that this approach will favor a more efficient ETU mechanism.

Yb^{3+}, with an absorption band located at 980 nm, and a large absorption cross section in comparison to other lanthanide ions. The energy associated with the $^2F_{7/2} \rightarrow {}^2F_{5/2}$ transition is resonant with the most commonly used activators Er^{3+} and Tm^{3+}. In Figure 2.3, the visible and NIR emissions, which are obtained *via* the ETU process where Yb^{3+} is the sensitizer and Er^{3+} and Tm^{3+} as activators. It has been found that the best upconversion efficiency occurs when the sensitizer concentration is approximately 20 mol% and the concentration of the activator 0.5=2 mol % [28].

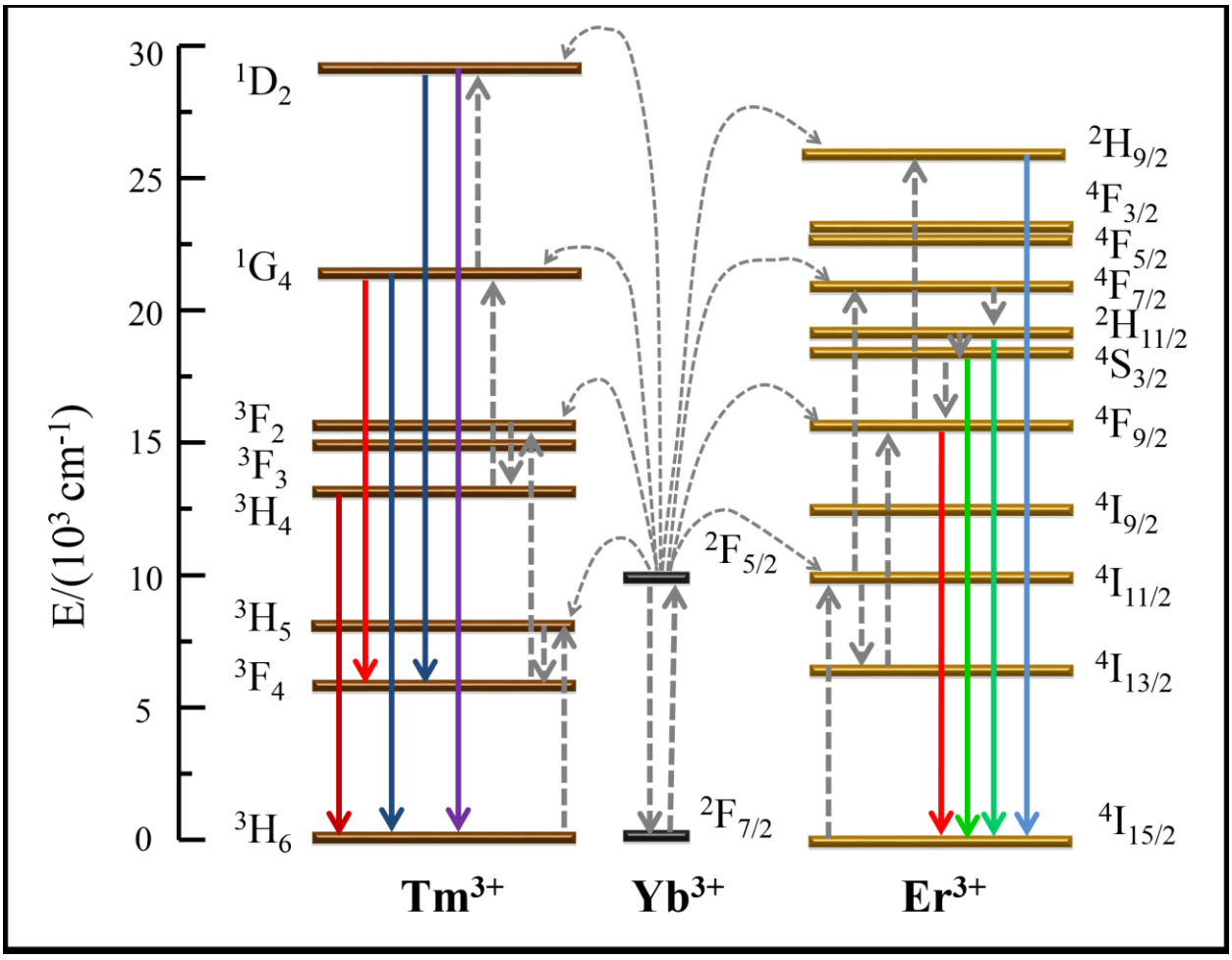

Figure 2.3: Partial energy diagram for the three trivalent lanthanide ions adopted from the "Dieke diagram" [28].

2.4 Magnetic Resonance Imaging (MRI)

In this section, the basic physical concepts of MR imaging will be summarized, and only the *in vivo* imaging on the basis of proton spin will be considered. The human body consist of approximately 63% protons (table 2.1), which includes both water and macromolecules [31]. Moreover, the high amount of water and the interaction of water with other macromolecules that determines the relaxation properties, allow the construction of an anatomical image for diagnostics purposes.

Table 2.1: Essential chemical elements composition in the body.

Element	Symbol
Major Elements: 99.3% of Total Atoms	
Hydrogen	H (63%)
Oxygen	O (26%)
Carbon	C (9%)
Nitrogen	N (1%)

2.4.1 Proton Nuclei and their Behaviour in the Magnetic Field

MRI is based on the basic principles of nuclear magnetic resonance (NMR). The basic concept of MRI involves the interaction of the hydrogen proton spins with an applied magnetic field. In the absence of an applied magnetic field, all the spin states of a given nucleus are degenerate. Each proton has its own magnetic field and their magnetic fields are oriented randomly. This random orientation results in a net magnetization of zero. Application of an external magnetic field results in the alignment of the proton spins either parallel or anti parallel to the magnetic field. However, over time the proton spins will align more in the parallel direction, which is the lower energy configuration (figure 2.4). Once equilibrium is achieved, the small net excess of the proton spins in the parallel direction gives a net magnetization in the direction of the external field [32].

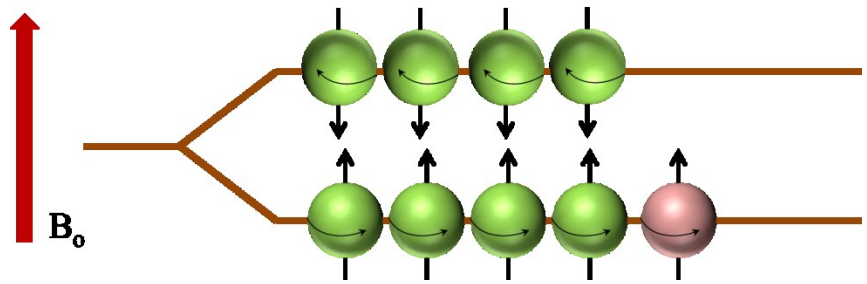

Figure 2.4: Behaviour of proton spins in a static external magnetic field.

2.4.2 Interaction with a Radiofrequency Field

Suppose equilibrium is disturbed such that it no longer lies along the z axis, precession motion will occur during the process as the spinning nuclei return to their natural equilibrium state (figure 2.5). The precession frequency ω_o, usually referred to as resonance frequency is directly proportional to the external applied field. Once equilibrium is achieved, the net magnetization is aligned along the direction of the external field and therefore does not precess.

The precession motion becomes more obvious when the second external field B_1, perpendicular to the B_o is applied. Additionally, B_1 rotates clockwise at frequency ω_o. If the field is applied for a short period of time, the net magnetization will be now precess slowly from the vertical axis (around B_o field) toward the B_1 field. This is an important concept in nuclear magnetic resonance where the absorption of energy by the nuclei resulting in the change of their spin orientation. Proton nuclei absorb radiation frequency of 60.0 MHz at a magnetic field strength of 1.41 Tesla, which is generally used in clinical MR imaging [33].

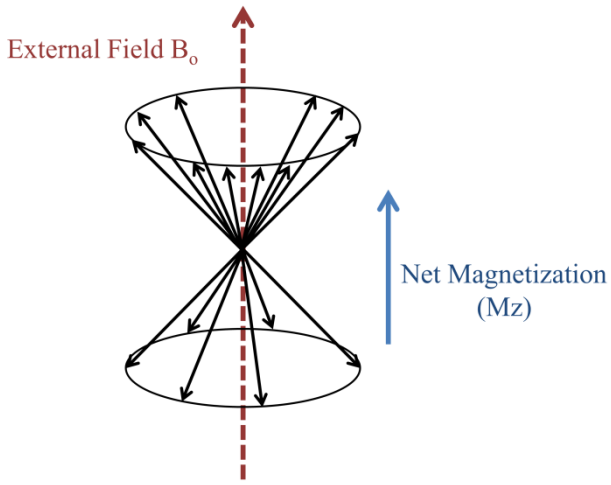

Figure 2.5: A collection of protons precess around the axis of an external field. A small excess if protons aligned with the field to produce a net magnetization (Mz) along the external field direction [33].

2.4.3 Relaxations

When a given population of nuclear spins aligned with a static magnetic field B_o is excited with an electromagnetic field B_1, perpendicular to B_o with a frequency equal to the precession frequency, also referred to as Larmor frequency, this causes the absorption of energy by the nuclear spins. From this perturbed state, the system relaxes back to its equilibrium state, which is the alignment of net magnetization (M_z) with the external field direction again. This process of relaxation is the observed NMR signal.

Therefore, in order to have NMR signal, the bulk magnetization M_z needs to be tilted away from the z-axis by the radiofrequency pulse (B_1). The tilt θ is proportional to the field strength of the pulse (B_1) and the time it was applied. Since the radiofrequency pulse tilts the vector M_o away from the vertical axis, the vector now has components M_x, M_y, M_z, tilted angle θ along with z axis and the angle φ lying in the xy-plane (figure 2.6). Since the angle φ is only dependent on the Larmor frequency, xyz systems is changed to x'y'z for the simplicity of mathematical expression of the relaxation, in which x' and y' axes rotate with the Larmor frequency.

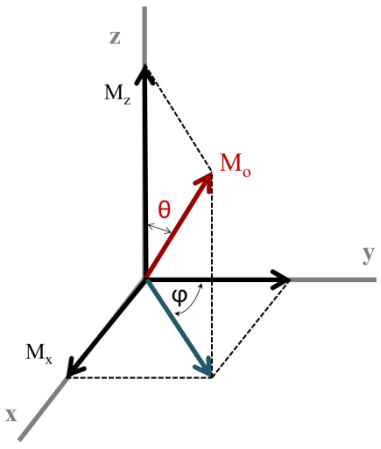

Figure 2.6: The vector Mo and its components Mx, My, and Mz [34].

During relaxation, the bulk magnetization M_o will gradually return to its equilibrium state, in which $M_{x'}$ and $M_{y'}$ will return to their initial zero values and M_z will be equal to M_o. This relaxation is first described by Bloch in 1946 and the equations below are now known as the Bloch equations [35].

$$\frac{dM_z}{dt} = -\frac{M_z - M_0}{T_1} \quad \text{(Equation 2.1)}$$

$$\frac{dM_{x'}}{dt} = -\frac{M_{x'}}{T_2} \qquad \frac{dM_{y'}}{dt} = -\frac{M_{y'}}{T_2} \quad \text{(Equation 2.2)}$$

2.4.3.1 Longitudinal Relaxation

The magnetization along the z axis is referred to as longitudinal magnetization (M_z) and the one perpendicular to this direction (in the xy-plane) is referred to as transverse magnetization (M_{xy}). Following a 90° radiofrequency (RF) pulse, M_z is converted is into M_{xy}. T_1 relaxation or longitudinal relaxation is the process where the system returns to equilibrium once the RF pulse is turned off. T_1 is called the spin-lattice time constant and characterizes the return to equilibrium along the z-direction (direction of B_o field). T_1 relaxation involves the exchange of thermal energy between the nuclei and the surrounding lattice. The recovery for longitudinal magnetization occurs in an exponential fashion (Equation 2.3) [33].

$$M_z = M_o(1 - e^{-t/T_1}) \quad \text{(Equation 2.3)}$$

2.4.3.2 Transverse Relaxation

Following a 90° radiofrequency (RF) pulse, the system eventually returns to its equilibrium. As there is a gradual gain of magnetization along the z direction, there is a decay magnetization in the transverse plane simultaneously. Therefore, the same factors accounts for T_1 relaxation also account for T_2 relaxation. The decay of traverse magnetization (M_{xy}) is referred to as T_2 relaxation or transverse relaxation. However, T2 relaxation also depends on other factors such as homogeneity of the external field and spin spin interaction which cause dephasing of the vector. Therefore, $T_2 \leq T_1$. Shown in figure 2.7, after 90° RF pulse, the precessing nuclear spins will gradually lose their coherence and fan out. The observed relaxation time due to the inhomogeneity of the magnetic field B_o and spin spin relaxation is expressed by T_2^* in equation 2.4 [33].

$$\frac{1}{T_2^*} = \frac{1}{T_2} + \frac{1}{T_{2\,\text{inhomo}}} \qquad \text{(Equation 2.4)}$$

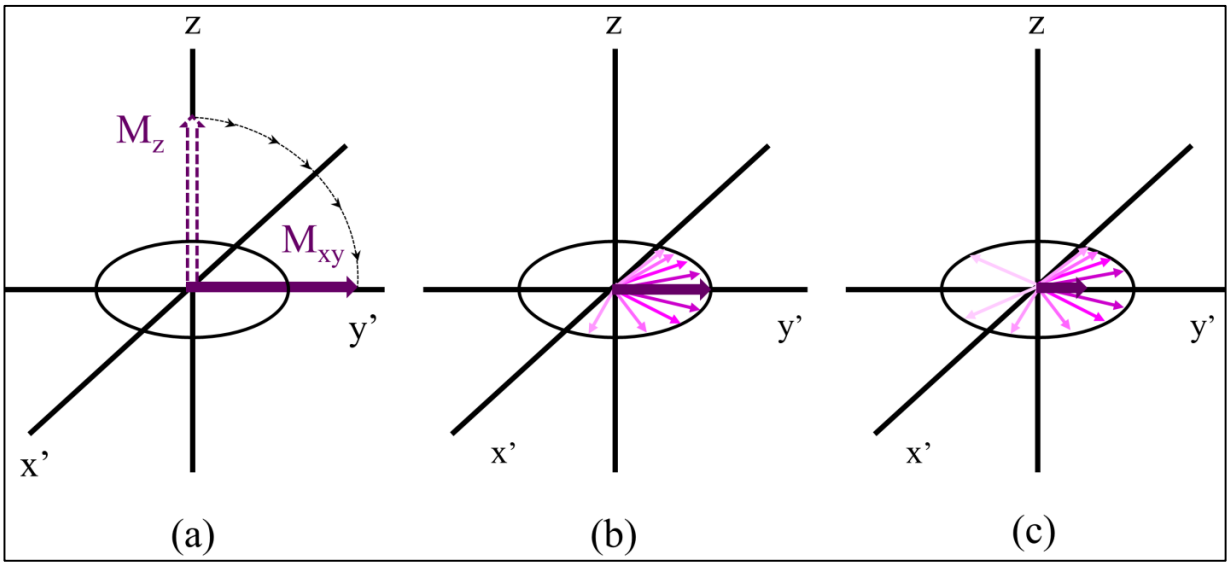

Figure 2.7: (a) M_z is converted to M_{xy} following 90° RF pulse; (b) and (c) gradual dephasing of M_{zy} vector [34].

2.4.4 Gadolinium as a Contrast Agent

The trivalent lanthanide ion (Gd^{3+}) contains the highest possible number of unpaired electrons (seven), which makes it the most paramagnetic among the stable metal ions. It functions to increases the relaxation rate of proton due to its paramagnetic property, and thus, enhancing the contrast of MR images. The clinical gadolinium based contrast agents are introduced into the body as a chelate form, through intravenous injection.

2.4.4.1 Relaxivity

The observed T_i (i=1, 2) of an aqueous solution containing a contrast agent can be written as consisting of a diamagnetic and paramagnetic contribution in the absence and presence of a contrast agent respectively (equation 2.5).

$$\frac{1}{T_{i,obs}} = \frac{1}{T_{1,d}} + \frac{1}{T_{i,p}} \qquad \text{(Equation 2.5)}$$

The paramagnetic contribution on the relaxation rate is directly proportional to the concentration of the contrast agent. If the concentration of Gd^{3+} is given in mM, the parameter r_1 is defined as proton relaxivity and can be determined from the slope of the equation 2.6, where c is the concentration of the contrast agent (equation 2.6). Relaxivity is normally expressed in $mM^{-1}\ s^{-1}$. The relaxivity value directly refers to efficiency of the contrast agent in the enhancement of relaxation rate of water protons [36].

$$\frac{1}{T_{i,obs}} = \frac{1}{T_{1,d}} + r_i c \qquad \text{(Equation 2.6)}$$

2.4.4.2 Paramagnetic Relaxation of the Water Protons

Free Gd^{3+} ions are not effective in affecting the relaxation of water molecules due to the rapid rotation of the small ions. Attaching Gd^{3+} ion to molecules such as diethylene triamine pentaacetic acid (DTPA) has the effect of slowing down the tumbling rate of the system, at a rate closer to the resonance frequency of water protons. The paramagnetic relaxation of water arises from dipole-dipole interactions between the protons nuclear spins and the fluctuating local magnetic field caused by the unpaired electron spins of the paramagnetic substance [33].

The effect caused by a contrast agent on the surrounding water molecules depends on the distance between the paramagnetic ion and the protons of the water molecules. The major contribution of the overall paramagnetic relaxation is from the inner-sphere water molecules, which directly bound to the paramagnetic ion. The proton relaxivity results from the interaction of Gd^{3+} electron spins and the water protons in the first coordination sphere *via* exchange of water molecules with the bulk solvent (figure 2.8). The paramagnetic center could also affect water molecules hydrogen bonded to the ligand (usually to its carboxylate or phosphonate groups). The contribution of the second sphere protons to the relaxation rate are however negligible in many cases [36, 37].

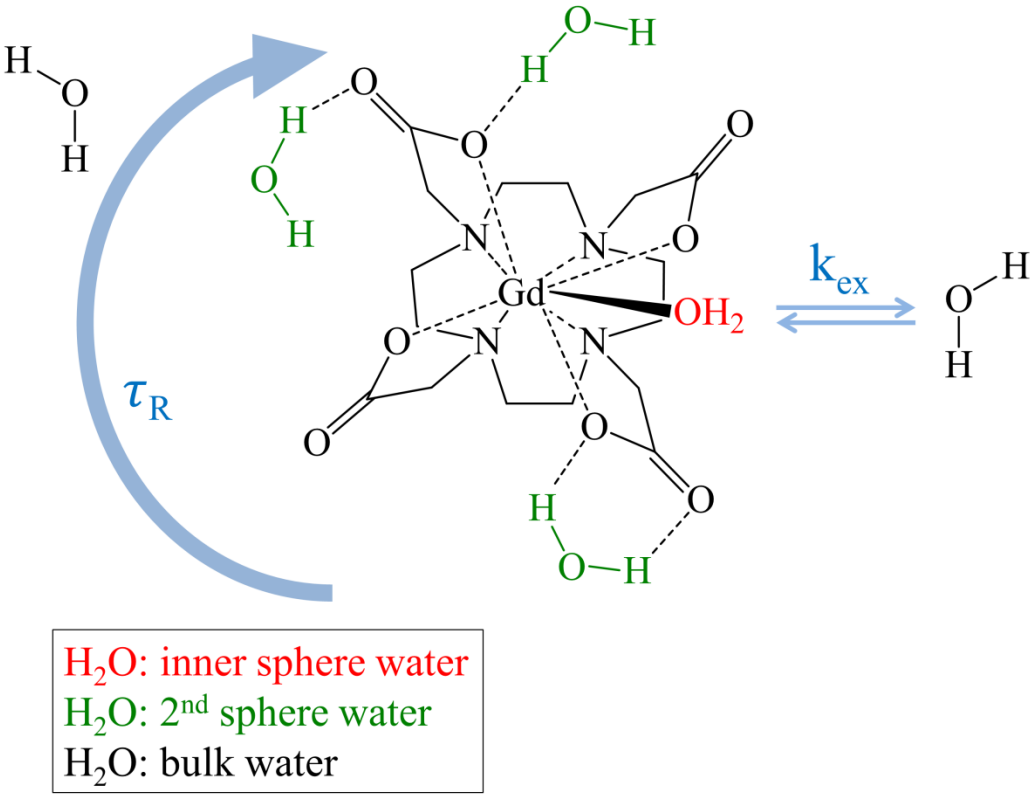

Figure 2.8: Inner-sphere, 2nd sphere and bulk water, τ_R: rotational correlation time, k_ex: water/proton exchange rate [37].

The development of gadolinium based contrast agent mainly involves in enhancing the proton relaxivity from the inner-sphere which depends on a large number of parameters. To name a few:

- proton exchange rate, $K_{ex} = 1/\tau_m$ (τ_m is the life time of a solvent water molecules in the inner sphere of the complex)
- rotational correlation time, τ_R
- hydration number q (number of water molecules coordinated to the Gd^{3+} center)

Rotation is perhaps the most critical parameter in the optimization of proton relaxivity at a given field strength. Experiment has been shown that by decreasing the τ_R from 1 ns to 0.1 ns, it has effect of increasing the bound relaxation rate (1/T). Moreover, the relaxation enhancement will approach a maximum as the inverse of the overall correlation time (in consideration of the rotational frequency, proton exchange rate and the relaxation rate) approaches the Larmor precessional frequency [37].

Chapter Three: Experimental and Characterization Techniques

3.1 Thermal Decomposition Synthesis of Upconverting Nanoparticles $NaYF_4$: Tm^{3+}/Yb^{3+}

The $NaYF_4$:Tm^{3+} (0.5%)/Yb^{3+} (25%) upconverting nanoparticles were synthesized *via* the thermal decomposition method established by our group [7]. Two major steps were involved in the synthesis: (1) preparation of the trifluroacetate lanthanide precursors, (2) synthesis of the oleate capped nanoparticles.

3.1.1 Procedure for the Preparation of Precursor: Lanthanides Trifluoacetate Salts

0.5 mol % of Tm_2O_3(0.0024 g), 25 mol% of Yb_2O_3 (0.1232 g) and 74.5 mol % of Y_2O_3 (0.2103 g) were added to a 50 mL round bottom flask. The addition of 10 mL (1:1) mixture of water/trifluoroacetic acid gave a white solution, which was refluxed at 80 ℃ for 12 hours until the solution turns clear. The solvents were evaporated at 60 ℃ and the products were brought to dryness.

3.1.2 Procedure for the Synthesis of Upconverting Nanoparticles $NaYF_4$: Tm^{3+}/Yb^{3+}

The precursor prepared in previous step were stored in an oven of 60 ℃ prior the synthesis of nanoparticles. To synthesize the nanoparticles $NaYF_4$: Tm^{3+}/Yb^{3+}, 25 mL (1:1) mixture of oleic acid and 1-octadecene was added to a 100 mL three-neck round bottom flask, referred as reaction flask. Under vacuum, the solution was stirred and degassed at 150 ℃ for 30 minute. The solution was purged using argon and the temperature was maintained at 150 ℃. After 15 minutes, the temperature was raised to 310 ℃.

To the 50 mL round bottom flask containing lanthanides trifluoacetate precursor, 15 mL of (1:1) mixture of oleic acid and 1-octadecene was added. The mixture was stirred and degassed at 45 ℃, 75 ℃ and 125 ℃ for 5 minutes respectively. Then, the precursor solution was injected into the reaction flask using a syringe and pump system at rate of 0.75 mL/min at 310 ℃ . As soon as the injection was completed, the mixture was left to react for one hour, at 310 ℃, under a gentle flow of argon. The nanoparticles were collected *via* precipitation using ethanol and washed with mixture of hexane and ethanol (1:7) few times [7].

3.2 Procedure Optimization for the Synthesis of $NaYF_4$: Tm^{3+}/Yb^{3+} in Thermal Decomposition Method

In order to obtain monodisperse $NaYF_4$: Tm^{3+}/Yb^{3+}, an optimization of the procedure was carried out. Shown in the table 3.1, the parameter varied was the injection rate while the temperature and reaction were kept constant.

Table 3.1: Variation of parameters in thermal decomposition method.

Temperature	Injection Rate (mL/min.)	Reaction time (min)
310 ℃	*1.0*	60
310 ℃	*0.75*	60
310 ℃	*0.30*	60

3.3 Synthesis Procedure of Ultra-small $NaGdF_4$: Tm^{3+}/Yb^{3+}

In a 100 mL three-neck round bottomed flask, 0.745 mmol of $GdCl_3 \cdot 6H_2O$ (0.2769 g), 0.005 mmol of $TmCl_3 \cdot 6H_2O$ (0.0019 g), 0.25 mmol of $YbCl_3 \cdot 6H_2O$ (0.0969 g), 4 mL of oleic

acid and 15 mL of 1-octadecene were added. Under vacuum, the solvents were stirred and degassed for 5 minutes at room temperature, and raised up to 150 ℃ and maintained at this temperature for 30 minutes. The mixture was then cooled to room temperature. A 10 mL of methanolic solution of NH_4F (4 mmol, 0.1500g) and NaOH **(**4 mmol, 0.1000 g**)** was injected using a syringe and pump system at a rate of 0.35 mL/min (Harward Apparatue Econoflow). The solution was let stirred at room temperature for 24 hours. Finally, the solution was slowly heated at 265 ℃ for 30 min. under argon. The nanoparticles were collected *via* precipitation using ethanol and washed with mixture of hexane and ethanol (1:7) few times [38].

3.4 Procedures for Surface Modifications of Nanoparticles towards Water Dispersibility and Multimodalities

In order to render the oleate capped upconverting nanoparticles water dispersible. Two approaches were employed: silica coating and polymer coating.

3.4.1 Silica Coating

3.4.1.1 Silica Coating Procedure for Nanoparticles of Size approximately 20 nm

In a glass vial, 40 mg of wet oleate capped nanoparticles and approximately 1 g of surfactant Igepal CO-520 were dispersed in 12 mL of cyclohexane by sonication for 15 min. While the mixture was stirring, 100 μL of ammonium hydroxide (28.0 – 30.0 % NH_3 basis) was added dropwise. The solution was let stirred for 30 min. Finally, 75 μL tetraethyl orthosilicate (TEOS) was added dropwise into the solution, and the reaction was continued for another 48 hours. The silica coated upconverting nanoparticles were precipitated using acetone and collected by centrifugation. The nanoparticles were washed with ethanol several times. The nanoparticles were kept wet to be used in the future experiments of surface modifications.

3.4.1.2 One Pot Synthesis Procedure of Azide Functional Silica Coated UCNPs

In order to functionalize the silica nanoparticles with the azide functional silane, same procedure used for the silica coating described in section 3.3.1.1 was followed. However, after 24 hours of reaction, and without precipitating the nanoparticles, 30 μL of 3-azidopropyltriethoxysilane (AzPTES) was added to the reaction vial. The solution was stirred for another 24 hours. The final nanoparticles were precipitated using acetone, centrifuged and washed with ethanol. The nanoparticles were kept wet to be used in the future experiments of surface modifications.

3.4.1.3 The Click Reaction: Covalent Conjugation of Alkyne-(Gd-DOTA) to Silica Coated UCNPs

10 mg of azide modified silica coated UCNPs and 150 μL of aqueous alkyne_(Gd-DOTA) (0.018 mmol) were mixed and dispersed in 2 mL of Millipore water and sonicated for 15 min. Under stirring, 54 μL of aqueous sodium ascorbate solution (0.0018 mmol) was added dropwise. The mixture was stirred for 5 minutes prior the slow addition of 9 μL of aqueous copper sulfate (0.0091 mmol). The color of the solution changed slowly from light blue to light yellowish. The mixture continuously stirred for 24 hours and the modified nanoparticles were precipitated with acetone and washed with Millipore water [39].

3.4.2 Polymer Coating Approach: Procedure for Polymer Coating of Ultra-small Upconverting Nanoparticles (US-UCNPs)

5mg of oleate capped, US-UCNPs and 1 mL of 0.2 M PEG diacid (pH = 3) were added into a 1.5mL-eppendorf tube. The sample was placed in a thermomixer and was shaked at 300

rpm and 40 ℃ for one hour. 0.5 mL of hexane was added to the aqueous solution to form an organic/aqueous phase. The resulting mixture was shaken for 30 additional min. The organic layer was removed and discarded. The unbound polymer was removed *via* dialysis.

3.5 Synthesis Procedure for Alkyne Gd-DOTA [41, 42, 43]

3.5.1 Synthesis of 2-bromo-*N*-(propargyl)acetamide (1)

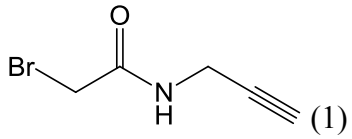

(1)

Dry dichloromethane (150 mL) and bromoacetyl chloride (4.5 mL, 54 mmol) were added to a 500 mL oven dried round bottom flask. Under a nitrogen atmosphere and at 0℃ (cooled using an ice bath), a solution of propargyl amine (3.7 mL, 54 mmol) and DIPEA (9.6 mL, 54 mmol) in dry dichloromethane was added dropwise *via* a cannula. Once the addition was complete, the solution was allowed to warm to room temperature and stirred for 45 min. The reaction mixture was concentrated *in vacuo*. The crude product was purified by column chromatography (silica gel, 1:1 of ethyl acetate and hexane).

3.5.2 Synthesis of tri-tert-butyl 2, 2', 2'' - (1,4,7,10-tetraazacyclododecane-1,4,7-triyl) triacetate (2)

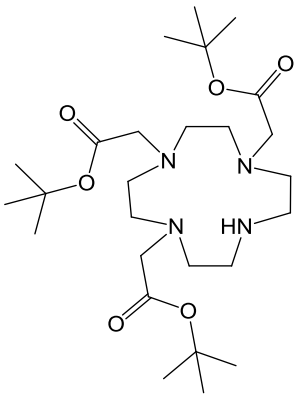

(2)

Compound **2** synthesized using the following procedure. In a 100 mL flask, 1 g (5.8 mmol) of 1,4,7,10-tetraazacyclododecane was dissolved in 50 mL of dry CH_3CN (HPLC grade) followed by an addition of 1.61 g (19.1 mmol) $NaHCO_3$. A solution of 3 mL (20.3 mmol) t-butylbromoacetate (98%) in 5 mL of CH_3CN was added dropwise to the suspension and the mixture was stirred at room temperature for 12 h. The reaction was carried out under an argon atmosphere. The residue was filtered through a pad of Celite and the filtrate was evaporated to dryness. The residual solid was treated with excess diethyl ether to precipitate the product, which was then isolated by filtration.

3.5.3 Synthesis of tri-tert-butyl 2, 2', 2'' - {10-[2-oxo-2-(2-propyn-1-ylamino)ethyl]-1,4,7,10-tetraazacyclododecane-1,4,7-triyl)} triacetate (3)

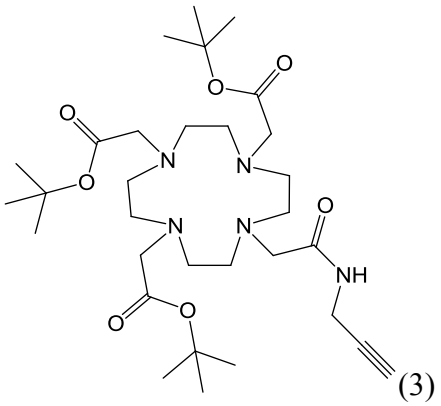

(3)

Compound **3** synthesized using the following procedure. Compound **2** (0.100 g, 0.194 mmol), compound **1** (0.026 g, 0.194 mmol) and K_2CO_3 (0.028 g, 0.194 mmol) were added to 100 mL of CH_3CN in a 250 mL flask containing. The mixture was heated under reflux for 12 h. The suspension was filtered through a pad of Celite and the solvent was removed *in vacuo*. The product was purified by column chromatography (alumina, 98:2 DCM/MeOH) yielding a white solid (Compound 3).

3.5.4 Synthesis of 2, 2', 2'' - {10-[2-oxo-2-(2-propyn-1-ylamino)ethyl]-1,4,7,10-tetraazacyclododecane-1,4,7-triyl)} triacetic acid (4)

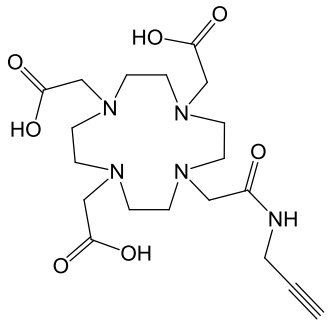

(4)

Compound **4** synthesized using the following procedure. Compound **3** was dissolved in 30 mL (1:1) mixture of CH_2Cl_2 and trifluoroacetic acid (TFA). The solution was stirred for 12 h at room temperature. The reaction flask was placed in the warm oil bath and the solvents were let evaporated slowly. The residue was suspended in 20 mL of methanol, and solvent were removed *in vacuo* to remove the traces of TFA. This step was repeated two more times with methanol, and then three times with CH_2Cl_2. The final evaporation of solvent yielded a golden oil (compound 4).

3.5.5 Synthesis of gadolinium 2, 2', 2'' -{10-[2-oxo-2-(2-propyn-1-ylamino)ethyl]-1,4,7,10-tetraazacyclododecane-1,4,7-triyl)}triacetate (5)

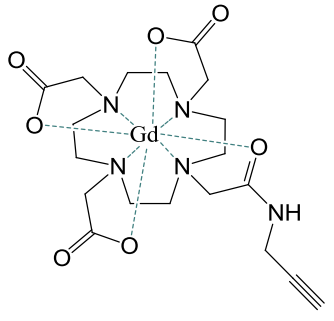

(5)

Compound **5** synthesized using the following procedure.100 mg (0.226 mmol) of compound **5** and 89.2 mg (0.240 mmol) of $GdCl_3 \cdot H_2O$ were dissolved in 5 mL of deionized water, and the pH was adjusted to 6 with 0.1 M KOH solution. The solution was stirred at 60 ℃ for 12 h. The solution was treated with CHELEX-100® three times, and the solvent was removed *in vacuo*. The resulting oil was dissolved in minimal volume of methanol. The addition of excess of diethyl ether yields a white solid. Chromatographic purification (HPLC) yielded the corresponding Gd(III) complex (compound 5).

3.6 Characterizations Techniques

3.6.1 Fourier Transform Infrared (FTIR) Spectroscopy

The FTIR spectra presented in this thesis were measured using a Nicolet 6700 FTIR spectrometer. KBr were prepared as the background.

3.6.2 Transmission Electron Microscopy (TEM)

TEM analysis was performed using a Philips CM200 microscope operating at 200 kV equipped with a charge-coupled device (CCD) camera (Gatan). Prior to analysis, the nanoparticles were dispersed in toluene to yield a 0.5 wt% solution. A few drops of the resulting solution were evaporated on a formvar/carbon film supported on a 300 mesh copper grid (3 mm in diameter).

3.6.3 X-Ray Powder Diffraction (XRPD)

XRPD patterns were measured using a Scintag XDS-2000 Diffractometer equipped with a Si(Li) Peltier-cooled solid state detector, a Cu Kα source using a generator power of 45 kV and 40 mA, divergent beams (2 mm and 4 mm), and receiving beam slits (0.5 mm and 0.2 mm). The scan range was set from 10-90° 2θ with a step size of 0.02° and a count time of 2 s. All samples were measured using a quartz "zero background" disk.

3.6.4 Upconversion Luminescence Spectroscopy

The luminescent emission properties of the lanthanide-doped nanoparticles were measured following 980 nm excitation using a Coherent 6-pin fiber-coupled F6 series (core) fiber. For the spectroscopic studies, the sample was dispersed in toluene (1 wt%) and placed in a Hellma, QS quartz cuvette (1 cm path length). The upconverted visible emission were collected at 90 degrees with respect to the incident beam and then dispersed by a 1 m Jarrell-Ash Czerny-Turner double monochromator with an optical resolution of ~0.15 nm. The visible emissions from the sample exiting the monochromator were detected by a thermoelectrically cooled

Hamamatsu R943-02 photomultiplier tube. A preamplifier, model SR440 Standard Research Systems, processed the photo-multiplied signals and a gated photon counter model SR400 Standard Research Systems data acquisition system was used as an interface between the computer and the spectroscopic hardware.

3.6.5 Mass Spectrometry

Mass spectrometry measurements were performed using a LC-MSD TOF (Agilent) with ESI as the ionisation source and in the mass range of 100–2000 m/z.

3.6.6 X-Ray Photoelectron Spectroscopy (XPS)

The XPS analysis of PEG and lysine grafted ultra-small $NaGdF_4$: Tm^{3+}, Yb^{3+} was carried out using a PHI 5600-ci spectrometer (Physical Electronics, Eden Prairie, MN, USA). A few drops of the aqueous suspension of nanoparticles were deposited on gold-coated silicon substrates which had been cleaned with a TL1 solution, which is a mixture of ultrapure water, 30% H_2O_2 and 25% ammonia (Fisher, IL, USA; 5:1:1), at 80°C for 10 min). A monochromatic aluminum X-ray source (1486.6 eV, 300 W) was used to record the survey spectra (1400-0 eV) with charge neutralization. The detection angle was set at 45º with respect to the surface and the analyzed area was 0.005 cm^2.

3.6.7 Dialysis of PEG grafted $NaGdF_4$: Tm^{3+}, Yb^{3+} Nanoparticles

Following the synthesis of PEG grafted $NaGdF_4$: Tm^{3+}, Yb^{3+} nanoparticles, dialysis was performed in order to remove any unbound polymer. A membrane size 10 kD (Spectra/Por #6,

Spectrumlabs) was used and the nanoparticles were dialyzed for 24 h in ultrapure water. The water was changed three times during the 24 hours and the sample-to-volume ratio was kept to at 1:1000.

3.6.8 Dynamic Light Scattering (DLS)

The hydrodynamic diameter and the zeta potentials of the nanoparticles were measured using dynamic light scattering (DLS, Malvern Zetasizer) The analyses were performed at 20°C in water. The analyses were performed at 25°C. The viscosity and refractive index of water were fixed at 0.8872 cP and 1.33, respectively. Three measurements were performed for each sample.

3.6.9 Neutron Activation Analysis

Neutron activation studies were carried out to determine the concentration of gadolinium in the samples. The concentration of gadolinium is necessary to determine the T_1 and T_2 relaxivities. Samples to be analyzed consisted of the dialyzed nanoparticle dispersions in de-ionized water. Samples prepared in plastic eppendorf tubes (100 µL) were introduced in the SLOWPOKE reactor for 100 seconds at a neutron flux of 1.0×10^{12} n.cm^{-2} s^{-1}. The ^{153}Gd (T1/2 = 280 d) activities was measured. The monitors were counted 10 cm from a germanium detector. Activities were corrected for decay time and after a period of 21 days, the vials were counted with a Ge(Li) detector for 1000 seconds.

3.6.10 ^{1}H NMR Relaxivity Studies

The proton relaxation rate was measurement using time domain NMR relaxometer (Bruker Minispec 60 MHz, 37 ℃). Dilution volumes of 400 µL (100, 75, 50, 25% v/v) of dialyzed suspensions were placed into 6.0 mm NMR tubes. Longitudinal and transversal relaxation times (T_1 and T_2) were performed in triplicate. The relaxation rates ($1/T_1$ and $1/T_2$) were plotted against Gd^{3+} concentration values obtained from neutron activation studies, and the relaxivities (r_1 and r_2) were obtained from the slopes of the graphs.

3.6.11 Magnetic Resonance Imaging and Contrast Agent Assessment

In vitro assays of the contrast agent performance of ultra-small $NaGdF_4$: Tm^{3+}, Yb^{3+} grafted with PEG and lysine were accomplished using a 1T ASPECT MR Scanner. The samples were placed in a bowl of nanopure water. The following T_1 weighted parameters were used: echo time: 10.8 ms, repetition time 400 ms, a flip angle of 90°.

Chapter Four- Results and Discussions

4.1 Synthesis of Upconverting Nanoparticles (UCNPs)

Upconverting nanoparticles may be synthesized by several different methods [7, 44, 45]. In this thesis, thermal decomposition and modified hydrothermal methods were used to produce UCNPs of size approximately 20 nm and 5 nm respectively. It is extremely important to obtain monodisperse nanoparticles such that the size dependent physiochemical properties may be investigated. Hence, an optimization of the thermal decomposition synthesis procedure was carried out.

4.1.1 Controlled Size, Morphology and Particle Size Distribution of UCNPs $NaYF_4$: Tm^{3+}, Yb^{3+} *via* the Thermal Decomposition Method

The thermal decomposition synthesis method requires the optimization of several parameters such as the ratio of oleic acid/1-octadecene, precursor injection rate, reaction temperature and reaction time since they affect the size, morphology, crystal phase and particle size distribution of the UCNPs. Naccache [38] carried out a study that provides the optimal parameters for the thermal decomposition synthesis of $NaGdF_4$ nanoparticles. In this thesis, the parameters obtained by Naccache [38] were used with the exception of the precursor injection rate. Thus, the precursor injection rate was investigated in order to ascertain its effect on the particle size distribution and morphology. This was carried out by varying the injection rate from 0.3 mL/min. to 1.0 mL/min. and maintaining the temperature at 310℃ and the reaction time of 60 min. The temperature and reaction time were selected based on the previous work carried out in the Capobianco research group.

Transmission electron microscopy (TEM) analysis was carried out to investigate the effect of varying the injection rate on the particle size and morphology (Figures 4.1a and b).

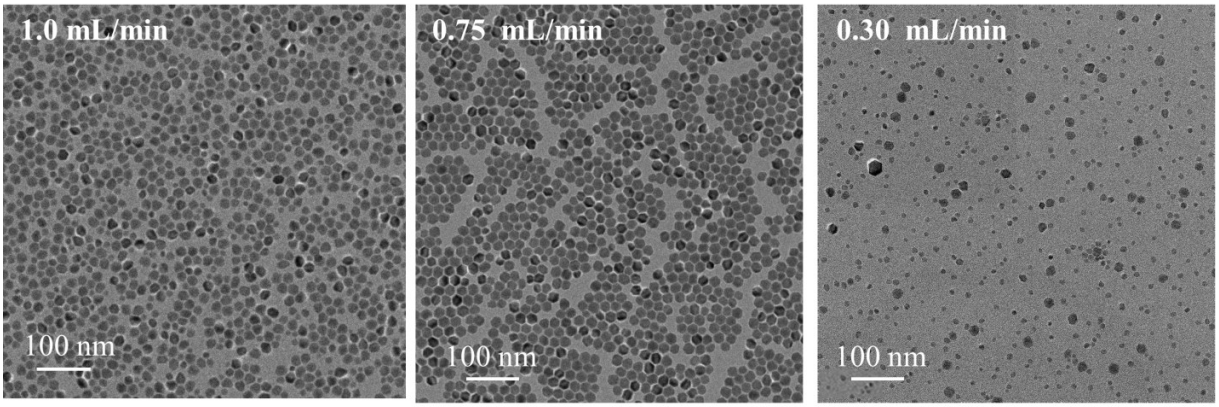

(a)

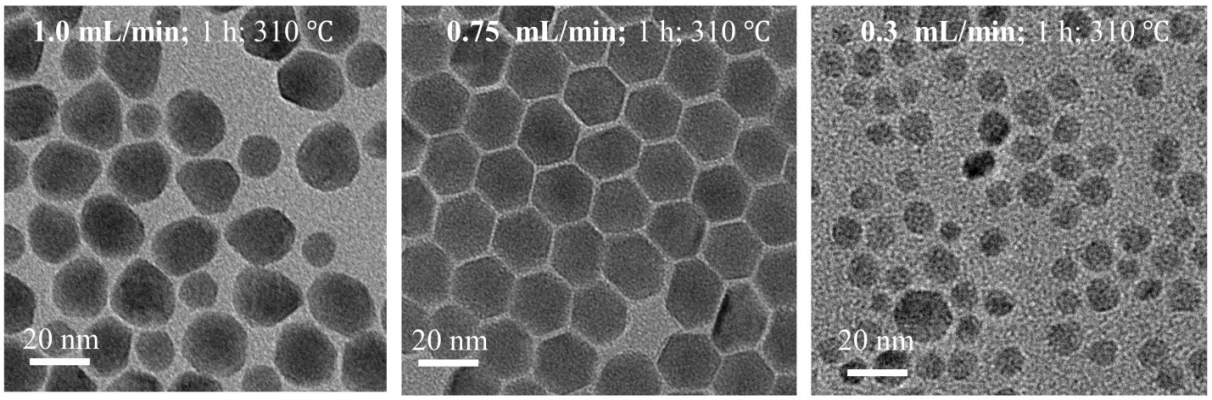

(b)

Figure 4.1: Transmission electron microscopy images of $NaYF_4$: Tm^{3+}, Yb^{3+} nanoparticles at (a) low magnification (30,500x) and (b) high magnification (179,000x) prepared as function of precursor injection rate.

It is evident from the TEM images (low and high magnification) that the injection rate of 0.75 mL/min produced the most uniform morphology and size of $NaYF_4$ UCNPs. Particle size distribution analyses were carried out for the nanoparticles synthesized at different precursor injection rates and the narrowest distribution was observed at 0.75 mL/min (Figure 4.2) whereas a double distribution was observed for the 1.0 and 0.3 mL/min injection rates. The mean particle

size for the three precursor injection rates is reported in Table 4.1. The calculated standard deviation was the lowest for the 0.75 mL/min injection rate.

Table 4.1: Mean particle size of $NaYF_4$: Tm^{3+}, Yb^{3+} nanoparticles prepared as function of precursor injection rate.

Precursor injection rate	1.0 mL / min.	0.75 mL / min.	0.30 mL / min.
Mean particle size (nm)	18.7 ± 4.5	19.4 ± 2.0	11.0 ± 3.1

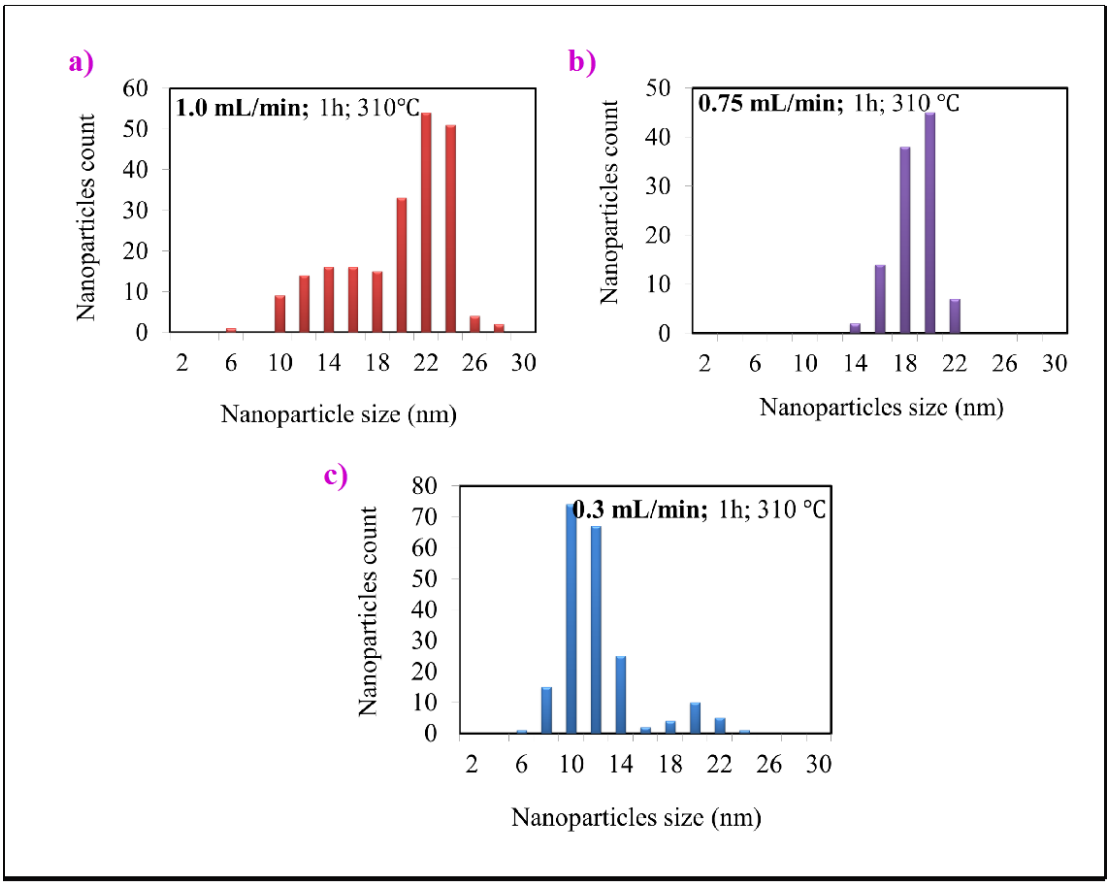

Figure 4.2: Particle size distribution of $NaYF_4$: Tm^{3+}, Yb^{3+} nanoparticles prepared as function of precursor injection rate.

In the classical model of crystal growth in solution, the particles increase in size by the reaction with monomers (ions, atoms or molecules) present in solution. Therefore, different growth regimes may be distinguished that are dependent on the concentration of the monomers, which is related to the rate at which the monomers are added or removed from the particle surface. Ostward ripening [46, 47] is an observed phenomenon thermodynamically driven by concentration gradient. Oswald ripening is simply the process whereby small particles dissolve and release monomers while larger particles grow by the uptake of the monomers. That is because larger particles are energetically more stable than smaller particles. The other mechanism, which has been proposed is the La Mer mechanism [48, 49, 50], which described the separation of nucleation and growth in time. A high rate of nucleation leading to the burst of nuclei formation in a short period, consequently, the monomer concentration drops drastically below a point where no further nucleation is possible. Eventually, a slow rate of growth leading to a long growth period compared to the nucleation period. There have also been reports that the growth could be the combination of the two mechanisms [51, 52]. The rate of addition of the precursors in the synthesis of UCNPs plays an important role in the process of crystal nucleation and growth. Crystal nucleation and growth are competitive processes. During the precursor injection period, as more precursors materials are being added into the reaction flask, new nuclei will be produced while previously formed nuclei continue to grow resulting in a polydisperse sample as observed for the rate of 0.3 mL/min (Figure 4.2c). At a faster addition rate of 1.0 mL/min, the precursors are introduced at a much faster rate. This condition favors nucleation over growth since a higher concentration of decomposed precursor results in the formation of a large number of nuclei followed by growth over the length of the reaction time. Since a greater number of nuclei are formed at the higher addition rate, the particle size in expected to increase

as more decomposing precursor would be available to contribute to the growth. This is clearly shown in Figure 4.1a and b and Table 4.1. Particle size distribution analyses showed that an injection rate of 0.75 mL/min produced the narrowest distribution whereas the 1.0 mL/min and 0.3 mL/min injection rate showed a double distribution indicating the polydispersity of the samples.

The high resolution TEM images (Figure 4.3) of the synthesized nanoparticles (injection rate of 0.75 mL/min) showed that the particles are roughly spherical. In addition, from the high resolution TEM, the distance between the lattice fringes was measured to be 0.311 nm which corresponds to the d-spacing for the (111) lattice plane in the cubic structure of $NaYF_4$.

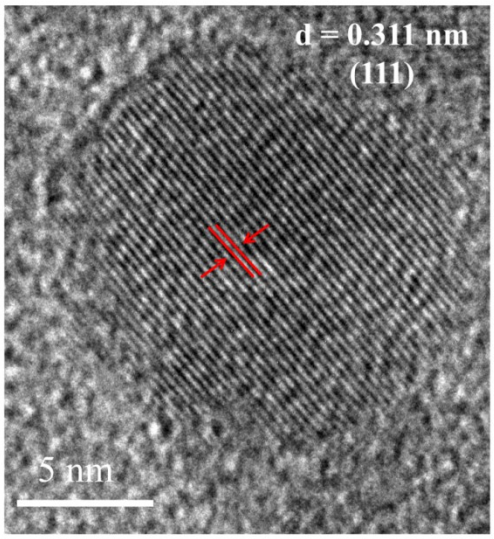

Figure 4.3: Lattice fringes observed in TEM image of $NaYF_4$: Tm^{3+}, Yb^{3+} upconverting nanoparticles. The sample was prepared with 0.75 mL/min injection rate.

The X-ray powder diffraction patterns for the samples synthesized using different injection rates are shown in Figure 4.4. Also shown in Figure 4.4 are the reference diffraction patterns for hexagonal (JCPDS 27-699) and the cubic (JCPDS 6-0342) phase of bulk $NaYF_4$. In

addition, to the diffraction peaks of the cubic phase, the patterns also showed additional diffraction peaks (marked by *) that could not be attributed to neither phase. However, we were not yet able to identify the origin of these peaks and we simply attribute them to possible impurities [53].

The XRD patterns were analyzed to ascertain the extent of formation of the cubic phase as a function of injection rate (Table 4.2). A maximum in the percentage of cubic phase was observed at an injection rate of 0.75 mL/min. The percent cubic phase was found to be the lowest at an injection of 0.3 mL/min suggesting that the conditions did not favor crystal growth.

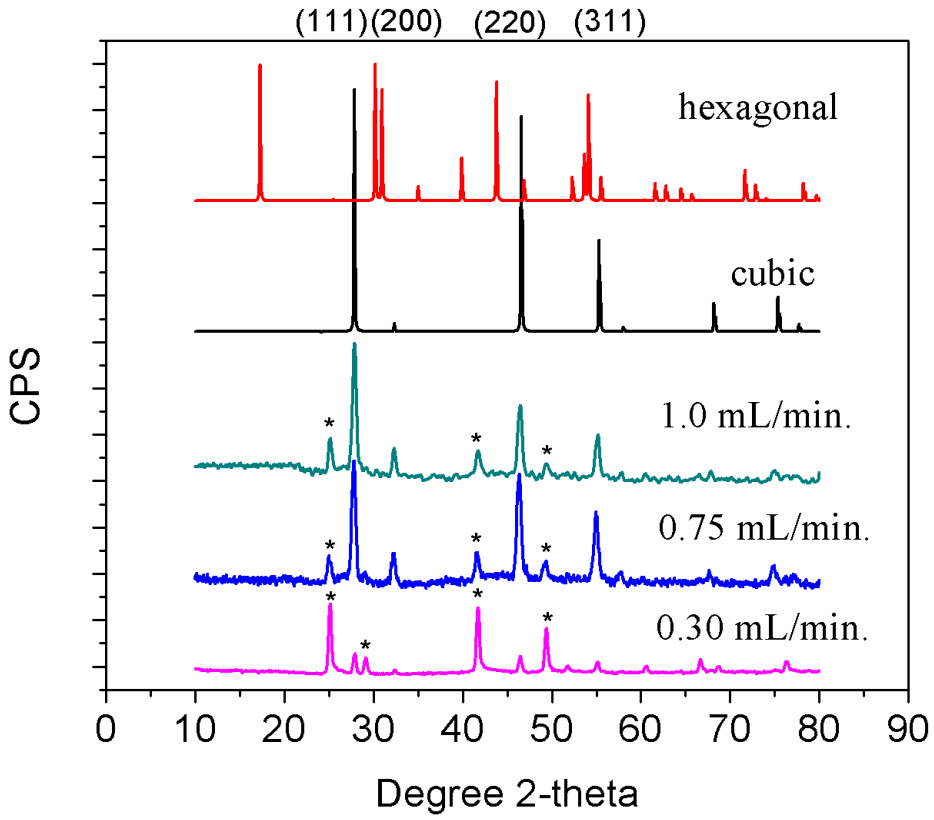

Figure 4.4: X-ray powder diffraction patterns of $NaYF_4$: Tm^{3+}, Yb^{3+} nanoparticles prepared as function of precursor injection rate.

Table 4.2: Cubic phase composition in the samples of $NaYF_4$: Tm^{3+}, Yb^{3+} prepared with different injection rate.

Precursor injection rate	% of pure cubic phase	% of impurities
1.0 mL/min.	82.1	17.9
0.75 mL/min.	88.0	12.0
0.30 mL/min.	23.7	76.3

The $NaYF_4$: Tm^{3+}, Yb^{3+} upconverting nanoparticles showed emissions in the blue, red and NIR regions (Figure 4.5) following 980 nm excitation. The nanoparticles were prepared with different injection rate from 1.0 mL/min to 0.3 mL/min and were dispersed in toluene. All three samples showed the characteristic emissions of Tm^{3+} ions. The blue emissions located at 449 nm and 480 nm corresponded to $^1D_2 \rightarrow {}^3F_4$ and $^1G_4 \rightarrow {}^3H_6$ transitions respectively. The red emission located at 650 nm was assigned to the $^1G_4 \rightarrow {}^3F_4$ transition. A strong intensity of NIR emission was centered at 800 nm, originated from the transition of $^3H_4 \rightarrow {}^3H_6$. All three spectra were normalized to the NIR emission and the changes in the intensity of the blue emissions were observed and summarized in Table 4.3. Although we observed a slight change in the blue/NIR ratio for the UCNPs prepared at different injection rate, the changes in the blue/NIR ratio is within 10% (within experimental errors). Since the three different injection rate resulted UCNPS of different particle size distribution, for example, the injection rate of 0.75 mL/min has resulted in UCNPs of 19.4 $\pm$ 2.0 nm. The injection rate of 0.30 mL/min has resulted the smallest particle size 11.4 $\pm$ 2.0 nm. Theoretically, smaller nanoparticles with more surface defects are expected to have smaller blue/NIR ratio since upconversion is a multiphoton process, the generation of blue emissions requires absorption of three photons, whereas the NIR emission requires only two photons (Figure 2.3). Therefore, small nanoparticles with more surface defects will be less

efficient than the large nanoparticles in the upconversion processes. The results obtained were consistent with the theory. The injection rate of 0.75 mL/min which resulted in the largest particle size with the narrowest particle size distribution among the three showed the highest blue/NIR ratio. And the injection rate of 0.3 mL/min resulted in smallest particle sizes showed smallest blue/NIR ratio.

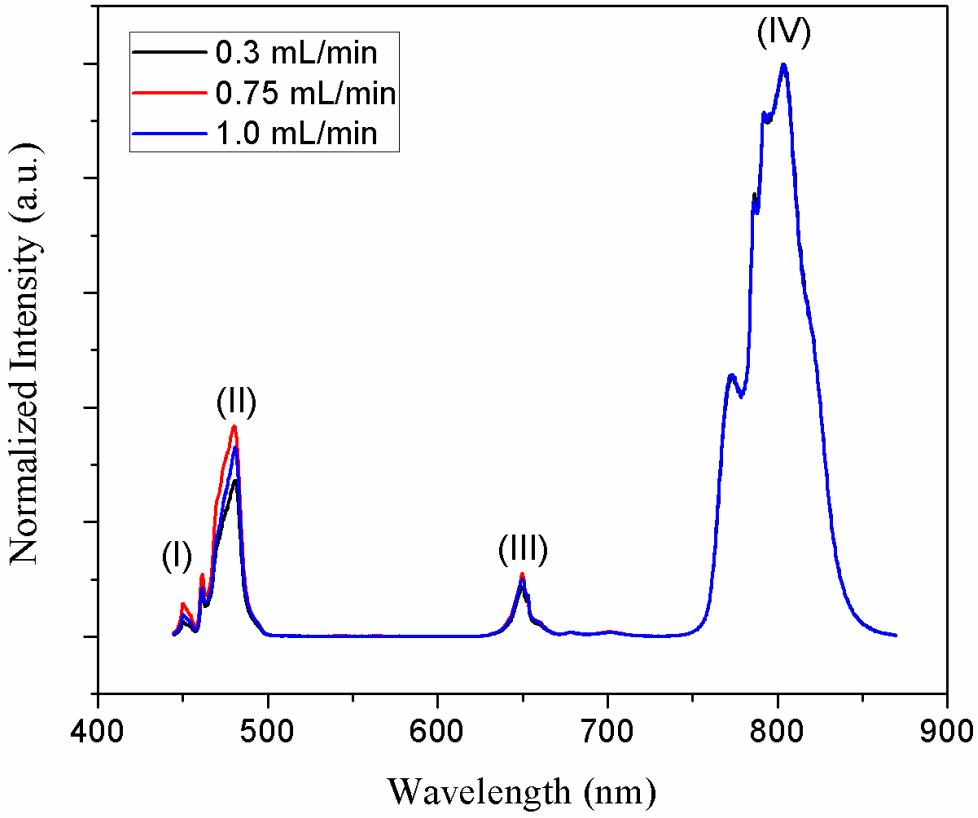

Figure 4.5: Upconversion emission spectra of $NaYF_4$: Tm^{3+}, Yb^{3+} nanoparticles (1 w% dispersion in toluene) prepared as function of precursor injection rate, following 980 nm excitation. Upconversion emission was ascribed to the transitions of (I) $^1D_2 \rightarrow {}^3F_4$, (II) $^1G_4 \rightarrow {}^3H_6$, (III) $^1G_4 \rightarrow {}^3F_4$, (IV) $^3H_4 \rightarrow {}^3H_6$

Table 4.3: Blue/NIR luminescence ratio for of $NaYF_4$: Tm^{3+}, Yb^{3+} nanoparticles as function of injection rate.

Injection Rate (mL/min)	Blue/NIR Ratio
0.3	0.11
0.75	0.15
1.0	0.13

4.1.2 Synthesis of Ultra-small $NaGdF_4$: Tm^{3+}, Yb^{3+}

For applications in nanomedicine, there are rigorous requirements. Particularly for multimodal bioimaging, a small particle diameter (<5 nm), bright luminescence, and non-toxicity are required. Despite the recent progress in the synthesis of ultra-small lanthanide-doped nanocrystals, the development of reproducible facile synthetic routes that yield reliably ultrasmall fluoride inorganic nanocrystals is still a tremendous challenge. In this section, we report the synthesis of ultra-small $NaGdF_4$: Tm^{3+}, Yb^{3+} nanoparticles and their potential application as bimodal probes (optical and magnetic resonance). The requirement for ultra-small $NaGdF_4$ nanoparticles stems from the fact that the concentration of Gd^{3+} ions will increase at the surface since the surface to volume ratio increases as the size of the nanoparticle decreases thus providing a greater water Gd^{3+} interaction, which is a primordial requirement for MRI.

The thermal decomposition synthesis of UCNPs requires high temperature to decompose the trifluoroacetates. Thus, the reaction favors the growth stage of nanocrystals, resulting in nanoparticles which are larger than 10 nm. The synthesis of UCNPs as small as 3 – 5 nm while maintaining a narrow size distribution requires a synthetic route that yields reliably ultra-small UCNPs.

The parameters which may be controlled in the thermal decomposition synthesis and which may impact the formation of the nanoparticles are: reaction time, reaction temperature, precursor addition rate and the oleic acid capping ligand to 1-octadecene non co-ordinating ligand solvent ratio. All of these parameters have been studied previously by Naccache [38] and the author demonstrated the difficulties in controlling these parameters to obtain ultra-small nanoparticles. Thus, we employed the synthetic route described in Section 3.3 of this thesis, which has been shown to produce high quality ultra-small UCNPs.

The TEM and particle size distribution revealed the synthesized $NaGdF_4$: Tm^{3+}, Yb^{3+} nanoparticles have a high degree of uniformity in size (Figure 4.6a) and shape (Figure 4.6b). The mean particle size was determined to be 5.1 ± 0.5 nm in a size range of 4 – 6 nm. Therefore, the synthesis procedure yields nanoparticles, which are ultra-small and highly monodisperse.

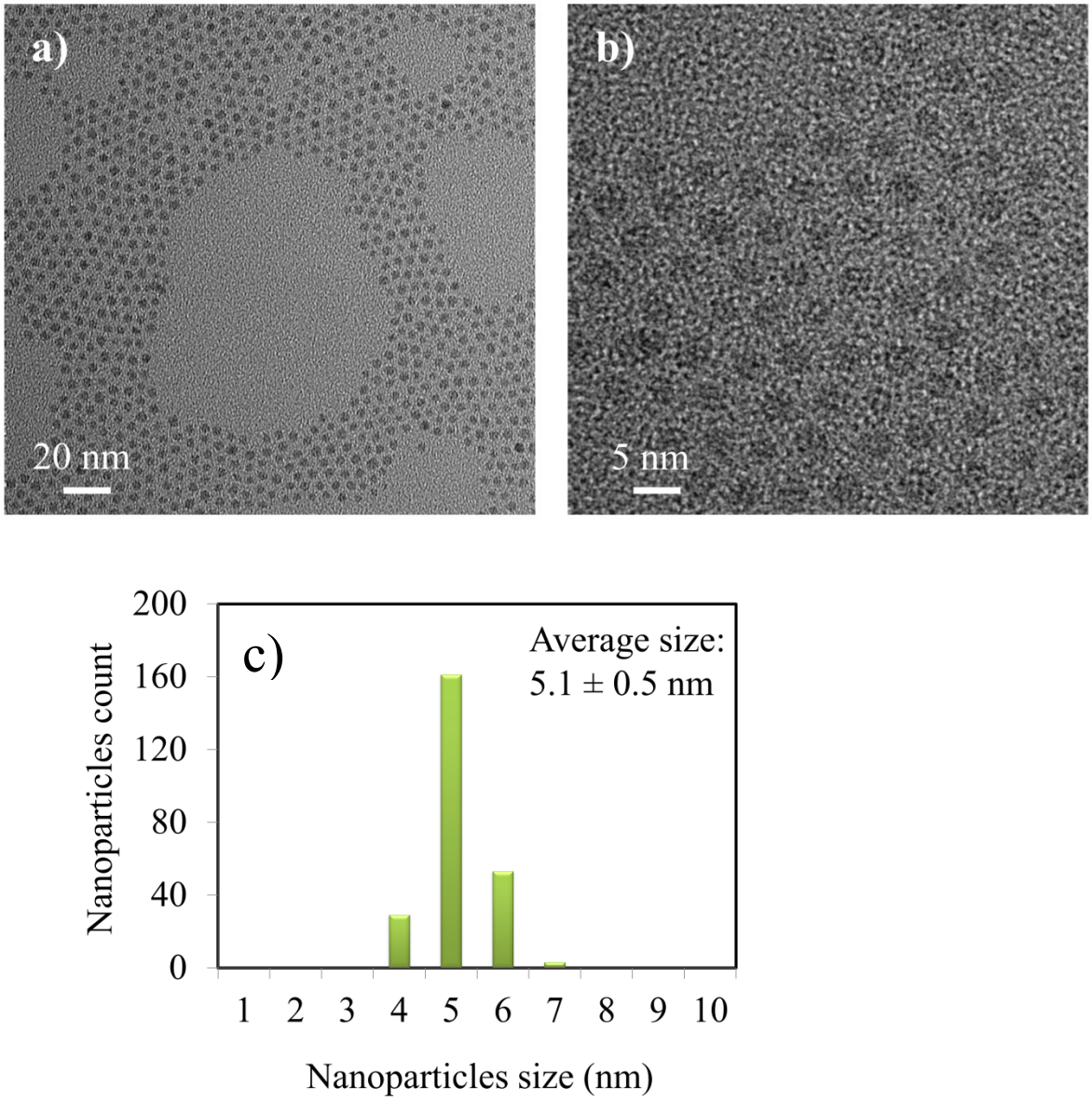

Figure 4.6: Transmission electron microscopy images of ultra-small $NaGdF_4$: Tm^{3+}, Yb^{3+} nanoparticles at a) low magnification (65,000X), b) high magnification (140,000X). Panel c) shows particle size distribution of ultra-small $NaGdF_4$: Tm^{3+}, Yb^{3+}.

The selected area electron diffraction (SAED) pattern of the particles (Figure 4.7) can be indexed to the (111), (200), (220) and (311) planes of the standard cubic structure. The emission spectrum obtained upon 980 nm excitation of the ultra-small $NaGdF_4$: Tm^{3+}, Yb^{3+} is shown in Figure 4.8. Four Tm^{3+} emission bands were observed. The two bands observed in the blue

regions of the spectrum 450-480 nm were assigned to the $^1D_2 \rightarrow {}^3F_4$, and $^1G_4 \rightarrow {}^3H_6$ transitions respectively. A weak red emission at 640-670 nm and an intense NIR emission at 750-850 nm were assigned to the $^1G_4 \rightarrow {}^3F_4$ and $^3H_4 \rightarrow {}^3H_6$ transitions respectively. It should be noted that the transitions are a result of the upconversion process which has been discussed extensively over the past years.

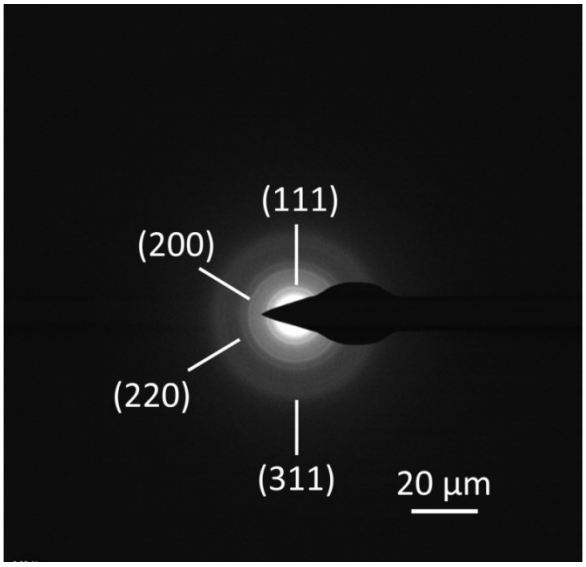

Figure 4.7: The selected area electron diffraction (SAED) pattern of ultra-small $NaGdF_4$: Tm^{3+}, Yb^{3+}.

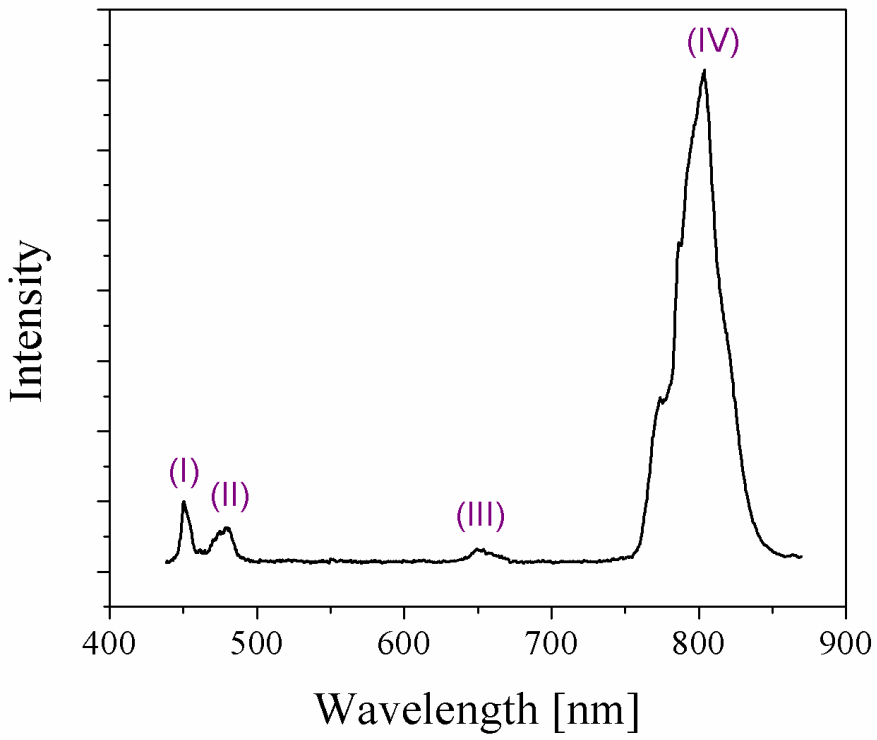

Figure 4.8: Upconversion emission spectra of ultra-small $NaYF_4$: Tm^{3+}, Yb^{3+} nanoparticles following 980 nm excitation. Upconversion emission was ascribed to the (I) $^1D_2 \rightarrow {}^3F_4$, (II) $^1G_4 \rightarrow {}^3H_6$, (III) $^1G_4 \rightarrow {}^3F_4$, (IV) $^3H_4 \rightarrow {}^3H_6$.

4.2 Surface Modifications of the Nanoparticles towards Water Dispersibility and Multimodalities

We have used two different synthetic routes to produce UCNPs that show a narrow particle size distribution as well as uniformity in their morphology. However, both synthetic routes resulted in the formation of hydrophobic nanoparticles. They have no intrinsic aqueous dispersibility and lack functional moieties for subsequent biological functionalization due to the hydrophobic oleate capping ligand. This is a major drawback in biomedical research. Post synthesis surface modifications have been employed to render these nanoparticles dispersible in aqueous media such as ligand exchange with citrate [54], silica coating [55, 56], oxidation of the

oleate capping ligand to azelaic acid and the removal of the oleate ligand by a simple acid treatment [57] that produces ligand free water dispersible nanoparticles.

Two approaches could be used for the design of a bimodal contrast agent. The optical properties could be strictly from the core of the upconverting nanoparticles. The Gd^{3+} ions, which provide T_1 contrast enhancement in MRI, could be functionalized onto the surface of UCNPs as Gd^{3+} complex or Gd^{3+} ions may be incorporated directly in the UCNPs.

In order to functionalize Gd^{3+} chelates onto the crystalline surface of the UCNPs, silica coating is a suitable approach since it would provide water dispersibility and covalent bonding of the Gd^{3+} chelates to the surface of UCNPs. $NaYF_4$: Tm^{3+}, Yb^{3+} was chosen as the core of the nanoconstruct to provide the optical properties required and the MRI signals will arise strictly from the Gd^{3+} chelates anchored to the surfaces of the UCNPs.

The second approach of incorporating of Gd^{3+} ions in the nanocrystal required maintaining a high concentration of Gd^{3+} ions per nanoparticle without having any adverse effect on the upconverting property. Ultra small nanoparticles provide high surface area to volume ratio, therefore, ultra-small $NaGdF_4$: Tm^{3+}, Yb^{3+} may be used as the base material for the design of the bimodal contrast agent. Moreover, considering water molecules must have direct contact with Gd^{3+} ions on the surface of the nanocrystals, polymer coating is the preferred approach compared to silica coating.

4.2.1 Silica Coating

The technique used to perform silica coating experiment was the reverse micro-emulsion. The hydrophobic UCNPs were dispersed in non-polar solvent such as cyclohexane. Koole *et al*. discussed the role of the surfactant Igepal CO-520, which functioned not only to ligand exchange

with the capping ligand oleate, but also formed a micelle around individual nanoparticles. The formation of micelles allows water, ammonium hydroxide and TEOS (tetraethyl orthosilicate) to migrate into the core of micelles [58] (Figure 4.9). The hydrolysis of TEOS was catalyzed in basic conditions, resulting in the formation of a silica shell around the nanoparticles. The ratio of concentration of UCNPs/TEOS was optimized in order obtain individually coated UCNPs.

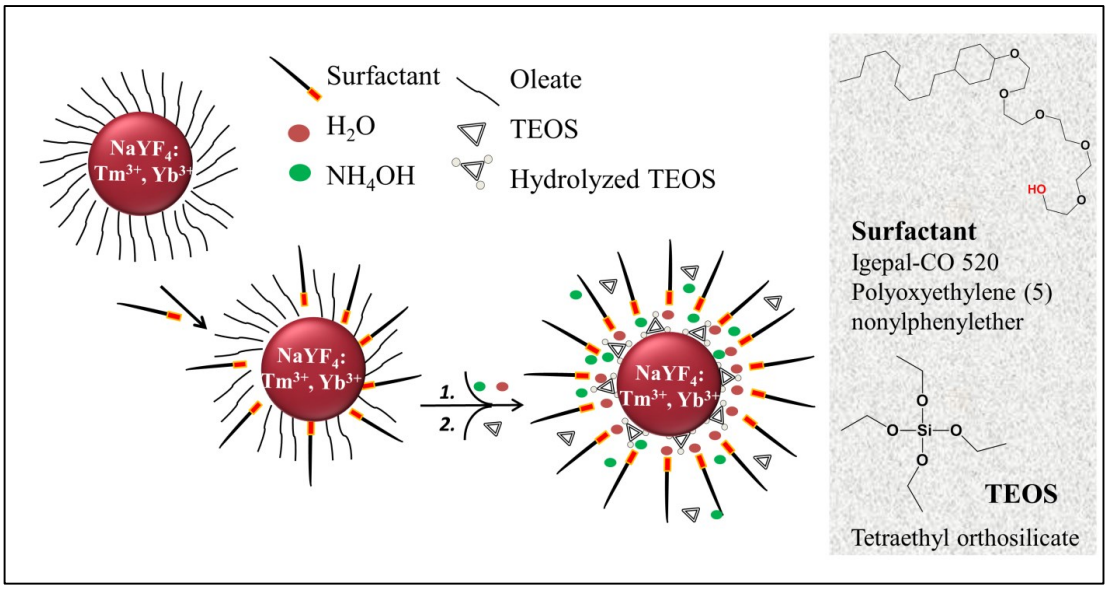

Figure 4.9: Proposed mechanisms for silica coating of nanoparticles [58].

The starting materials, UCNPs $NaYF_4$: Tm^{3+}, Yb^{3+} were prepared using the following conditions: 310 ℃, 0.75 mL/min of injection rate, one hour of reaction time. The as-synthesized UCNPs with a mean particle size of 19.4 ± 2.0 nm were dispersible only in non polar solvents. Following silica coating, we observed a thin layer of silica shell of approximately 4-5 nm grown on each nanoparticle based on the TEM images in Figure 4.10c. Hence, the mean particle size of the silica coated UCNPs increased to 27.6 ± 3.0 nm (Figure 4.10d). One problem often encountered in silica coating of nanoparticles is agglomeration. Due to optimal reaction conditions, both TEM images and particle size distributions (Figure 4.10) showed the success of silica coating of UCNPs. Therefore, not only was the narrow size distribution maintained, more

importantly silica coated UCNPs are hydrophilic. The formation of the silica shell on the UCNPs was verified to be silica by Fournier transform infrared (FTIR) spectroscopy. The FTIR spectrum shown in figure 4.11a shows the characteristic peak of the oleate capping ligand before surface modification: the peaks observed at 2925, 2852 cm $^{-1}$ corresponded to the C-H stretching from the carbon chains and the partial C=O bond stretching of carboxylate groups at 1562, 1467 cm $^{-1}$. These characteristic peaks of the oleate capping ligand are not observed in the FTIR spectrum (Figure 4.11b) of the silica coated UCNPs. The spectrum (Figure 4.11b) showed the following peaks, which were attributed to the asymmetrical and symmetrical O-Si-O stretching at 1090 and 953 cm $^{-1}$ respectively; Si-C stretching at 800 cm $^{-1}$ and O-H bending at 1637 cm $^{-1}$. Therefore, the silica shell on the UCNPs was confirmed by FTIR

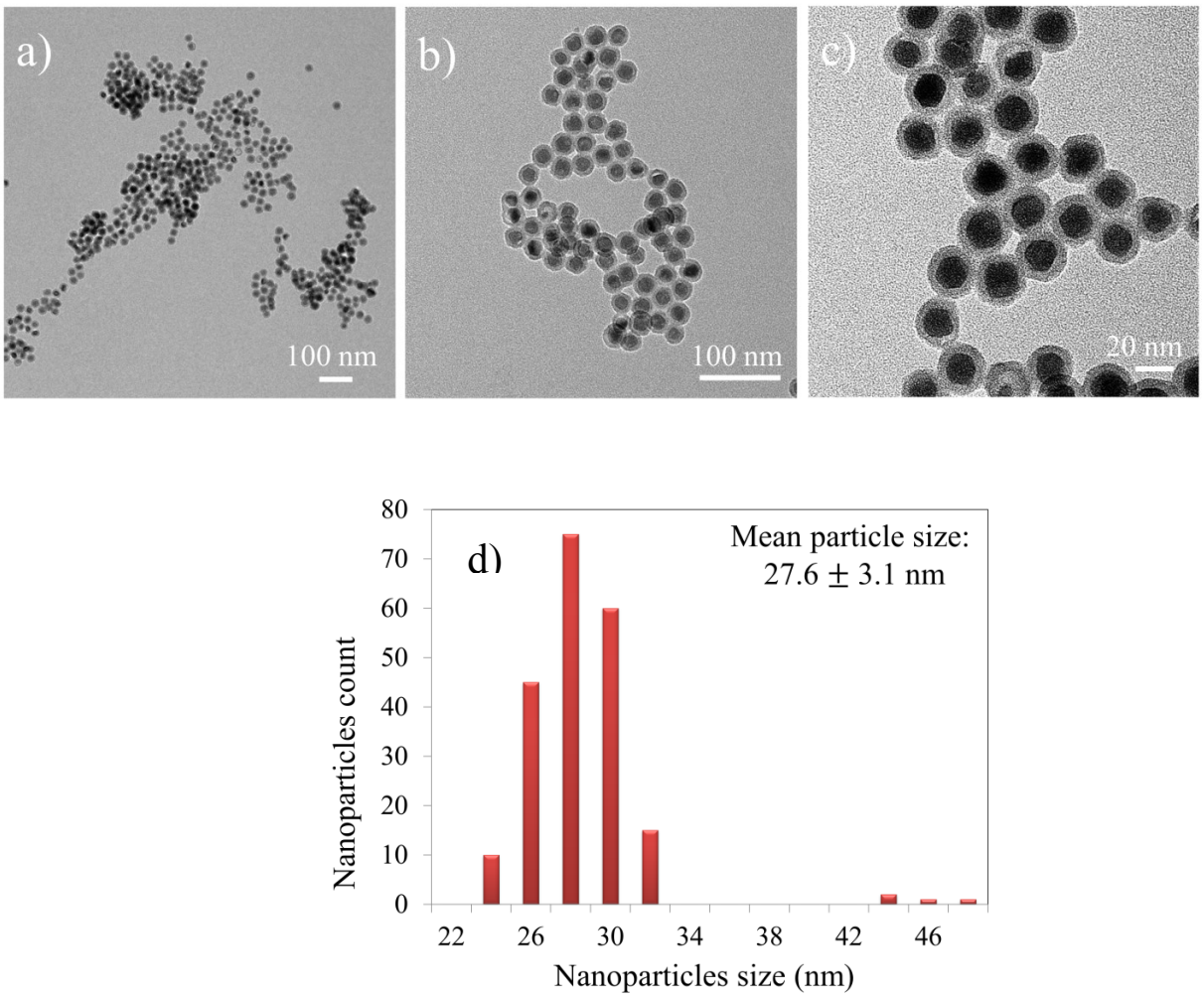

Figure 4.10: Transmission electron microscopy of silica coated $NaYF_4$: Tm^{3+}, Yb^{3+} nanoparticles at magnifications a) 22,000X; b) 57,000X and c) 135,000X; d) particle size distribution of silica coated $NaYF_4$: Tm^{3+}, Yb^{3+} nanoparticles.

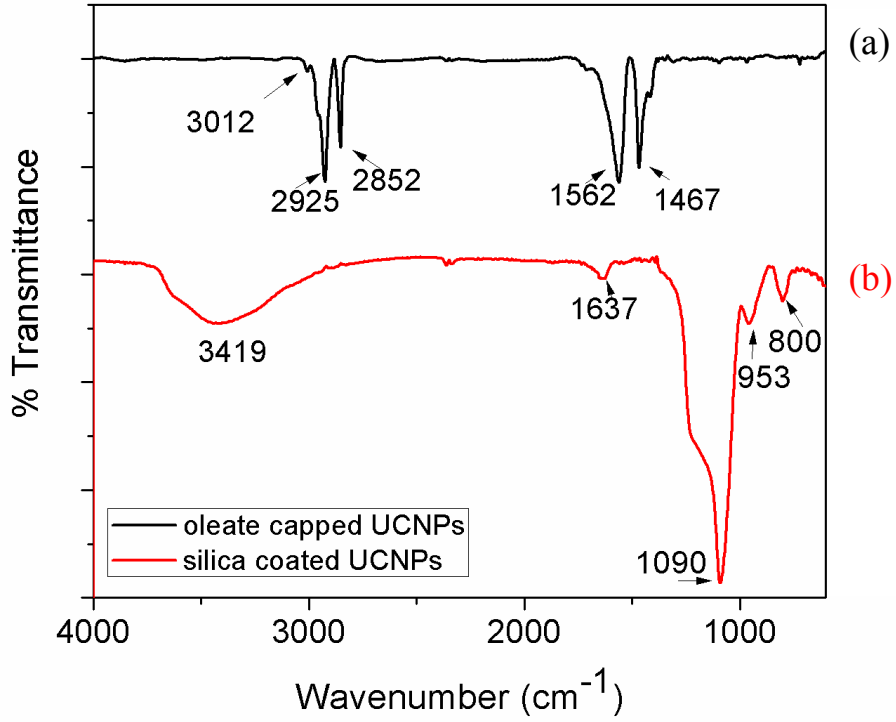

Figure 4.11: FT-IR spectra of (a) oleate capped and (b) silica coated UCNPs $NaYF_4$: Tm^{3+}, Yb^{3+} nanoparticles.

4.2.1.1 Introducing Azide Functional Groups on the Surface of Silica Coated UCNPs

The FTIR results of the silica coated UCNPs showed the presence of hydroxyl groups on the surface. In order to covalently conjugate the Gd^{3+} chelates, for example, Gd-DOTA to silica coated UCNPs, it is necessary to modify the silica surface to provide functional groups, which will allow covalent bonding to Gd-DOTA. Among all conjugations techniques, the click reaction introduced by Sharpless *et al.* has been shown to be the most convenient route since it is easy to perform and provides high yield. It involves a 1,3-dipolar cycloaddition between an azide and an alkyne functional group, which results in a 1,2,3-triazole [59]. The first step involves the surface modifications of silica coated UCNPs to bear the N_3 terminal group, which was confirmed by comparing FTIR spectra. Before the modification with azide silane, Figure 4.12a showed the

characteristics peaks of silica at 3419, 1087, 958 and 800 cm $^{-1}$ (the assignments were discussed in the previous section). The appearance of the peaks at 2937 cm $^{-1}$ (alkyl C-H stretching) and at 2107 cm $^{-1}$ (N≡N asymmetric stretching) in the FTIR spectrum (Figure 4.12b) suggested the presence of azide groups on the surfaces of silica coated UCNPs following the surface modification.

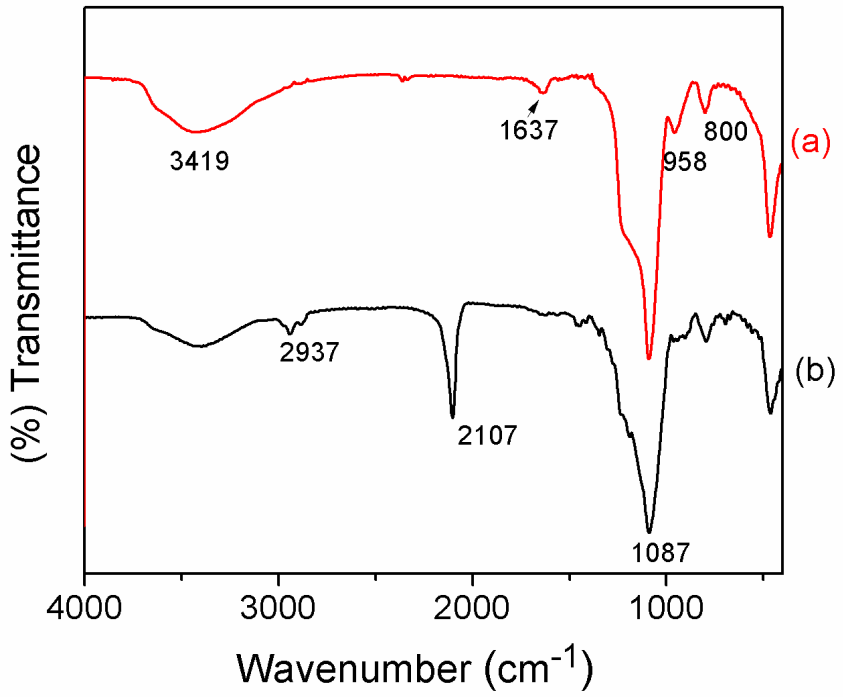

Figure 4.12: FT-IR of (a) silica coated UCNPs and (b) azide modified UCNPs

4.2.1.2 Functionalization of Silica Coated UCNPs with Alkyne Gd-DOTA *via* the Click Reaction

Silica coating has rendered the UCNPs water dispersible and the addition of the azide group allowed for the functionalization of the UCNPs with the alkyne Gd-DOTA for the design of a bimodal (optical, MRI) nanoconstruct for bioimaging using the click reaction. The reaction

to produce the alkyne terminated Gd-DOTA is shown in Appendix A. Figure 4.13 shows the reaction scheme for the conjugation of the alkyne Gd-DOTA to the surface of the UCNPs.

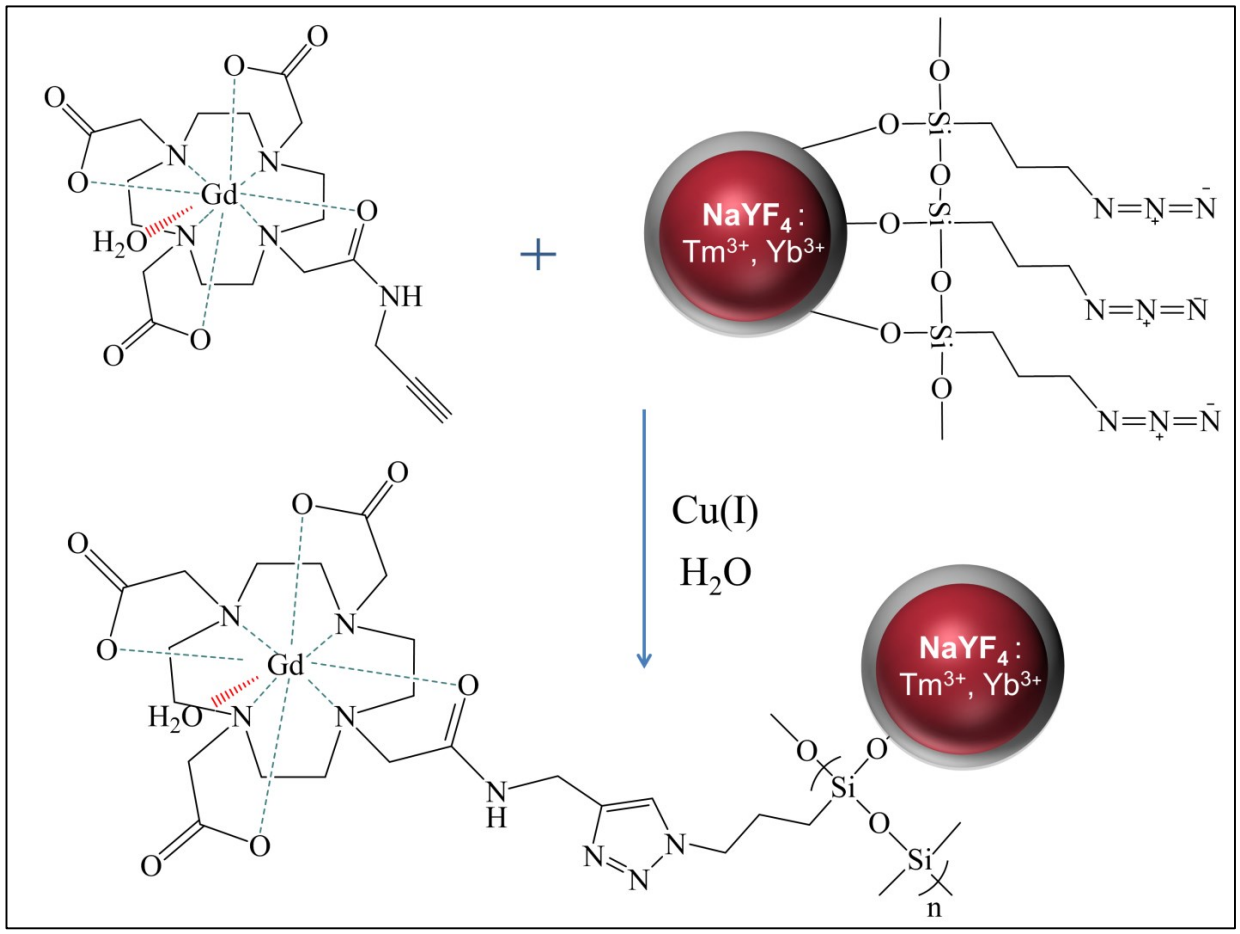

Figure 4.13: The reaction scheme of the conjugation of a MRI contrast agent Gd-DOTA to an azide modified silica coated $NaYF_4$: $Tm^{3+,}$ Yb^{3+} nanoparticles.

Briefly, the reaction of the alkyne and azide moieties was catalyzed by Cu(I) at room temperature. Sodium ascorbate was used to reduce Cu(II) to Cu(I). During the reaction, the color

of the solution was observed to change from light blue to light yellow, which was an indication of the presence of the catalyst Cu(I) (Figure 4.14).

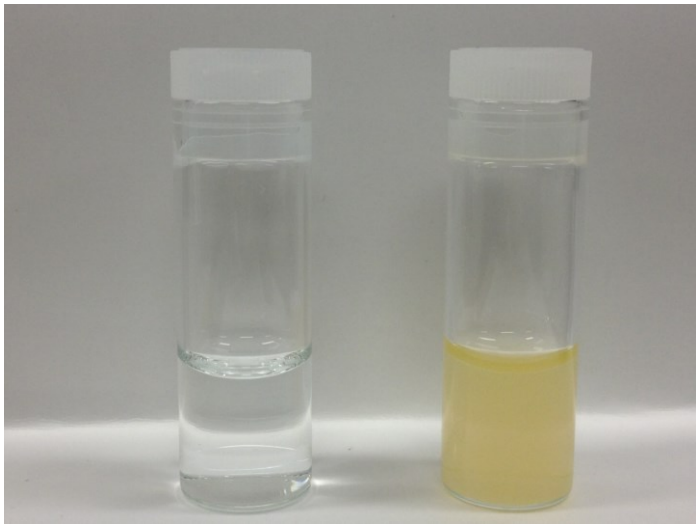

Figure 4.14: Sodium ascorbate reduced Cu(II) to Cu(I) during the click reaction. The color of the solution changed from light blue to light yellow.

To ascertain the presence of the Gd-DOTA complex on the surface of the silica coated UCNPs, FTIR spectroscopy was employed. Figure 4.15a, b, c shows the FTIR spectra of the alkyne terminated Gd-DOTA, of the azide modified silica coated UCNPs and the final product which is UCNPs functionalized with the Gd-DOTA complex respectively. In Figure 4.15a, the following peaks in the FTIR spectrum were observed and the compound was confirmed to be alkyne terminated Gd-DOTA: peak at 3307 cm^{-1} was attributed to N-H stretching of amide; 2993 cm^{-1} (C-H stretching); 2128 cm^{-1} (C≡C stretching); a pair of peaks at 1697 and 1404 cm^{-1} (asymmetric and symmetric stretching of partial C=O of carboxylate); 1625 cm^{-1} (C=O stretching of amide); 1209 cm^{-1} (C-O stretching) and 1132 cm^{-1} (C-N stretching). Figure 4.15b showed the characteristics peaks of the azide modified silica coated UCNPs at 2933, 2108 and

1099 cm $^{-1}$ (the assignments were discussed in the previous section). The FTIR spectrum in Figure 4.15c represents the final product following the click reaction. The characteristics peaks of silica were observed in the spectrum, which were expected: 1091, 957, 805 cm $^{-1}$ (the assignments were discussed in section 4.2.1). Comparing the spectrum (b) the azide modified silica coated UCNPs to the spectrum (c) the product formed following the click reaction in Figure 4.15, the first important difference was the disappearance of the peak at 2108 cm^{-1} (N≡N asymmetric stretching) in Figure 4.15c, indicating the completion of the click reaction. The second important difference was the appearance of the peak at 1648 cm^{-1}, which corresponded to the peak of the highest intensity from Figure 4.15a, which was identified to be the asymmetrical C=O stretching of the carboxylate group for alkyne terminated Gd-DOTA.

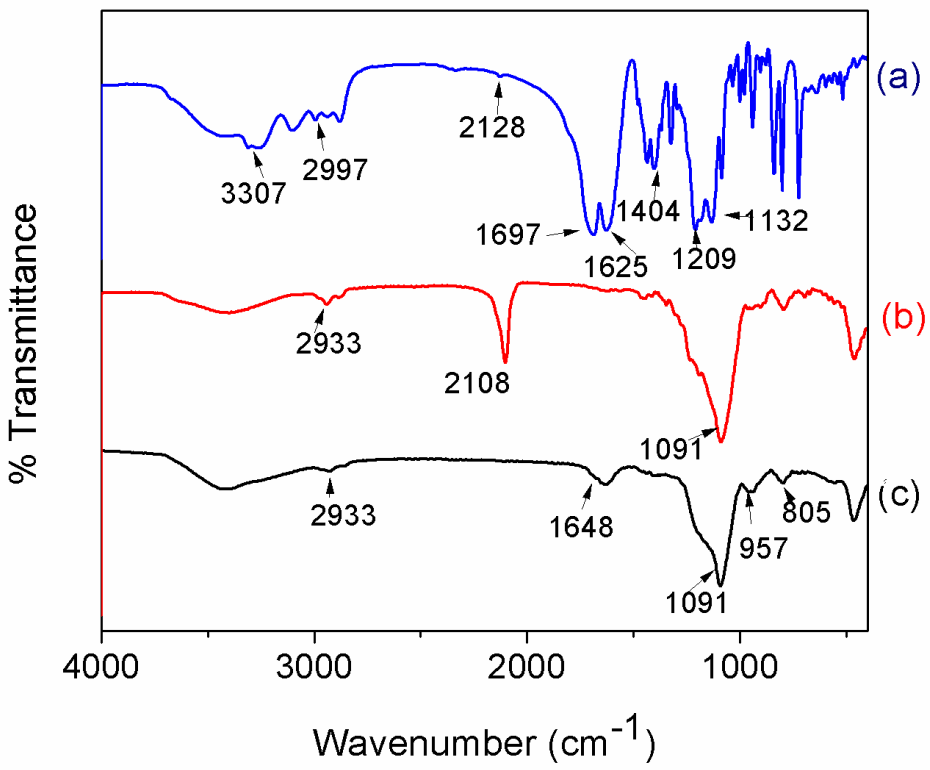

Figure 4.15: FT-IR spectra of (a) alkyne Gd-DOTA; (b) azide modified silica coated upconverting nanoparticles $NaYF_4$: Tm^{3+}, Yb^{3+}; (c) nanoconstruct following the click reaction.

The FTIR results provide evidence for the conjugation of Gd-DOTA onto the surface of the UCNPs using the click reaction. Further evidence for the formation of (Gd-DOTA)-UCNP nanoconstruct may be obtained by comparing the T_1 and T_2 relaxivities of the alkyne Gd-DOTA complex to those obtained for the nanoconstruct since the tumbling rates for the two systems should be different. As a MRI contrast agent, the tumbling rate plays an important role in the enhancement the relaxation rate of water molecules, which is defined by the relaxivity. In order to evaluate the enhancement effect of the two contrast agents, the alkyne Gd-DOTA complex and the (Gd-DOTA)-UCNP, a relaxometry experiment was carried out.

Since the paramagnetic contribution on the relaxation rate is directly proportional to the concentration of the contrast agent, an accurate determination of the Gd^{3+} ion concentration in the two samples was required, which was performed using ICP-MS. The calibration curve for gadolinium in ICP-MS analysis was first established (Figure 4.16) using Gd^{3+} ions as the standard reagents from 0.1 to 1.0 ppm. This method required digestion of the samples in concentrated nitric acid prior ICP-MS analysis. The calibration curve was used to determine the Gd concentration of the alkyne Gd-DOTA complex and the nanoconstruct (Gd-DOTA)-UCNP. The analysis results were obtained in ppm, which were converted to mM since the unit of relaxivity is normally expressed in mM^{-1} s^{-1}.

Time domain NMR was employed to measure the proton relaxation rate of the two samples. The samples were prepared as 100% (stock solution) along with dilutions at 75, 50, and 25 % v/v. The corresponding T_1 and T_2 relaxation rates of the samples were plotted against Gd concentration (Figure 4.17 a, b). The slopes of the linear plots represent the T_1 and T_2 relaxivities, denoted using parameters r_1 and r_2. The results were summarized in Table 4.4. The T_1 and T_2 relaxivities of alkyne Gd-DOTA were found to be 3.4 and 3.9 mM^{-1} s^{-1} respectively.

These values were in accordance to the literature data [36]. However, the T_1 and T_2 relaxivities of the nanoconstruct were found to be 16.9 and 28.2 mM^{-1} s^{-1} respectively, which were significantly higher than the Gd^{3+} chelates (Table 4.4). These results were expected since immobilizing gadolinium complex to nanoparticles of size 27 nm, had effect of significantly reducing the tumbling rate of the system, allowing for more water molecules to be interacted with Gd^{3+} per second [60, 61]. The T_1 relaxivity or longitudinal relaxivity directly refers to the efficiency of a contrast agent in the enhancement of water relaxation rate. The higher the relaxivity suggests the better enhancement effect. These results not only indicated the success of the click reaction, the covalent conjugation of Gd-DOTA to the upconverting nanoparticles, but it also showed the potential benefits of the nanoconstruct for MR imaging.

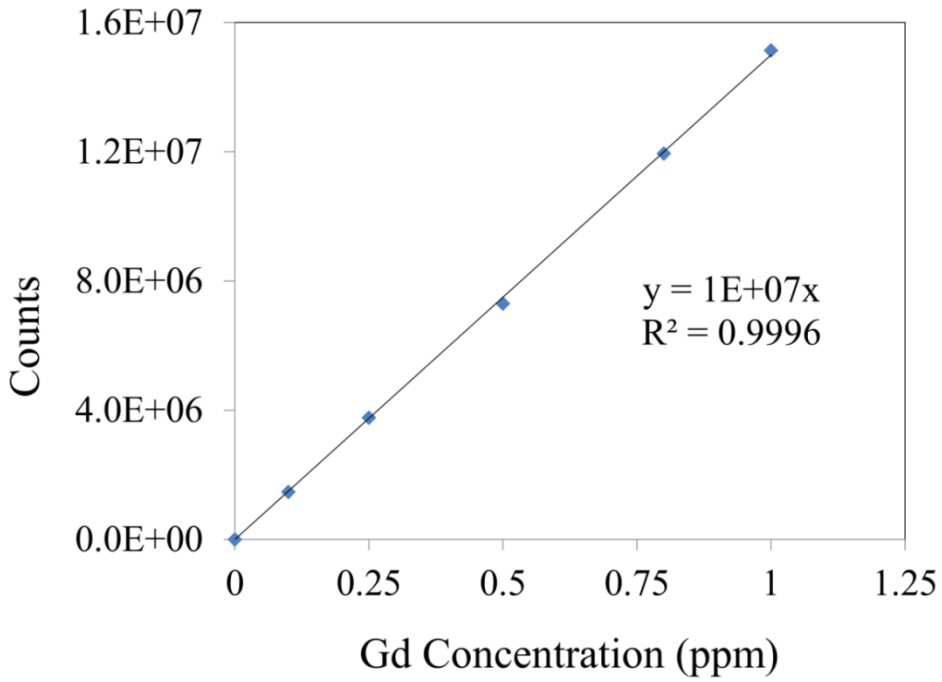

Figure 4.16: Calibration curve for gadolinium in ICP-MS analysis.

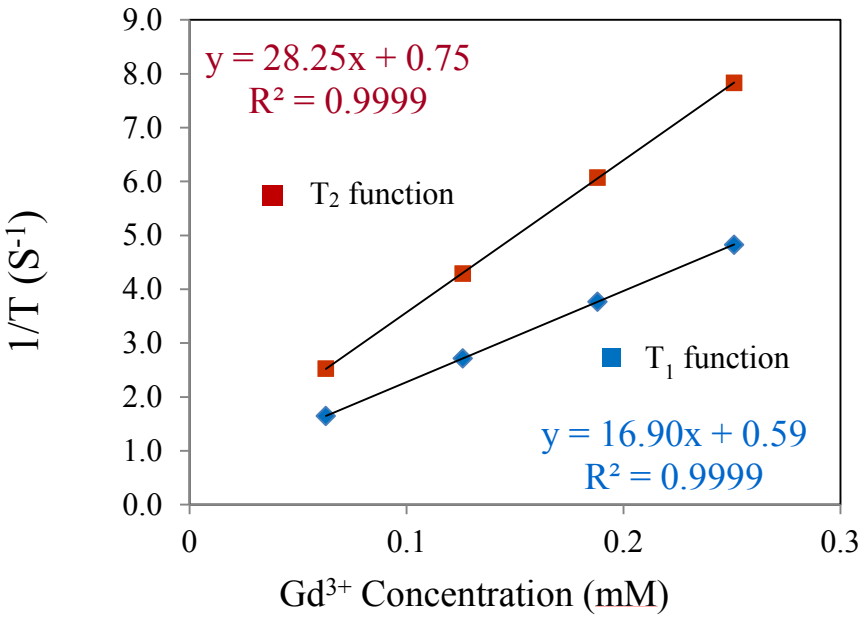

(a)

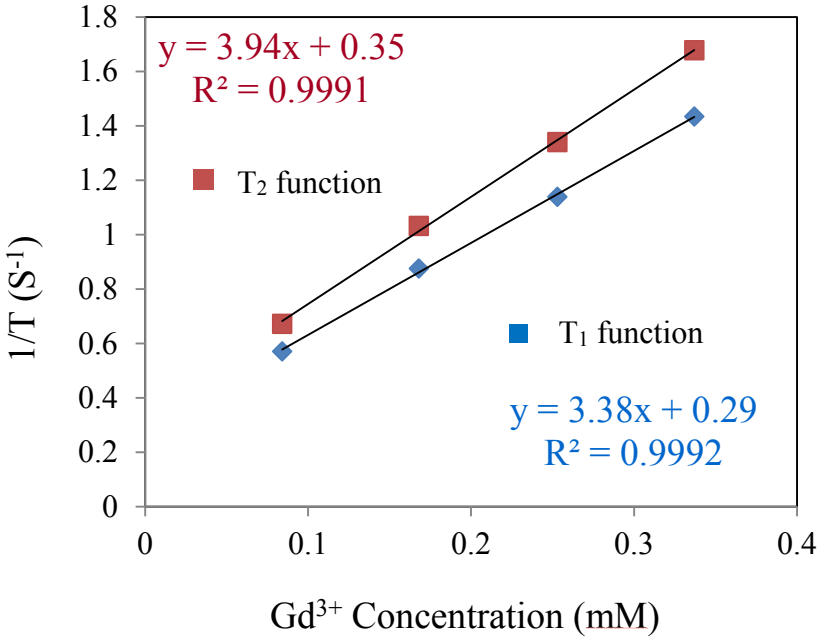

(b)

Figure 4.17: T_1 and T_2 relaxivities plots for (a) nanoconstruct Gd-DOTA-(UCNPs) and (b) alkyne Gd-DOTA.

Table 4.4: T_1 and T_2 relaxivities of alkyne Gd-DOTA and the nanoconstruct in water under physiological conditions (37 ℃ and pH = 7) at 60 MHz

	Alkyne_Gd-DOTA	Nanoconstruct
T_1 relaxivities	3.38	16.90
T_2 relaxivities	3.94	28.25

The optical properties of the nanoconstruct were characterized using luminescence spectroscopy. The nanoconstruct is composed of the core $NaYF_4$: Tm^{3+}, Yb^{3+}, of silica shell and the MRI contrast agents Gd-DOTA conjugated onto the surface. Figure 4.18 shows the upconversion emission spectra of the nanocontruct (Gd-DOTA)-UCNPs, following 980nm excitation. The nanoconstruct clearly showed the characteristic transitions of Tm^{3+}. The blue emission peaks observed at 450 nm and 480 nm were attributed to the $^1D_2 \rightarrow {}^3F_4$ and $^1G_4 \rightarrow {}^3H_6$ transitions respectively. The red emission peak at 650 nm was assigned to the $^1G_4 \rightarrow {}^3F_4$ transition and finally the most intense emission peak at 800 nm was assigned to the $^3H_4 \rightarrow {}^3H_6$ transition.

The upconversion spectrum of the nanoconstruct in Figure 4.18 was normalized to the NIR emission peak at 800 nm from the spectrum of the starting material, oleate capped $NaYF_4$: Tm^{3+}, Yb^{3+} dispersed in toluene, which gave higher upconversion efficiency in nonpolar solvent. The overall luminescence intensity of the nanoconstruct was observed to be weaker compared to the oleate capped UCNPs dispersed in toluene. This is likely due to the high efficiency of the vibrations of water molecules in bridging the energy gaps separating the emitting levels of the thulium(III) ions. The NIR: Blue ratio for the nanoconstruct was calculated to be 6.68 whereas the oleate capped UCNPs has a NIR: Blue ratio of 8.34 (the area of the peak at 800 nm *versus* the area of the peak at 480 nm.) The lower NIR: Blue ratio for the nanoconstruct showed

quenching in the intensity of the NIR at 800 nm, which is likely due to silica phonons in bridging the energy gap of $^3H_4 \rightarrow {}^3H_6$ transition. However, the decrease in intensity of the NIR emission peak is not as significant as expected, which shows the efficiency of NIR-NIR excitation-emission process of the silica coated nanoconstruct in water, and it shows that the nanoconstruct has potential to be used as *in vivo* optical probe.

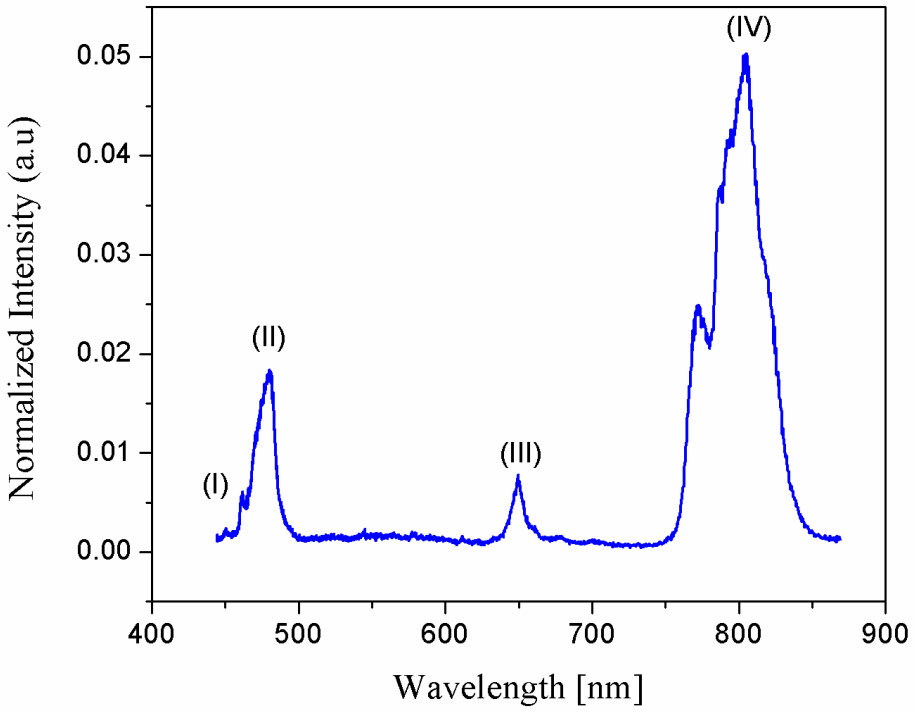

Figure 4.18: Luminescence spectrum of 1 wt% nanoconstruct (Gd-DOTA)-UCNPs dispersed in water, following excitation of 980 nm. The emission spectrum was normalized to the NIR at 800 nm of 1 wt% oleate capped UCNPs $NaYF_4$: Tm^{3+}, Yb^{3+} dispersed in toluene. Upconversion emission was ascribed to the transitions of (I) $^1D_2 \rightarrow {}^3F_4$, (II) $^1G_4 \rightarrow {}^3H_6$, (III) $^1G_4 \rightarrow {}^3F_4$, (IV) $^3H_4 \rightarrow {}^3H_6$.

Finally, we have demonstrated the synthesis of bimodal nanoconstruct, which is the functionalization of Gd chelates onto the UCNPs $NaYF_4$: Tm^{3+}, Yb^{3+} , resulting in higher relaxivities than commercial MRI contrast agents. The nanoconstruct possesses unique optical

property. Its NIR-to-NIR excitation-emission was shown to be effective in water, which renders this system suitable for bioimaging since both excitation and emission fall within the biological window. Meanwhile, we are exploring alternative ways for designing a contrast agent which would offer optical and paramagnetic properties.

4.2.2 Design of a Blood Pool Contrast Agent (Polymer Coating of Ultra-small UCNPs)

Low molecular weight of Gd^{3+} chelates are rather inefficient for imaging of arteries or veins due to rapid diffusion rate and short circulation time in the blood vessels (early distribution phase $t_{1/2} \approx 10$ min; elimination $t_{1/2} \approx 1.5$ hours). Morever, the major problem associated with the low molecular weight contrast agents (CAs) is the rapid tumbling motion resulting in low relaxivity. Therefore, another class of contrast agents, known as blood pool CAs, have been designed to address both the need for longer vascular retention times and the higher relaxivity [62].

Due to their higher molecular weight, blood pool CAs provide longer circulation times resulting in longer image acquisition window, which may be used to increase both the signal-to-noise ratio and to improve image resolution [63]. The previous sections presented the functionalization of Gd^{3+} chelates onto upconverting nanoparticles leading to higher relaxivities. Another approach for designing T_1 CAs would be the incorporation of Gd^{3+} into the nanocrystalline system. The advantages of this approach include simple synthetic procedure which would not involve the tedious functionalization of Gd^{3+} chelates; a higher concentration of Gd^{3+} ions per nanoparticle; control of targeting and clearance making use of the surface chemistry. Capobianco's group reported the relaxivities values and the r_1/r_2 ratio of citrate

capped ultra-small $NaGdF_4$: Tm^{3+}, Yb^{3+} (<5 nm diam.,) which was found to be very similar to commercial Gd^{3+} chelates and provided efficient positive contrast for MRI. However, the results of biodistribution of citrate capped US-UCNPs showed a strong uptake of nanoparticles by the liver after 48h and after 8 days [9]. In general, when nanoparticles are administered into the blood, they are taken up by the phagocytic cells of the mononuclear phagocyte system (MPS) [64]. The retention time and the clearance rate of nanoparticles depend on many factors; however, size and surface chemistry play a predominant role. For example, positively charged nanoparticles are taken up at a faster rate in comparison to neutral or negatively charged nanoparticles [65]. It has been suggested that the rate of clearance rate can be reduced by adding poly(ethylene) glycol (PEG) to the surface of nanoparticles. In addition, PEG prevents antibody opsonisation, and drastically increases the blood half-life of nanoparticles [66]. It has also been shown that nanoparticles with diameters smaller than 6 nm may be eliminated by the kidneys [67]. Without such clearance route, the biodegradation of nanoparticles could potentially lead to toxic components. Therefore, a new class of blood pool CAs was designed using ultra-small $NaGdF_4$: Tm^{3+}, Yb^{3+} as base material, which are to be functionalized with PEG polymer. The aim was to prolong the circulation time in the blood vessels and to control clearance *via* renal route.

The design of a blood pool CAs for MRI involved first the synthesis of ultra-small $NaGdF_4$: Tm^{3+}, Yb^{3+} (US-UCNPs) (section 4.1.2) followed by coating the surface of the nanoparticles using PEG diacid. We selected PEG of relatively low molecular weight (Mn = 600) and with two carboxylate groups, which functioned as anchor groups to bind the positively charged surface of the US-UCNPs. Oleate was the capping ligand of the starting material, which also has one carboxylate group that binds to the positively charged surface of US-UCNPs.

Therefore, the two ligands compete to bind to the surface of UCNPs. In order to displace all oleates, theoretically, PEG polymer has to be provided in higher concentration compared to the oleates. Then, the high PEG concentration pushes the position of the equilibrium to the right according to Le Chatelier's Principle. It was observed that the ligand exchange process was efficient at pH 3-4, at 40 ℃. The DLS results shown in Figure 4.19a,b were the nanoparticles obtained after ligand exchange reaction, dispersed in aqueous solution. The concentration of PEG diacid at 0.02 M resulted in US-UCNPs of hydrodynamic diameter of 436 nm whereas a relatively higher PEG diacid concentration of 0.2 M gave nanoparticles in smaller hydrodynamic diameter of 55 nm. It is evident that 0.02 M of PEG diacid was not sufficient to displace all oleate on the surface of US-UCNPs, which caused the nanoparticles to agglomerate in aqueous solution. When PEG diacid was present at higher concentration, 0.2 M during the ligand exchange process, more oleate on the surface of US-UCNPs were being replaced, this has resulted in colloidally more stable nanoparticles, indicated by smaller hydrodynamic diameter.

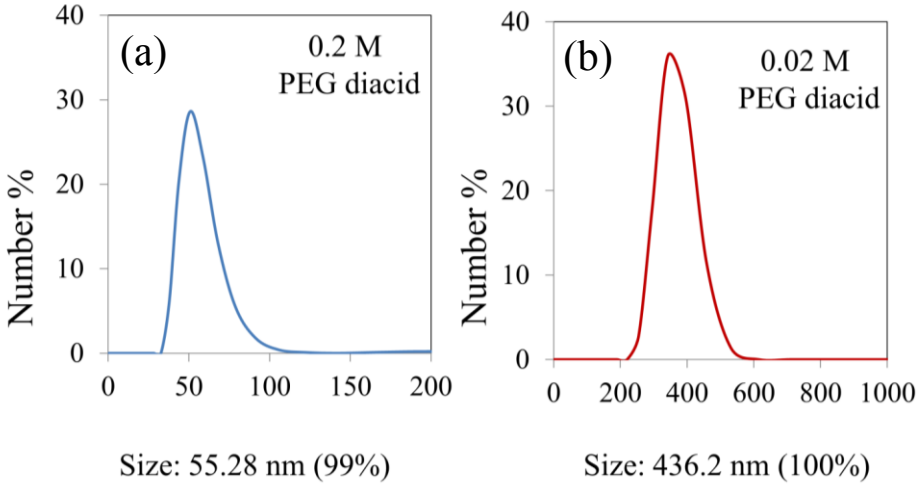

Figure 4.19: Hydrodynamic diameter of PEG grafted US-UCNPs using (a) 0.2 M of PEG diacid; (b) 0.02 M of PEG diacid determined by DLS. Both sets of nanoparticles were dispersed in 154 mM NaCl solution, pH 5.

Polymer coating of US-UCNPs rendered the nanoparticles water dispersible. To be used as a blood pool agent, the PEG coated-UCNPs must be stable in the commonly used saline solution (154 mM NaCl). Dynamic light scattering (DLS) was used to evaluate the colloidal stability of the PEG coated US-UCNPs over a period of one month. The hydrodynamic diameters of the PEG coated US-UCNPs dispersed in the saline solution after the dialysis (day 1), day 7, and day 30 was observed to be 51 nm, 51 nm and 59 nm. Therefore, it is concluded that the hydrodynamic diameters of the PEG coated US-UCNPs dispersed in the saline solution did not change after 7 days demonstrating that the nanoparticles are stable and that no agglomeration occurred (Figure 4.20).

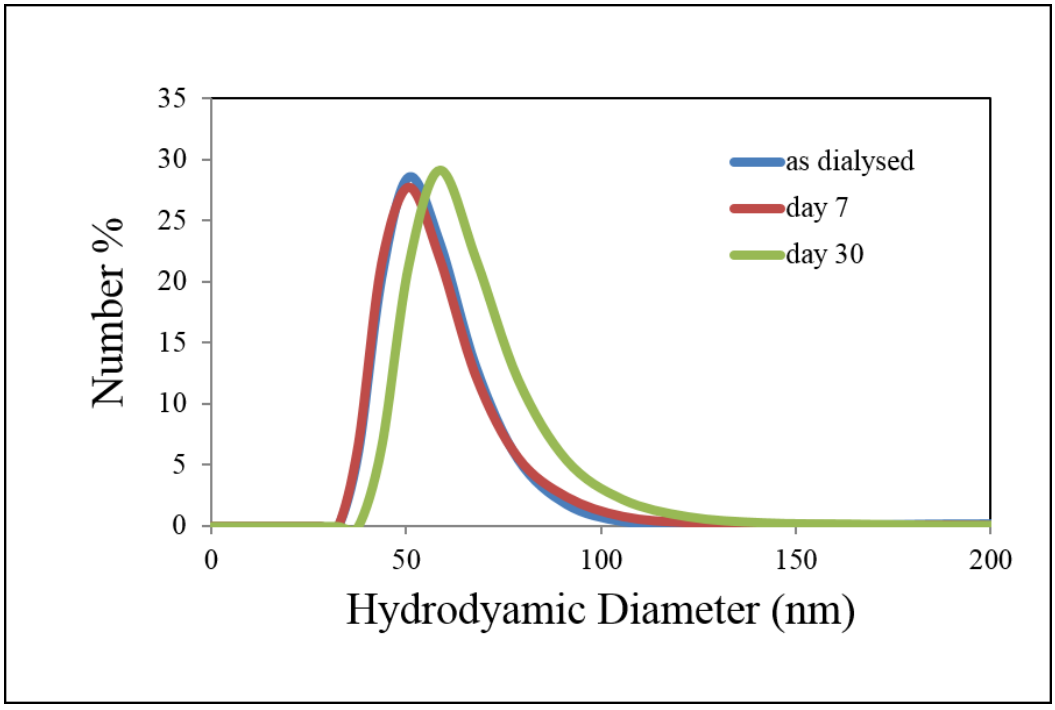

Figure 4.20: Colloidal stability evaluation of PEG coated US-UCNPs dispersed in 154 mM saline solution as function of time (pH 5), by DLS.

Figure 4.21a,b show the TEM images of oleate capped US-UCNPs and PEG coated US-UCNPs respectively. It is evident from the TEM images (Figure 4.21a) that the oleate capped US-UCNPs show no agglomeration. The oleate capped US-UCNPs appeared to be distant from each other in a homogeneous fashion, which is due to interdigitation of the hydrocarbon chains from the oleate. In Figure 4.21b, the PEG coated US-UCNPs formed small clusters, and the nanoparticles self-assembled *via* an attractive interaction. Since PEG diacid has a carboxylic acid group at each end of the polymer chain, it is speculated that certain carboxylic acid groups were not chelated by the lanthanides ions of the US-UCNPs and were exposed on the outer surface of the nanoparticles leading to hydrogen bonding with other PEG coated nanoparticle. This could possibly explain why the US-UCNPs were closely bound to each other as shown in Figure 4.21b.

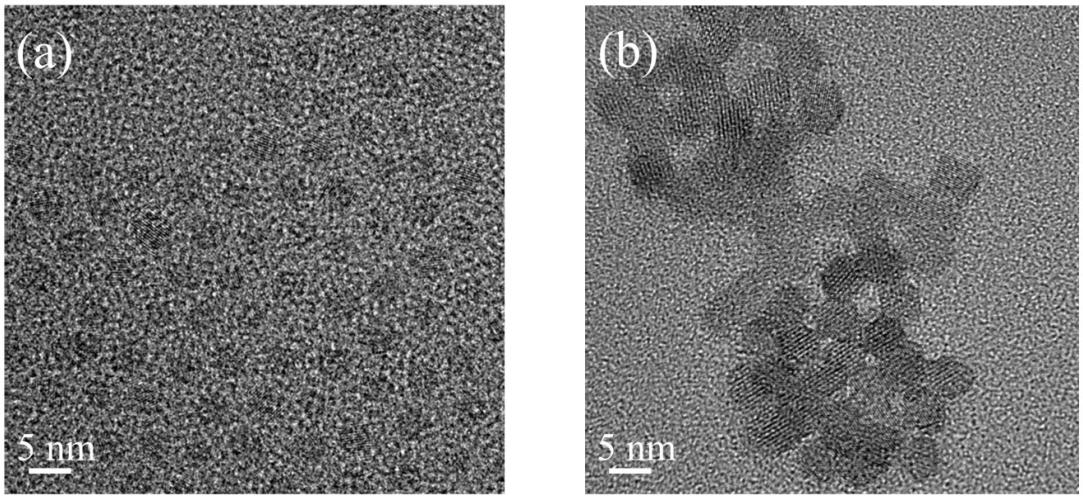

Figure 4.21: TEM images of (a) Oleate capped US-$NaGdF_4$: Tm^{3+}, Yb^{3+} ; (b) PEG coated US-$NaGdF_4$: Tm^{3+}, Yb^{3+} (The nanoparticles were dispersed in aqueous solution of pH 5, 154 mM of saline).

Following the ligand exchange reaction and dialysis, the solution where the PEG coated US-UCNPs were dispersed was found to be at pH 5. The pH was adjusted for the zeta potential measurement. Table 4.5 showed the zeta potential of PEG coating of US-UCNPs in solutions at different pH. Zeta potential is usually employed as indication of the degree of stabilization of a colloidal system. Large zeta potential of $\pm$ 25 mV usually indicates a stable colloidal system that nanoparticles resist aggregation [68]. PEG coated US-UCNPs gave a relatively low zeta potential value of – 4.95 mV at pH 5 in 154 mM of saline solution. However, both DLS and TEM results which were measured at the same conditions suggested that these nanoparticles were stable since no severe aggregation was observed (Figure 4.19a and 4.21b). In fact, colloidal stability is imparted by the combination of electrostatic and steric effects. Generally, polymers provide stability to colloids through steric stabilization [69, 70]. Therefore, the colloidal stability of PEG coated US-UCNPs was due to steric repulsion of the polymers on the surface of the nanoparticles. This explains why PEG coated US-UCNPs did not aggregate despite the low zeta potential. PEG coating of nanoparticles provided good colloidal stability and low surface charge, which could result in interesting biological effects. It was discussed that surface charge played an important role in the rate of nanoparticles uptake by the phagocytic cells of the mononuclear phagocyte system (MPS). Nanoparticles with close to zero surface charge are expected to give longer retention time in blood circulation which could be advantageous in bioimaging.

Table 4.5: Zeta potential of PEG coated US- $NaGdF_4$: Tm^{3+}, Yb^{3+} in deionized water.

pH of the solution	Zeta Potential (mV)
3	- 0.52
5	- 4.95
7	- 8.89

US-UCNPs and the PEG diacid respectively. The oleate capping ligand was characterized in spectrum (b): the peak at 3010 cm $^{-1}$ corresponded to the sp^2 C-H stretch; the peaks observed at 2923, 2856 cm $^{-1}$ corresponded to the sp^3 C-H stretch; the asymmetrical and symmetrical partial C=O bond stretch of carboxylate groups were found at 1562, 1467 cm $^{-1}$. The PEG diacid solution (pH = 3) which was to be used for the ligand exchange reaction was characterized in spectrum (c): the peak at 2870 cm $^{-1}$ corresponded to the sp^3 C-H stretch, the peak at 1756 cm $^{-1}$ corresponded to the C=O stretch of the carboxylic acid and the peak at 1115 cm $^{-1}$ corresponded to the C-O stretch. Following the ligand exchange reaction, the products showed the characteristics peaks of PEG diacid on spectrum (a): 2866 cm $^{-1}$ which corresponded to the sp^3 C-H stretch, 1751 cm $^{-1}$ corresponded to the C=O stretch. The peak at 1097 cm $^{-1}$ which corresponded to the C-O stretch. The pair of peaks found at 1616 and 1469 cm $^{-1}$ which was present in the spectrum of PEG diacid, corresponded to the asymmetrical and symmetrical stretches of the carboxylate. Therefore, we confirmed the success of the ligand exchange reaction and that the US-UCNPs were coated by PEG diacid.

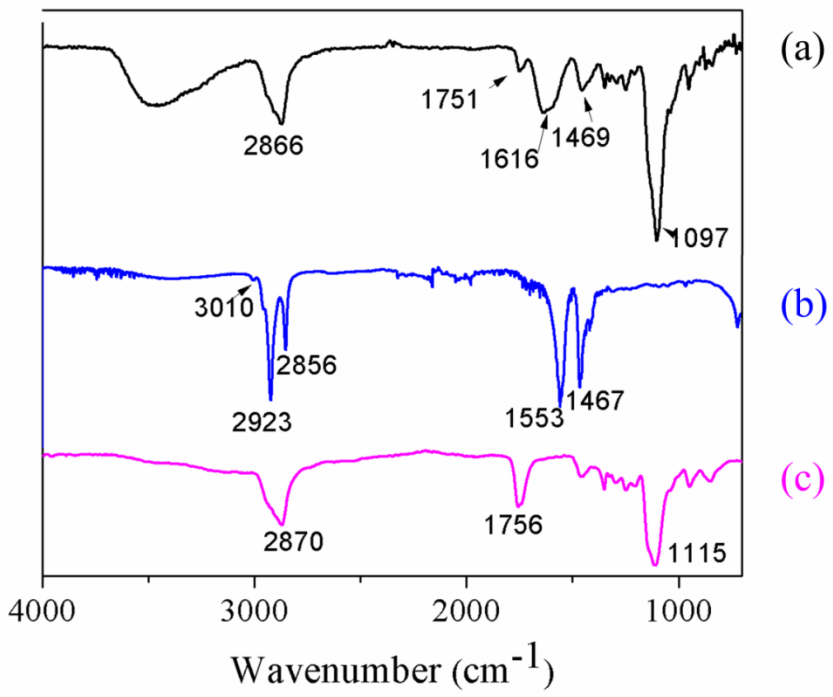

Figure 4.22: FTIR spectra (a) PEG capped US- $NaGdF_4$: Tm^{3+}, Yb^{3+} ; (b) oleate capped US-$NaGdF_4$: Tm^{3+}, Yb^{3+} ; (c) PEG diacid pH = 3.

X-ray photoelectron spectroscopy (XPS) was employed to confirm the presence of PEG on the surface of US-UCNPs. Figure 4.23 shows magnified regions of the XPS spectrum for PEG coated US- $NaGdF_4$: Tm^{3+}, Yb^{3+}. From the XPS data, the ratio of carbon / oxygen was calculated to be 2:1 which is consistent to stoichiometric ratio of carbon / oxygen of the PEG diacid showing below.

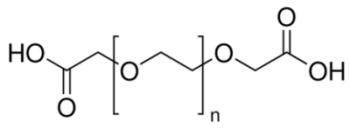

PEG diacid Mn = 600

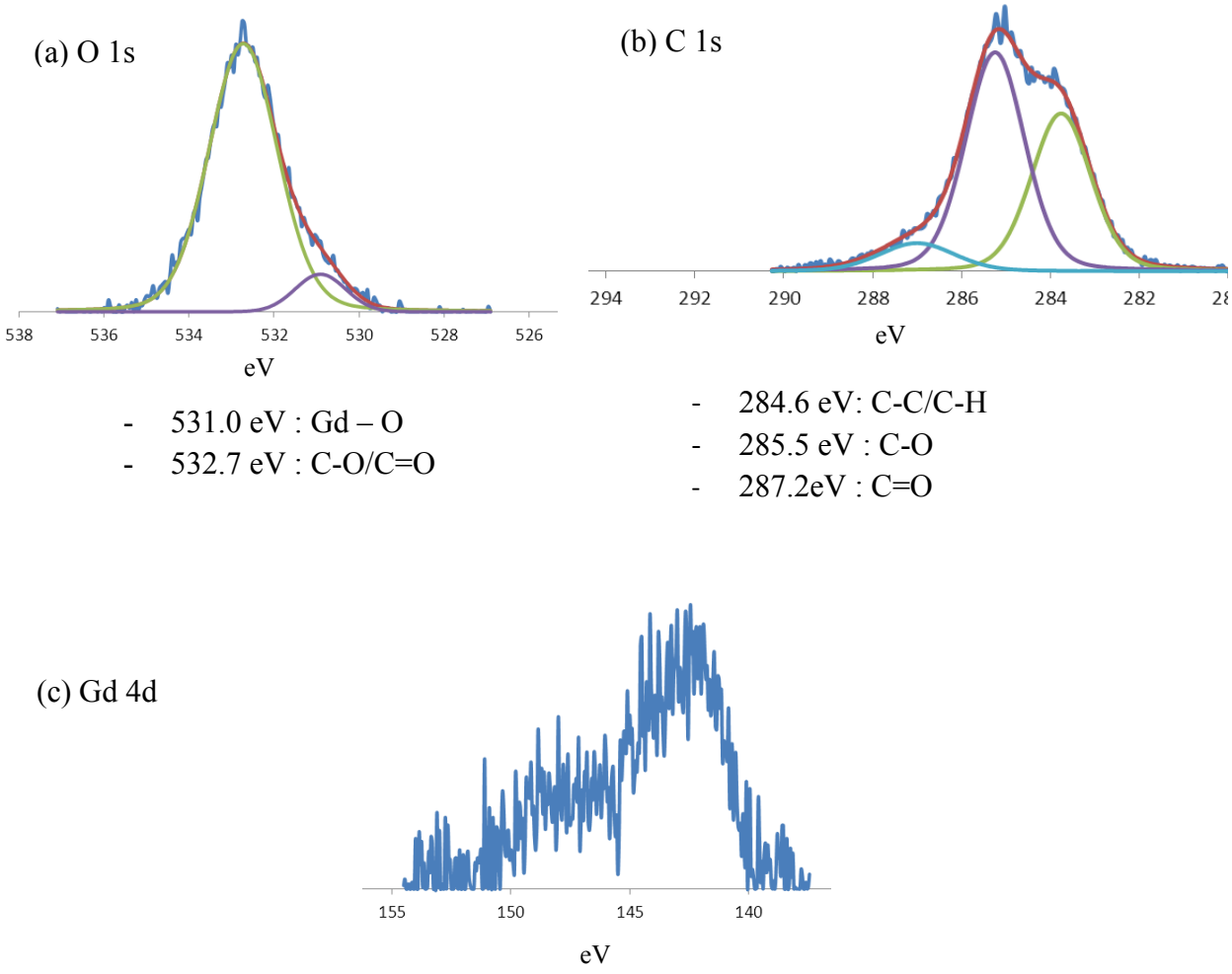

Figure 4.23: XPS spectrum for PEG coated US- $NaGdF_4$: Tm^{3+}, Yb^{3+} magnified region (a) 538 – 526 eV for oxygen (1S); (b) 294 –280 eV for carbon (1S); (c) 155 – 140 eV for gadolinium (4d).

Both FTIR and XPS results confirmed the capping ligand on the US-UCNPs to be PEG acid. It is important to study the effect of the capping ligand on the relaxivity of US-UCNPs. Therefore, a relaxometric experiment was performed by comparing lysine coated US-UCNPs and PEG coated US-UCNPs. The structures of both ligands are shown below. Lysine, an amino

acid with molecular weight of 146 g/mol, has one carboxylic acid and two amine groups. PEG diacid, a polymer has average molecular weight of 600 g/mol. The characterization on lysine coated nanoparticles is shown in Appendix B.

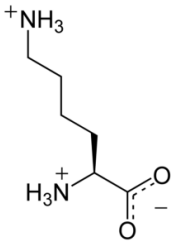

Lysine

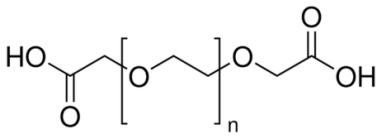

PEG diacid Mn = 600

Both lysine and PEG coated US-UCNPs dispersed in water were prepared in a diluted series of 100 % (the dialyzed dispersion), 75%, 50 % and 25% v/v prior relaxometric measurement. The Gd concentration of each set of the samples was determined using neutron activations since it has been shown that the ICP-MS/ICP-AES techniques which involve the digestion procedures of the sample using concentrated nitric acid caused an underestimate the concentration of lanthanide ions in the sample [71]. The proton relaxation rate of each set of the samples was measured using time domain NMR. Figure 4.24a,b shows the plots of proton relaxation rate vs. Gd concentration for PEG coated and lysine coated US-UCNPs respectively. The T_1 and T_2 relaxivities were determined as the value of the slopes from the linear plots, denoted r_1 and r_2 respectively. The relaxometric results were summarized in table 4.6.

The T_1 and T_2 relaxivities of lysine grafted US-UCNPs were found to be 3.61 and 5.24 respectively. These values were very close to the citrated capped US- $NaGdF_4$: Tm^{3+}, Yb^3 reported by Naccache R. *et al*. (r_1=3.37, r_2=3.96, r_2 / r_1 =1.18) [9]. In contrast, PEG coated US-UCNPs gave slightly higher T_1 and T_2 relaxivities, 5.79 and 7.41 respectively. These results were expected since both lysine and citrate have lower molecular weight compared to PEG. Coating

PEG polymer on the surface of US-UCNPs has the effect of slowing down the tumbling rate, thus resulting in higher relaxivities. Moreover, since a MR contrast agents affect both T_1 and T_2 relaxation rate simultaneously, the ratio between the T_2 and T_1 relaxivities (expressed as r_2/r_1), is commonly used to assess the efficiency of a MR contrast agent. The ratio r_2/r_1 provides an indication as to whether the contrast agent can be employed as a positive or negative CA. An efficient T_1 contrast agent must have a large paramagnetic property with negligible magnetic anisotropy. Typically, T_1 contrast agents have r_2/r_1 ratio approaching 1 whereas commercial iron oxide nanoparticles used in T_2-weighted MRI imaging has a r_2/r_1 ratio between 6-15 [72]. The ratio r_2/r_1 of PEG and lysine grafted US- $NaGdF_4$: Tm^{3+}, Yb^{3+} were calculated to be 1.28 and 1.45 respectively, thus both may be considered as potential T_1 contrast agent.

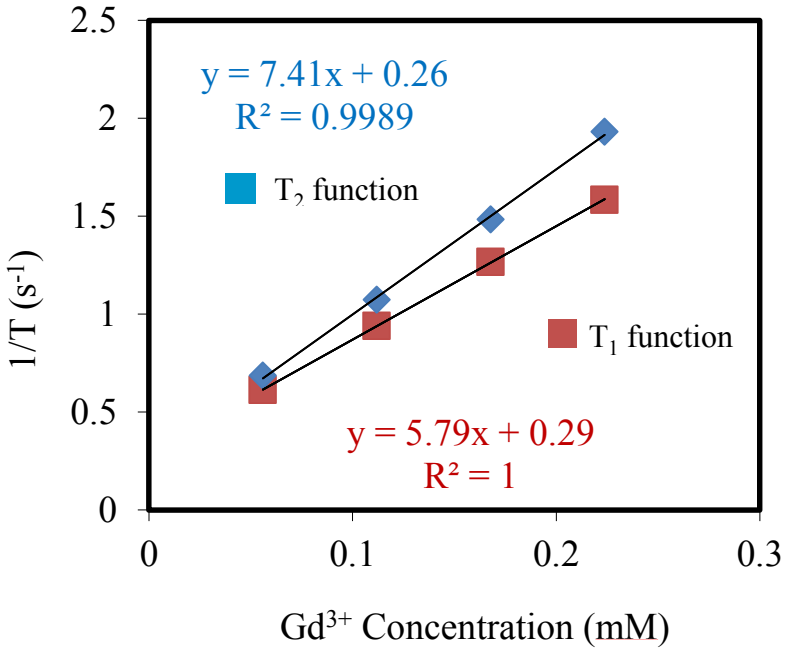

(a)

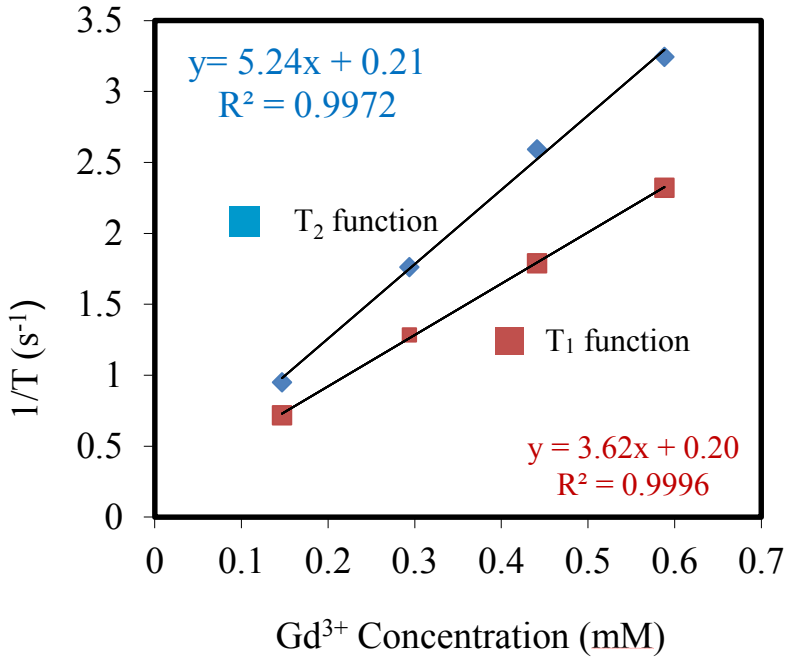

(b)

Figure 4.24: T_1 and T_2 relaxivities plots for (a) PEG coated US- $NaGdF_4$: Tm^{3+}, Yb^{3+}; (b) lysine coated US- $NaGdF_4$: Tm^{3+}, Yb^{3+}.

Table 4.6: Relaxometric results of US- $NaGdF_4$: Tm^{3+}, Yb^{3+} coated by different ligands.

Ligands grafted on US-NaGdF4: Tm/Yb	**r_1 ($mM^{-1}s^{-1}$)@ 37 °C, 60MHz**	**r_2 ($mM^{-1}s^{-1}$)@ 37 °C,60MHz**	**r_2 / r_1**
PEG	5.79	7.41	1.28
Lysine	3.61	5.24	1.45

The T_1 and T_2 contrast enhancement abilities were evaluated with *in vitro* MRI. The lysine and PEG coated US-UCNPs were prepared in a set a diluted samples 100% (dialyzed dispersion), 75%, 50% and 25% v/v, which had been previously measured by time domain NMR, were to be analyzed in a MR Scanner of 1 Tesla. Figure 4.25a,b shows the T_1 and T_2 weighted images of the lysine coated US-UCNPs, the PEG coated US-UCNPs and a water sample (a negative control). In the T_1 weighted image (Figure 4.25a), all the spots containing lysine and PEG coated US-UCNPs appeared to be brighter than the control, indicating the positive contrast enhancement by the US-$NaGdF_4$: Tm^{3+}, Yb^{3+}. The contrast decreased with decreasing concentration of Gd. On the other hand, in the T_2- weighted image (Figure 4.25b), all the spots containing lysine and PEG coated US-UCNPs were not showing darker compared to the control, indicating there was not significant T2 effect contributed by the ultra-small sized UCNPs. Therefore, the low r_2/r_1 ratio and the *in vitro* MRI scans demonstrated the efficiency of US-$NaGdF_4$: Tm^{3+}, Yb^{3+} to be used a positive contrast agent.

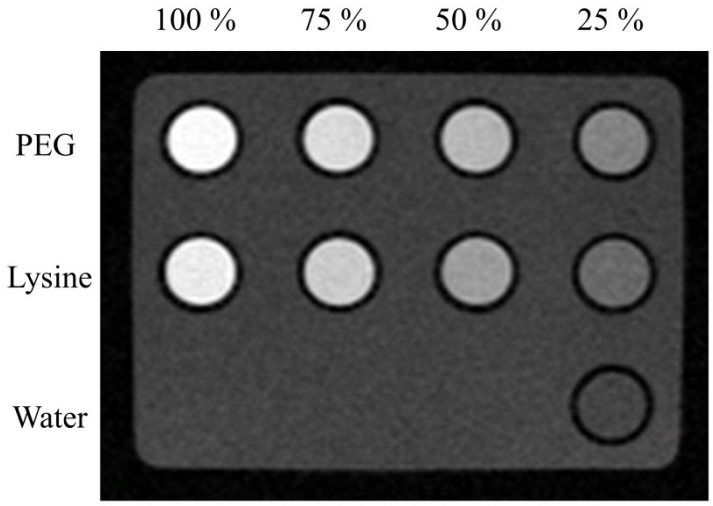

(a)

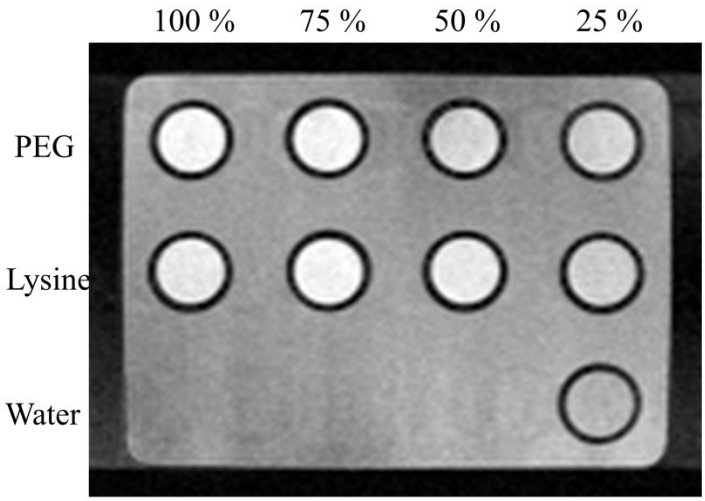

(b)

Figure 4.25: 2-D spin echo images of US- $NaGdF_4$: Tm^{3+}, Yb^{3+} coated with PEG and lysine (a) T_1 weighted image (b) T_2 weighted image. Dilution series identified as 100, 75, 50, 25 % v/v.

Chapter Five – Conclusions

MRI and optical imaging, the two medical imaging techniques are known to provide distinct advantages in disease diagnostics. Upconverting nanoparticles have allowed for the design of a magnetic optical hybrid imaging probe, combining high spacial resolution and high sensitivity, which could result in images revealing more accurate anatomical information than using the two techniques separately. The bimodal contrast agents were designed using two different approaches and may have potential application in biological systems.

The first approach involved the functionalization of a MRI contrast agent, Gd-DOTA onto the surface of upconverting nanoparticles $NaYF_4$: Tm^{3+}, Yb^{3+} using the click reaction. The upconverting nanoparticles $NaYF_4$: Tm^{3+} (0.5 mol%), Yb^{3+} (25 mol%) were synthesized using the thermal decomposition procedure. The synthetic conditions were optimized to yield monodisperse nanoparticles of size 19.4 $\pm$ 2.0 nm. The surface of UCNPs was modified by silica coating, which resulted in larger particle size (27.6 $\pm$ 3.1 nm), and in water dispersible nanoparticles with facile modification of the surface. A multi-step organic procedure was followed to synthesize the alkyne_Gd-DOTA, which was conjugated to the azide modified silica coated UCNPs using the click reaction. Luminescence spectroscopy measurements of the nanoconstruct showed an intense emission of Tm^{3+} ions at 800 nm, an ideal wavelength for bioimaging, upon excitation at 980 nm. The T_1 and T_2 relaxivities of the nanoconstruct were determined to be 16.9 and 28.2 mM^{-1} s^{-1} respectively, which were significantly higher than commercially available Gd^{3+} chelates. These results clearly demonstrate the success of integrating bi-functionalities to nanoscale materials as a novel contrast agents and optical probe.

The second approach involved the design of a bimodal contrast agent to be used as blood pool agent. Ultra-small $NaGdF_4$: Tm^{3+}, Yb^{3+} of size 5.1 ± 0.5 nm were synthesized. Polymer coating using PEG diacid (Mn=600) rendered the hydrophobic nanoparticles water dispersible. The PEG capping ligand was confirmed by FTIR and XPS studies. More importantly, the polymer coated US-UCNPs showed T_1 and T_2 relaxivities of 5.79 and 7.41 mM^{-1} s^{-1} respectively, which were relatively higher than citrate and lysine capped US-UCNPs. Additionally, PEG coated US-UCNPs gave a low zeta potential value of – 4.95 mV at pH 5, which would be suitable for *in vivo* imaging [74]. These nanoparticles provided very good colloidal stability in saline solution. Finally, *in vitro* MRI evaluation showed that the PEG capped ultra-small $NaGdF_4$: Tm^{3+}, Yb^{3+} can be used as an efficient T_1 contrast agent.

Chapter Six – Future Works

The nanoconstruct Gd-DOTA-$NaYF_4$: Tm^{3+}, Yb^{3+} were monodisperse, water dispersible, possessed unique optical property and showed high T_1 relaxivity as described in the Section 4.2. For biological applications, the as-synthesized nanoconstruct must also meet the following requirement, the colloidal stability in biological conditions. Preliminary results indicated that the as-synthesized Gd-DOTA-UCNPs agglomerated in clinical saline solution. Therefore, it is necessary to carry out further surface modification in order to enhance the colloidal system, which may be achieved since the silica shell affords itself to a number of reactions for further conjugation with a number of molecules. Since polymer coated nanoparticles was demonstrated to provide low surface charge and good colloidal stability in clinical saline, PEG polymer chain could be added as a linker between the upconverting nanoparticles and MRI constrast agent Gd-DOTA. The length of the PEG polymer will need be optimized to obtain monodisperse nanoparticles. Figure 6.1 shows the reaction scheme of surface functionalization of Gd-DOTA-NHS-ester on the surface of polymer-silica coated UCNPs $NaYF_4$: Tm^{3+}, Yb^{3+}. Amine-PEG silane could be simply added to the surface of silica coated nanoparticles through silane condensation. The PEG functionalized silica UCNPs will have amine groups on the surface, which will allow for the crosslinking reaction with NHS-ester of the Gd complex. This novel nanoconstruct is expected to provide good colloidal stability and bimodal imaging capabilities.

With respect to the PEG coated US-NaGdF4: Tm^{3+}, Yb^{3+}, it would be interesting to carry our further studies to evaluate its abilities in providing optical and MR imaging in small animals, as well as toxicity and biodistribution.

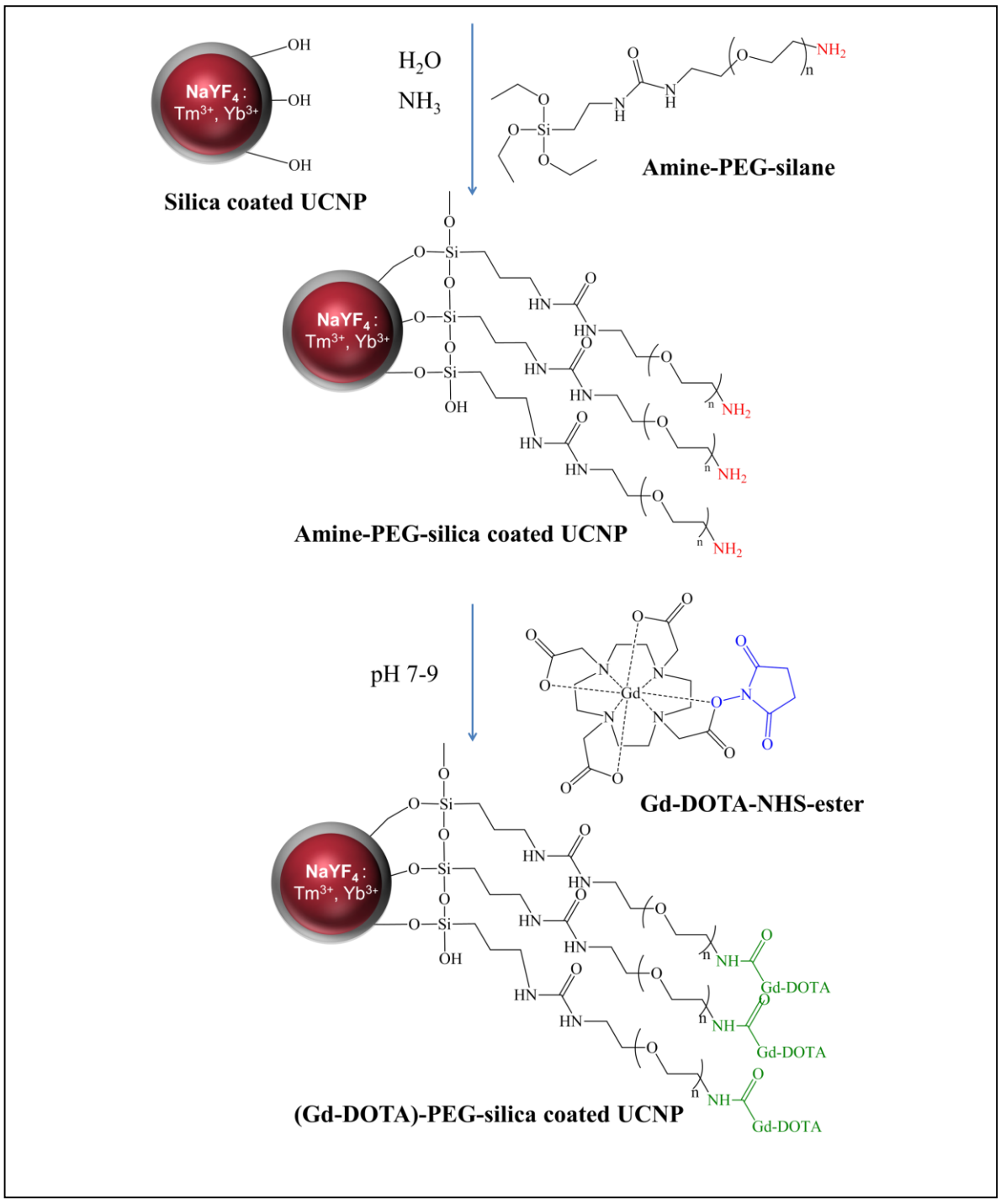

Figure 6.1: Reaction scheme of surface functionalization of (Gd-DOTA)-PEG polymer on the surface of silica coated UCNPs $NaYF_4$: Tm^{3+}, Yb^{3+}.

References:

1) Cademartiri, L.; Ozin G. A. *Concepts of Nanochemistry*; WILEY-VCH: Weinheim, 2009.

2) Daniel, M.C.; Astruc, D. Gold nanoparticles: Assembly, Supramolecular Chemistry, Quantum-size-related Properties, and Applications toward Biology, Catalysis, and Nanotechnology. *Chem. Rev*. **2004**, *104*, 293-346.

3) Meng, H.; Xue, M.; Xia, T.; Ji, Z. X.; Tarn, D. Y.; Nel, A. E. Use of Size and a Copolymer Design Feature to Improve the Biodistribution and the Enhanced Permeability and Retention Effect of Doxorubicin-Loaded Mesoporous Silica Nanoparticles in a Murine Xenograft Tumor Model. *ACS Nano*. **2011**, *5*, 4131-44.

4) Talekar, M.; Kendall, J.; Denny, W.; Garg S. Targeting of Nanoparticles in Cancer: Drug Delivery and Diagnostics. *Anticancer Drugs*. **2011**, *22*, 949-62.

5) Cao, Y. C. Synthesis of Square Gadolium Oxide Nanoplates. *J. Am. Chem. Soc*. **2004**, *126*, 7456.

6) Kompe, K.; Borchert, H.; Storz, J.; Lobo, A.; Adam, S.; Moller, T.; Haase, M. Green-Emitting $CePO_4$:Tb/$LaPO_4$ Core–Shell Nanoparticles with 70 % Photoluminescence Quantum Yield. *Angew. Chem. Int. Ed.* **2003**, *44*, 5513-5516.

7) Boyer, J. C.; Cuccia, L. A.; Capobianco, J. A. Synthesis of Colloidal Upconverting $NaYF_4$: Er^{3+}, Yb^{3+} and Tm^{3+}/Yb^{3+} Monodisperse Nanocrystals, *Nano Lett.* **2007**, *7*, 847-852.

8) Vetrone, F.; Naccache, R.; Juarranz de la Fuente, A.; Blazquez-Castro A.; Martin Rodriguez E.; Garcia Sole J.; Capobianco, J. A. Intramolecular Imaging of HeLa Cells by Non-functionalized NaYF4: Er^{3+}, Yb^{3+} Upcpnverting Nanoparticles. *Nanoscale*. **2010**, *2*, 495-498.

9) Naccache, R.; Chevalier, P.; Lagueux , J.; Gossuin, Y.; Laurent, S.; Elst Vander, C.; Chillian, C.; Capobianco, J. A.; Fortin, M.-A. High Relaxivities and Strong Vascular Signal Enhancement for $NaGdF_4$ Nanoparticles Designed for Dual MR/Optical Imaging. *Adv. Healthcare Mater.* **2013**, 1478-88.

10) Zijlmans, H. J. M. A. A.; Bonnet, J.; Burton, J.; Kardos, K.; Vail, Niedbala R. S.; Tanke, H. J. Detection of Cell and Tissue Surface Antigens Using Up-Converting Phsphors: A New Reporter Technology. *Anal. Biochem*. **1999**, *267*, 30–36.

11) Bottrill, M.; Green, M. Some Aspects of Quantum Dot Toxicity. *Chem. Commun.* **2011**, *47*, 7039–7050.

12) Cheng, L.; Yang, K.; Zhang, S.; Shao, M.; Lee, S.; Liu, Z. Highly-sensitive Multiplexed *in vivo* Imaging Using PEGylated Upconversion Nanoparticles. *Nano Res*. **2010**, *3*, 722-732.

13) Tyrrell, R.M.; Keyse, S.M. New Trends in Photobiology the Interaction of UVA Radiation with Cultured Cells. *J. Photochem. Photobiol. B Biol.* **1990**, *4*, 349–361.

14) Xu, C.; Zipfel, W.; Shear, J.B.; Williams, R.M.; Webb, W.W. Multiphoton Fluorescence Excitation: New Spectral Windows for Biological Nonlinear Microscopy. *Proc. Natl. Acad. Sci. USA*. **1996**, *93*, 10763–10768.

15) Chatterjee, D. K; Rufaihah , A.J.; Zhang, Y. Upconversion Fluorescence Imaging of Cells and Small Animals Using Lanthanide Doped Nanocrystals. *Biometerials*. **2008**, *29*, 937-943.

16) Nyk, M.; Kumar, R.; Ohulchanskyy, T. Y.; Bergey, E. J.; Prasad, P. N. High Contrast *in Vitro* and *in Vivo* Photoluminescence Bioimaging Using Near Infrarer to Near Infrared Up-Conversion in Tm^{3+} and Yb^{3+} Doped Fluoride Nanophsophors. *Nano Lett*. **2008**, *8*, 3834-3838.

17) Raymond, K. N.; Pierre, V. C. Next Generation, High Relaxivity Gadolinium MRI agents. *Bioconjugate Chem*. **2005**, *16*, 3–8.

18) Ahren M. *et al*. Synthesis and Characterization of PEGylated Gd_2O_3 Nanoparticles for MRI Contrast enhancement. *Langmuir*, **2010**, *26*, 5753-5762.

19) Kumar, R.; Nyk, M., Ohulchanskyy, T. Y.; Flask, C. A.; Prasad, P. N. Combined Optical and MR bioimaging using Rare Earth Ion doped $NaYF_4$ Nanocrystals. *Adv. Funct. Mater*. **2009**, *19*, 853-859.

20) Lee, J. H.; Huh, Y. M.; Jun, Y. W.; Seo, J. W.; Jang, J. T.; Song,H. T.; Kim, S.; Cho, E. J.; Yoon, H. G.; Suh, J. S.; et al. Artificially Engineered Magnetic Nanoparticles for Ultra-Sensitive Molecular Imaging. *Nat. Med*. **2007**, *13*, 95–99.

21) Hu, F. Q.; Wei, L.; Zhou, Z.; Ran, Y. L.; Li, Z.; Gao, M. Y.Preparation of Biocompatible Magnetite Nanocrystals for *in Vivo* Magnetic Resonance Detection of Cancer. *Adv. Mater.* **2006**, *18*, 2553–2556.

22) Hahn. M. A.; Singh A. K.; Sharma P.; Brown S. C.; Moudgil B. M. Nanoparticles as contrast agents for in-vivo bioimaging: current status and future perspectives. *Ana. Bioanal. Chem*. **2011**, *399*, 3-27.

23) Atkins, P.; Overton, T.; Rourke, J.; Weller, M.; Armstrong, F. *Inorganic Chemistry,* fourth edition; Oxford Univerity Press: New York, 2006.

24) Rayner-Canham, G.; Overton, T. *Descriptive Inorganic Chemistry*, fifth edition; W. H. Freeman and Company: New York, 2010.

25) Sun, L.-D.; Gu, J.-Q.; Zhang, S.-Z.; Zhang, Y.-W.; Yan, C.-H. *Science in China Series B: Chemistry*. **2009**, *52*, 1590.

26) Auzel, F. Upconversion and Anti-Strokes Processes with f and d Ions in Solids. *Chem. Rev.* **2004**, 104, 139-173

27) Cotton, S. *Lanthanide and Actinide Chemistry,* John Wiley & Sons, Ltd: Chichester, 2006.

28) Wang, F.; Liu, X. Recent advances in the chemistry of lanthanide-doped upconversion nanocrystals. *Chem. Soc*. Rev. **2009**, *38*, 976-989.

29) Wang F. *et al*. Simutaneuous Phase and Size Control of Upconversion Nanocrystals through Lanthanide Doping. *Nature*. **2010**, *46*, 1061-1065.

30) Mason, S. F.; Stewart, B. *Lanthanide (III) f-f transition probabilities;* Academic Press: London, 1985.

31) Widmaier, E. P; Raff, H.; Strang, K. T. *Vander, Sherman, Luciano's Human Physiology: The Mechanisms of Body Function*; McGrawHill: New York, 2004.

32) Pavia D. L.; Lampman G. M.; Kriz G. S.; and Vyvyan J. R. *Introduction to spectroscopy, fourth edition*; Brooks/Cole Cengage learning: Belmont, 2009.

33) Smith, R. C.; Lange, R. C. Understanding Magnetic Resonance Imaging; CRC Press: Boca Raton, 1998.

34) Friebolin, H. *Basic One- and Two-Dimensional NMR Spectroscopy, fourth ed*.; Wiley-VCH: Weinheim, 2005.

35) Bloch, F. Nuclear Induction, *Phys. Rev*. **1946**, *70*, 460-473.

36) Tóth, É.; Helm, L.; Merbach A. E. *Relaxivity of MRI Contrast Agents*. W. Krause, ed. Springer: Berlin/Heindelber, 2002, pp 61-101.

37) Caravan, P.; Ellison, J. J.; McMurry T. J.; Lauffer R. B. Gadolinium(III) Chelates as MRI Contrast Agents: Structure, Dynamics, and Applications. *Chem. Rev*. **1999**, *99*, 2293-2352.

38) Naccache, R. Colloidal Upconverting Nanoparticles Systems for Integration in Targeting, Therapeutics, and Imaging Applications. Ph.D. Dissertation, Concordia University, Montreal, 2012.

39) Himo, F.; Lovell, T.; Hilgraf, R.; Rostpvtsev, V. V.; Noodleman, L.; Sharpless, and Fokin, V. V. Copper(I)-Catalyzed Synthesis of Azoles. DFT study Predicts Unprecedented Reactivity and Intermediates. *J. Am. Chem. Soc*. 2005, *127*, 210-216.

40) Hermanson, G. T. Bioconjugate Techniques; Academic Press: Boston, 2008.

41) Pokorski J.K; Miller Jenkins L. M.; Feng H. Q.; Durell S. R.; Bai Y.; Appella D. H.; Introduction of a Triazole Amino acid into a peptoid oligomer induces turn formation in aqueous solution. *Org. Lett*. **2007,** *9,* 2381- 2383.

42) Romain F. H. V.; Alison N. H., A Sensitized Europium Complex Generated by Micromolar Concentrations of Copper(I): Toward the Detection of Copper(I) in Biology. *J. Am. Chem. Soc.* 2006, *128*, 11370-1137.

43) Prasuhn D. E.; Yeh R. M.; Obenaus A.; Manchester M.; Finn M. G. *Chem Commun*. 2007, 1269-127.

44) Wong, H.-T; Vetrone, F.; Naccache, R.; Chan, H. L. W.; Hao, J. H. ; Capobianco, J. A. Water Dispersible Ultra-Small Multifunctional $KGdF_4$: Tm^{3+}, Yb^{3+} Nanoparticles with Near-Infrared to Near-Infrared Upconversion. *J. Mater. Chem*. **2011**, *21*, 16589-16596.

45) Heer, S.; Kompe, K.; Gudel, H.-U.; Hasse, Highly Efficient Multicolour Upconversion Emission in Transparent Colloids of Lanthanide-Doped $NaYF_4$ Nanocrystals. *Adv. Mater.* **2004**, *16*, 2101)

46) Winnischofer, H.; Rocha, T. C. R.; Nunes, W. C.; Socolovsky L. M.; Knobel, M.; Zanchet, D. Chemical Synthesis and Structural Characterization of highly Disordered Ni Colloidal Nanoparticles. *ACS Nano*. **2008**, *2*, 1305-1312.

47) Chen, Y.; Johnson, E.; Peng, X. Formation of Monodisperse and Shape-Controlled MnO Nanocrystals in Non-Injection Synthesis: Self-Focusing via Ripenining. *J. Am. Chem. Soc*. **2007**, *129*, 10937−10947.

48) Dinegar R. H.; LaMer V. K. Theory, Production and Mechanism of Formation of monodispersed Hydrosols. *J. Am. Chem. Soc*. **1950**, *72*, 4847-4854.

49) Murray, C. B.; Norris, D. J.; Bawendi M. D. Synthesis and Characterization of Nearly Monodisperse CdE (E = S, Se, Te) Semiconductor Nanocrystallites. *J. Am. Chem. Soc*. **1993**, *115*, 8706-8715.

50) Owen, J. S.; Chan, E. M.; Liu, H.; Alivisatos, A. P. Precursor Conversion Kinetics and the Nucleation of Cadmium Selenide Nanocrystals. *J. Am. Chem. Soc*. **2010**, *132*, 18206-18213.

51) Abe, S.; Capek, R. K.; De Geyter, B.; Hens, Z. Tuning the Postfocused Size of Colloidal Nanocrystals by the reaction Rate: From Theory to Application. *ACS Nano*. **2012**, *6*, 42-53.

52) Clark, M. D.; Kumar, S. K.; Owen, J. S.; Chan, E. M. Focusing Nanocrystal Size Distributions via Production Control. *Nano Lett*. **2011**, *11*, 1976−1980.

53) Arnold, A. A.; Terskikh, V.; Li, Q. Y.; Naccache, R.; Marcotte, I.; Capobianco, J. A. Structure of $NaYF_4$ Upconverting Nanparticle: A Multinuclear Solid-State NMR and DFT Computational Study. *J. Phys. Chem. C*. **2013**, *117*, 25733-25741.

54) Zhou, J.; Yu M-X.; Sun, Y.; Zhang, X-Z.; Zhu, X-J.; Wu Z.-H.; Wu D.-M.; Li, F.-Y. Fluorine-18-labeled $Gd^{3+}/Yb^{3+}/Er^{3+}$ co-doped NaYF4 nanophosphors for multimodality PET/MR/UCL imaging. *Biomaterials*. **2011**, *32*, 1148-1156.

55) Zhang, F.; Braun, G. B.; Zhang, Y. Shi, Y.; Sun, X.; Reich, N. O.; Zhao, D.; Stucky, G. Fabrication of $Ag@SiO_2@Y_2O_3$:Er Nanostructures for Bioimaging: Tuning of the Upconversion Fluorescence with Silver Nanoparticles. *J. Am. Chem. Soc.* 2010, *132*, 2850-2851.

56) Koole R.; Schooneveld, M. M.; Hilhorst, J.; Denegá C. de M.; 'tHart D. C.; Blaaderen, A. V.; Vanmaekelbergh D.; Meijerink A. On the Incorporation Mechanism of Hydrophobic Quantum Dots in Silica Spheres by a Reverse Microemulsion Method. *Chem. Mater*. **2008**, *20*, 2503-2512.

57) Bogdan, N.; Vetrone, F.; Ozin,G. A.; Capobianco, J. A. Synthesis of Ligand-Free Colloidally Stable Water Dispersible Brightly Luminescent Lanthanide-Doped Upconverting Nanoparticles**,** *Nano Lett.* **2011***, 11*,835-840.

58) Koole R.; Schooneveld, M. M.; Hilhorst, J.; Denegá C. de M.; 'tHart D. C.; Blaaderen, A. V.; Vanmaekelbergh D.; Meijerink A. On the Incorporation Mechanism of Hydrophobic Quantum Dots in Silica Spheres by a Reverse Microemulsion Method. *Chem. Mater*. **2008**, *20*, 2503-2512.

59) Himo, F.; Lovell, T.; Hilgraf, R.; Rostovtsev, V. V.; Noodkeman, L.; Sharpless, K. B.; Fokin, V. V. Copper(I)-Catalyzed Synthesis of Azoles. DFT Study Predicts Unprecedented Reactivity and Intermediates. *J. Am. Chem. Soc.* **2005**, *127*, 210-216.

60) Duncan, A. K.; Klemm, P. J.; Raymond, K. N.; Landry, C. C. Silica Microparticles as a Solid Support for Gadolinium Phosphate Magnetic Resonance Imaging Contrast Agents. *J. Am. Chem. Soc.* **2012**, *134*, 8046-8049.

61) Botta, M.; Tei, L. Relaxivity Enhancement in Macromolecular and Nanosized Gd^{III}-based MRI Contrast Agents. *Eur. J. Inorg. Chem*. **2012**, 1945-1960.

62) Clarkson, R. B. *Blood-Pool MRI Contrast Agents: Properties and Characterization*. W. Krause, ed. Springer: Berlin/Heindelber, 2002, pp 202-232.

63) Krofit, L. J.M; de Ross, A. Blood Pool Contrast Agents for Cardiovascular MR Imaging. *J Magn Resin Im*. **1999**, 10, 395-403.

64) Storm, G.; Belliot, S. O.; Daemen, T.; Lasic, D. D. Surface Modification of Nanoparticles to Oppose Uptake by the Mononuclear Phagocyte System. *Advanced Drug Delivery Reviews*. **1995**, *17*, 31-48.

65) Thorek D.L.J.; Tsourkas, A. Size, charge and concentration dependent uptake of iron oxide particles by non-phagocytic cells. *Biomaterials* **2008**, *29,* 3583–3590.

66) Perrault, S. D.; Walkey, C.; Jennings, T.; Fischer, H. C.; Chan, W. C. W. Mediating Tumor Targeting Efficiency of Nanoparticles Through Design. *Nano Lett*. **2009**, *9*, 1909-1915.

67) Choi H.S; Liu, W.; Misra, P.; Tanaka, E., Zimmer, J.P., Ipe, B. I.; Bawendi, M. G.; Frangioni, J. V. Renal clearance of quantum dots. *Nat. Biotechnol.* 2007, 25, 1165-70.

68) Lü, Q.; Li, A.H.; Guo, F.Y.; Sun, L.; Zhao, L.C. Experimental Study on the surface modification of Y_2O_3: $Tm^{3+/}Yb^{3+}$ nanoparticles to enhance upconversion fluorescence and weaken aggregation. *Nanotechnology,* **2008**,*19*, 145701.

69) Zhulina, E. B.; Borisov, O. V.; Priamitsyn, V. A. Theory of Steric Stabilization of Colloid Dispersions by Grafted Polymers. *J. Colloid and Interface Sci.* **1990**, *137*, 495-511.

70) Ortega-Vinuesa, J. L.; Martín-Rodríguez, A.; Hidalgo-A Lvarez R. Colloidal Stability of Polymer Colloids with Different Interfacial Properties: Mechanisms. *Colloid and Interface Sci.* **1996,** *184,* 259-267.

71) Krachler, M.; Mohl, C.; Emons, H.; Shotyk, W. Influence of digestion procedures on the determination of rare earth elements in peats and plants samples by USN-ICP-MS. *J. Anal. At. Spectrom*., **2002**, *17*, 844–851.

72) Casula, M. F.; Floris, P.; Innocenti, C.; Lascialfari, A.; Marinone, M.; Corti, M.; Sperling, R. A.; Parak, W. J.; Sangregorio, C. Magnetic Resonance Imaging Contrast

Agents Based on Iron Oxide Superparamagnetic Ferrofluids. *Chem. Mater*. **2010**, *22*, 1739-1748.

73) Vocke, R. D. Jr. Atomic Weights of the Elements 199. *Pure Appl. Chem*. **1999**, *71*, 1593-1607.

74) Feng, Y.; Zong, Y.; Ke, T.; Jeong, E-K.; Parker, D. L.; Lu, Z-R. Pharmacokinetics, Biodistribution and Contrast Enhanced MR Blood Pool Imaging of Gd-DTPA Cystine Copolymers and Gd-DYPA Cystine Diethyl Ester Copolymers in a Rat Model. *Pharm Res*, **2006**, *23*, 1736-1742.

Appendix A: Synthesis of Alkyne Gd-DOTA

8.1 Synthetic scheme for alkyne Gd-DOTA

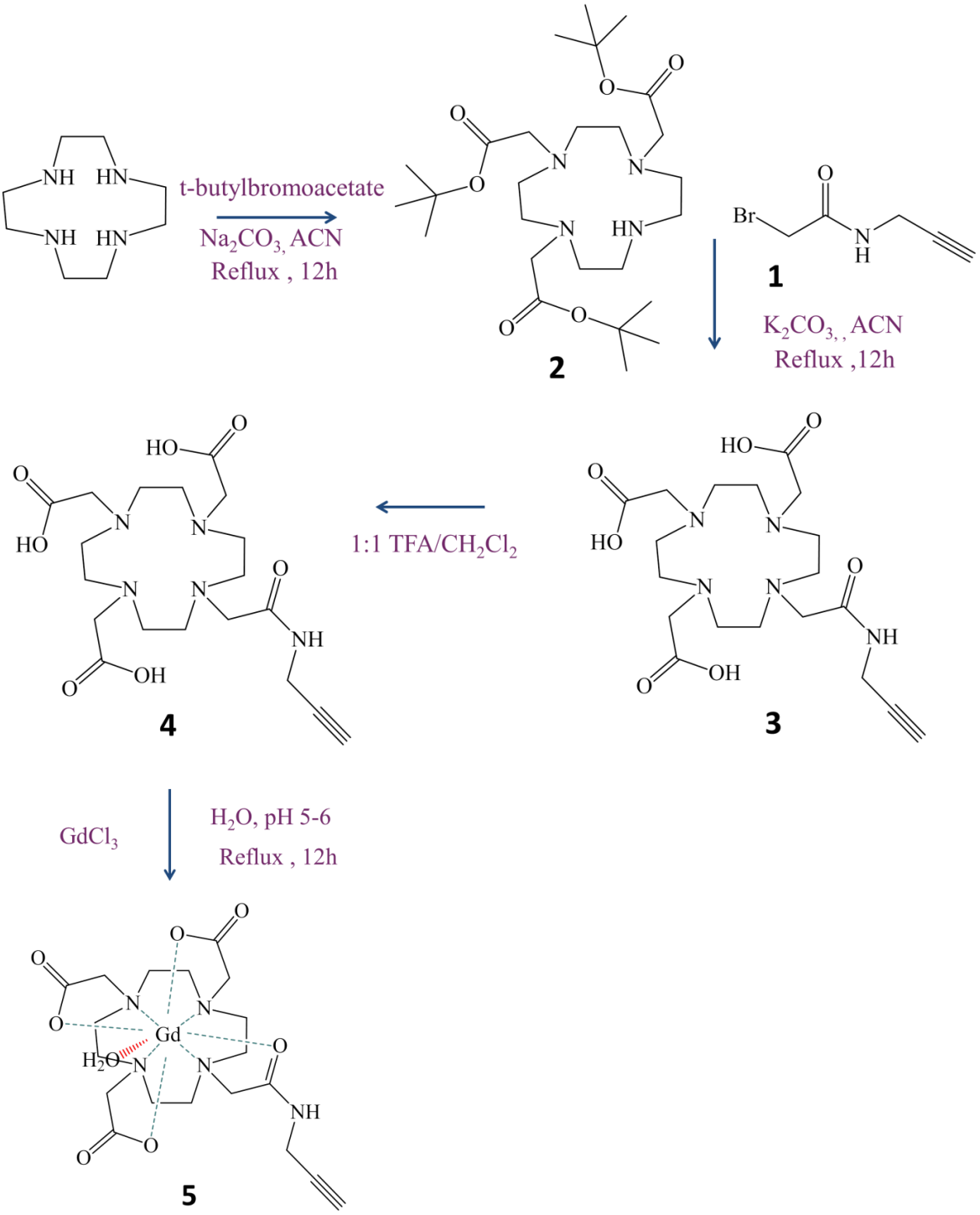

8.2 2-bromo-*N*-(propargyl)acetamide

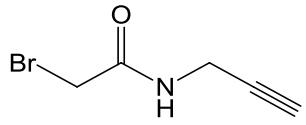

(1)

Yield: 68%

^{1}H NMR: $CDCl_3$, 500 MHz, 2.28 ppm (t, 1H, J=2.6 Hz, C≡C<u>H</u>), 3.90 (s, 1H, C<u>H$_2$</u>Br), 4.09 (dd, 2H, J= 2.6, 5.3 Hz, C<u>H$_2$</u>C≡CH), 6.75 (Br, 1H, CON<u>H</u>)

FTIR: KBr pellet, 3288 cm^{-1} (N-H stretching), 3251 (–C≡<u>C–H</u> stretching), 2956 (–C–<u>C–H</u> stretch), 2126 (C≡C stretching), 1673 (C=O stretching of amide), 1550 (N-H bending), 688 (C-H bending of terminal alkyne), 636 (C-Br str.)

Analytical data were in accordance with reported data in the literature [41].

8.3 Tri-*tert*-butyl 2, 2', 2'' - (1,4,7,10-tetraazacyclododecane-1,4,7-triyl) triacetate

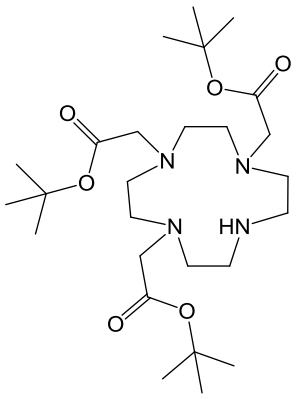

(2)

Yield: 71%

^{1}H NMR: $CDCl_3$, 500 MHz, 10.26 ppm (br, 1H, NH), 3.37(s, 4H, C<u>H$_2$</u>CO), 3.29 (s, 2H, CH_2CO), 3.09 (s, 4H, C<u>H$_2$</u>-C<u>H$_2$</u>-NH), 2.88-2.93 (m, 12H, CH_2-CH_2), 1.46 (s, 27, $C(CH_3)_3$)

FT-IR: KBr pellet, 3401cm^{-1} (N-H stretching), 2979 (C-H stretching), 1722 (C=O stretching of ester), 1592 (N-H bending), 1255 and 1157 (asymmetrical/symmetrical C-O stretching), 1157 (C-N stretching)

Analytical data were in accordance with reported data in the literature [42, 43].

8.4 Tri-*tert*-butyl 2, 2', 2'' - {10-[2-oxo-2-(2-propyn-1-ylamino)ethyl]-1,4,7,10-tetraazacyclododecane-1,4,7-triyl)} triacetate

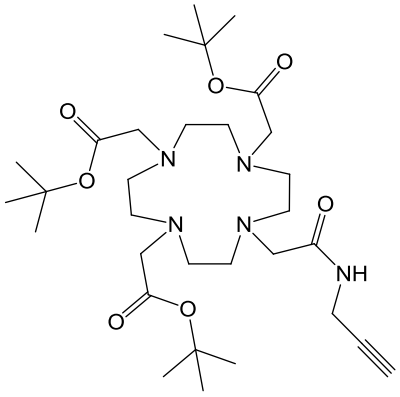

(3)

Yield: 66%

^{1}H NMR: $(CD_3)_2SO$, 500 MHz, 8.61 ppm (t, J=5.5 Hz, 1H, CONHCH$_2$), 3.88 (dd, J=2.4, 5.5 Hz, 2H, CH$_2$C≡CH), 3.31 (s, 8H, CH$_2$CO), 3.08 (t, J=2.4 Hz, 1H, C≡CH), 2.50 (s, 16H, 8xCH$_2$ cyclen), 1.44 (s, 9H, 3xCH$_3$), 1.43 (s, 18H, 6xCH$_3$)

^{13}C NMR: $CDCl_3$, 500 MHz, 172.3 ppm (CO), 171.0 (CO acetamide), 81.9 (C(CH$_3$)$_3$), 81.2 (C≡CH), 69.2 (C≡CH), 56.0 (NCH$_2$CO), 55.8 (NCH$_2$CONH), 52.1 (br, CH$_2$ cyclen)

FT-IR: KBr pellet, 3313cm^{-1} (C-H stretching of C≡CH), 2113 (C≡C stretching), 2979 (C-H stretching), 1726 (C=O stretching of ester), 1666 (C=O stretching of amide), 1552 (N-H bending), 1160 (asymmetrical/symmetrical C-O asymmetrical/symmetrical), 1101 (C-N asymmetrical/symmetrical)

Analytical data were in accordance with reported data in the literature [42, 43].

8.5 2, 2', 2'' - {10-[2-oxo-2-(2-propyn-1-ylamino)ethyl]-1,4,7,10-tetraazacyclododecane-1,4,7-triyl)} triacetic acid

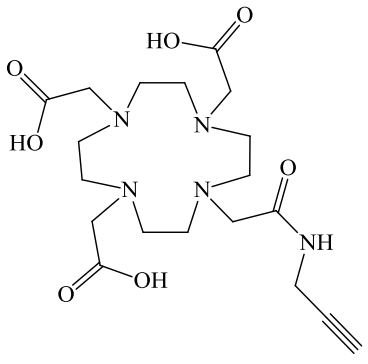

(4)

Yield: 54%

^{1}H NMR: (500 MHz, D_2O) 3.82 ppm (d, J = 2.2 Hz, 2H, C*H*$_2$C≡CH), 3.80 (s, 2H, C*H*$_2$CO), 3.72 (s, 4H, C*H*$_2$, C*H*$_2$CO), 3.53 and 3.54 (2s, 4H, 2xC*H*$_2$ cyclen), 3.38 (broad, 6H, C*H*$_2$ cyclen), 3.02 (broad, 6H, CH_2 cyclen), 2.55 (1H, J = 2.5 Hz, 1H, C≡C*H*)

FT-IR: KBr pellet, broad 3149 – 2709 cm^{-1} (O-H str. of carboxylic acid), 2967 (C-H str.), 1727 (C=O of carboxylic acid), 1688 (C=O of amide), 1210 (C-O str.).

Analytical data were in accordance with reported data in the literature [42, 43].

8.6 Gadolinium 2, 2', 2'' - {10-[2-oxo-2-(2-propyn-1-ylamino)ethyl]-1,4,7,10-tetraazacyclododecane-1,4,7-triyl)}triacetate

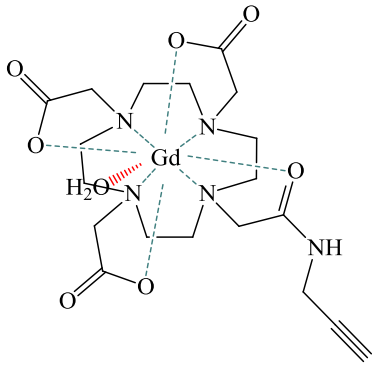

(5)

Yield: 35%

Purity: >99%

FT-IR: KBr pellet, 3307 cm^{-1} (N-H stretching of amide), 2993 (C-H stretching), 2128 (C≡C stretching), 1697 and 1404 (asymmetric and symmetric partial C=O stretching of carboxylate), 1625 (C=O stretching of amide), 1209 (C-O stretching), 1132 (C-N stretching).

Analytical data were in accordance with reported data in the literature [42, 43].

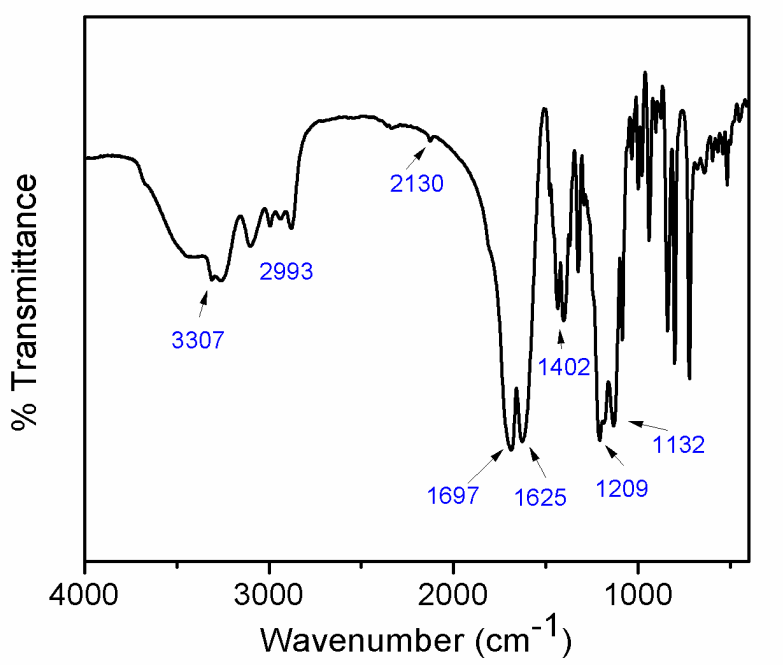

Figure 8.1: FTIR spectrum of alkyne Gd-DOTA.

The mass spectrometry analysis showing in figure 8.1 strongly confirmed the identity of compound (5). The most intense peak at 597.13 m/z observed in the mass spectrum (a) corresponded to the atomic mass of compound (5) and the peak at 299.07 corresponded to the doubly charged ion of the same compound. In the magnified spectrum (b), scanned from 588 to 608 m/z, the patterns of the peaks were found to correspond to the percentage of relative abundance of gadolinium isotopes. Therefore, this information further confirmed the presence of the gadolinium element in the compound alkyne Gd-DOTA [73].

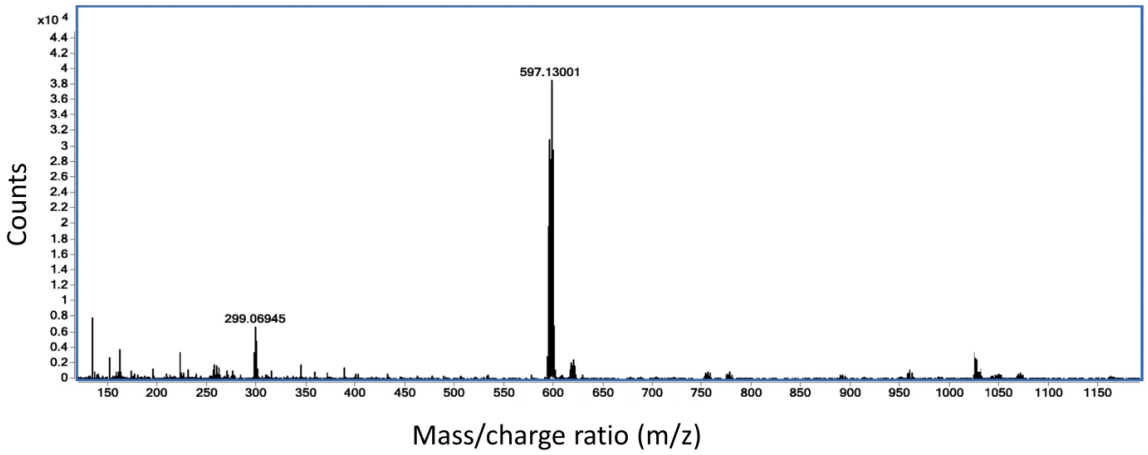

(a)

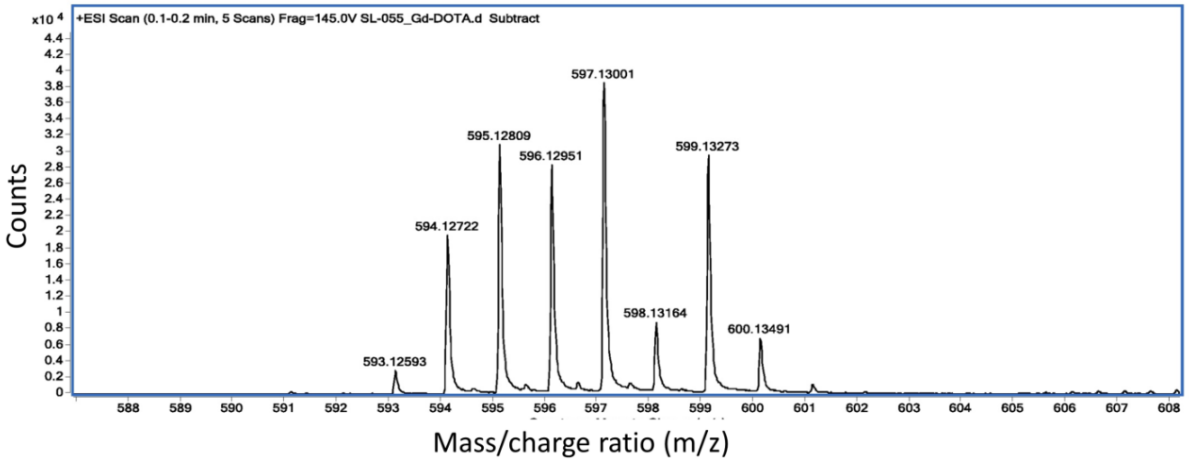

(b)

Figure 8.2: Mass spectra of compound (5), alkyne_Gd-DOTA. (a) scanned from 150 -1150 m/z (b) a magnified spectrum scanned from 588 to 608 m/z.

Appendix B: Characterization of Lysine Coated US-$NaGdF_4$: Tm^{3+}, Yb^{3+}

FT-IR: KBr pellet, 3346 cm^{-1} (N-H stretching of amine), 2930 (C-H stretching), 1563 and 1427 (asymmetric and symmetric partial C=O stretching of carboxylate), 1026 (C-O stretching).

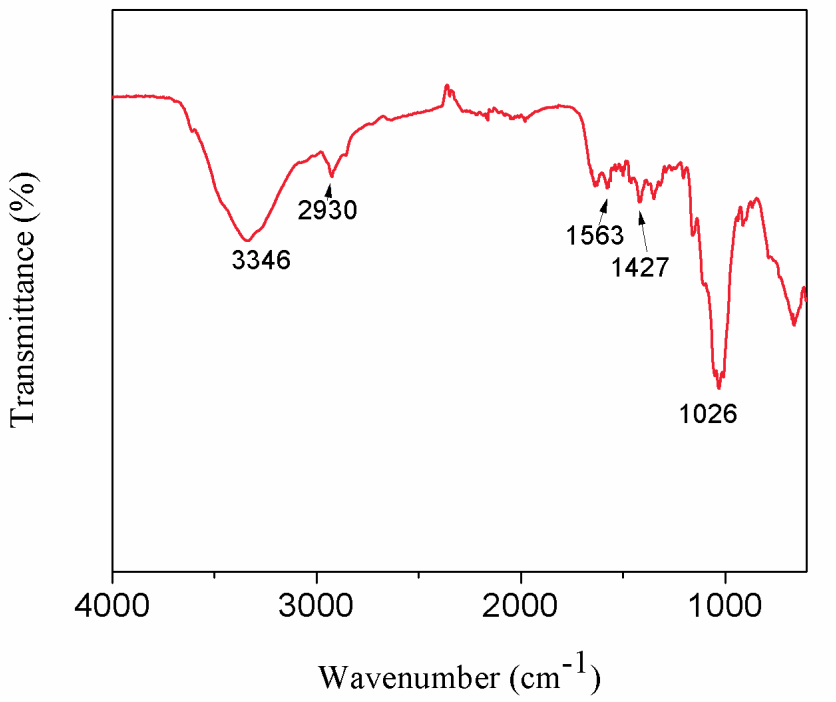

Figure 9.1: FTIR spectrum of Lysine Coated US- $NaGdF_4$: Tm^{3+}, Yb^{3+}.